الجـــــــــــــــــــمـهـوريـــــة الجـــــــــــــزائـريـة الديمـــــــقـراطيـة الـشـــــــــعبيـة

People's Democratic Republic of Algeria

وزارة التـــــــــــــــــــــــــــــعـليـم العـــــــالي و البـــــــــحث العـــــلـمـــي

Ministry of Higher Education and Scientific Research

جـــــــــــــامعة أبي بكـــر بـلـقـايد – تـلمســـــــــــــان –

University of Aboubakr Belkaïd – Tlemcen –
Faculty of Technology
Laboratory of Computational Mechanics

THESIS

Presented for obtaining the degree of **DOCTORATE 3rd Cycle**

In Mechanical Engineering

Specialty Mechanical construction

Presented by Merwan Behar

Subject

Vibration behavior of a smart rotating nanoshaft

Comportement vibratoire d'un nano-arbre tournant intelligent

Publicly defended, 20/01/2025, in front of a thesis committee :

M.Benachour Mustapha	Professor	Univ. Tlemcen	Chairman
M.Boukhalfa Abdelkrim	Professor	Univ. Tlemcen	Supervisor
M.Amirat Mohamed	Professor	Univ. Tlemcen	Examiner 1
M.Saimi Ahmed	Assoc. Prof. 'A'	Univ. Ain Temouchent	Examiner 2

بسم الله الرحمن الرحيم

Declaration

I hereby affirm that this thesis represents my original work and has not been submitted for any other degree or examination at any university. All sources of information and assistance utilized in the preparation of this thesis have been properly acknowledged. I fully understand that any form of plagiarism or academic misconduct may result in serious consequences.

Merwan Behar

2024

Dedicate

I dedicate this thesis to the memory of my late father, may God have mercy on his soul, and to my mother and sister, whose boundless love and sacrifices laid the foundation for my ambitions. Their unwavering support and encouragement have been my greatest source of strength. I also extend my heartfelt gratitude to my dear friends, whose companionship brought much-needed balance to my academic journey.

To every mentor, colleague, and participant who contributed to this work, I offer my sincere thanks. Your insights and guidance were truly invaluable. This achievement is not mine alone; it is a shared success made possible by the steadfast support of my family, friends, and the remarkable individuals who believed in me. Thank you for being the guiding light in this academic endeavor.

Acknowledgements

I begin by offering my deepest thanks to Allah, whose divine guidance illuminated my journey and bestowed upon me the strength to persevere through every challenge.

I am immensely grateful to my mentor, A BOUKHALFA, for his invaluable wisdom and guidance, which played a pivotal role in shaping the direction of this research.

I owe a special debt of gratitude to my Chairman M. BENACHOUR and examiners, M. AMIRAT and A. SAIMI, for their gracious willingness to undertake the evaluation of my work. A heartfelt thank you goes to A.L. AOUINAT, whose unwavering support and motivation were instrumental to my success.

I also extend my appreciation to the entire MECACOMP laboratory team, my colleagues, and the broader scientific community for fostering an environment of collaboration and intellectual development.

To my dearest family and friends, whose constant encouragement has been my greatest source of strength—this achievement is as much yours as mine. Your steadfast support has been the foundation of my academic journey, and for that, I am eternally grateful.

Abstract

This thesis introduces a novel mathematical formulation to investigate the vibration behavior of rotating smart nanoshafts. The model integrates Euler-Bernoulli beam theory with the nonlocal strain gradient theory and Maxwell's electrostatic equations. The smart nanoshaft structure is composed of a single-walled boron nitride nanotube (SWBNNT), chosen for its exceptional piezoelectric and magnetic properties, which make it highly suitable for rotating components in nanoelectromechanical systems (NEMS).

The electro-mechanical equations of motion are derived using Hamilton's principle and solved semi-analytically through Galerkin-based closed-form solutions. Forthermore, the effects of rotating speed, mode number, external voltage, temperature change, geometrical parameters, material length scale, and nonlocal parameters on natural frequencies and critical speed are investigated.

This work represents the first comprehensive analysis of these factors under various boundary conditions for rotating smart nanoshafts, offering valuable insights into their vibrational dynamics. The results are contextualized within the existing literature, demonstrating the accuracy and efficiency of the proposed model. This establishes the formulation as a robust numerical tool for analyzing the behavior of rotating nanoscale structures.

Keywords: Galerkin closed-form solution, Smart nanotube, piezoelectric material, rotating nanotube, Critical speed, Euler-Bernoulli beam theory.

ملخص

تقدم هذه الأطروحة صياغة رياضية جديدة لدراسة سلوك الاهتزاز للأعمدة النانوية الذكية الدوارة. يدمج النموذج نظرية حزمة أويلر-برنولي مع نظرية التدرج الإجهادي غير المحلية ومعادلات ماكسويل الكهروستاتيكية. يتكون هيكل العمود النانوي الذكي من أنبوب نانوي من نيتريد البورون أحادي الجدار(SWBNNT) ، تم اختياره لخصائصه الكهروضغطية والمغناطيسية الاستثنائية، مما يجعله مناسبًا للغاية للمكونات الدوارة في أنظمة النانو الكهروميكانيكية.(NEMS)

يتم اشتقاق المعادلات الكهروميكانيكية للحركة باستخدام مبدأ هاملتون وحلها شبه تحليليًا من خلال حلول مغلقة الشكل تعتمد على طريقة غاليركين. تدرس هذه الدراسة بشكل منهجي آثار سرعة الدوران، ورقم النمط، والجهد الخارجي، وتغير درجة الحرارة، والمعلمات الهندسية، ومقياس طول المادة، والمعلمات غير المحلية على الترددات الطبيعية والسرعة الحرجة.

يمثل هذا العمل أول تحليل شامل لهذه العوامل تحت ظروف حدودية مختلفة للأعمدة النانوية الذكية الدوارة، مما يوفر رؤى قيمة حول ديناميكيات اهتزازها. يتم وضع النتائج في سياق الأدبيات الموجودة، مما يدل على دقة وكفاءة النموذج المقترح. يؤسس هذا الصياغة كأداة عددية قوية لتحليل سلوك الهياكل النانوية الدوارة.

الكلمات المفتاحية: حل غاليركين في الصورة المغلقة، أنبوب نانوي ذكي، مادة كهرضغطية، أنبوب نانوي دوار، السرعة الحرجة، نظرية الجائز أويلر وبرنولي

Résumé

Cette thèse présente une nouvelle formulation mathématique pour étudier le comportement vibratoire des nano-arbres intelligents en rotation. Le modèle intègre la théorie des poutres d'Euler-Bernoulli avec la théorie du gradient de déformation non local et les équations électrostatiques de Maxwell. La structure du nano-arbre intelligent est composée d'un nanotube de nitrure de bore à paroi simple (SWBNNT), choisi pour ses propriétés piézoélectriques et magnétiques exceptionnelles, qui le rendent particulièrement adapté aux composants rotatifs dans les systèmes nanoélectromécaniques (NEMS).

Les équations électromécaniques du mouvement sont dérivées en utilisant le principe de Hamilton et résolues de manière semi-analytique par des solutions à forme fermée basées sur la méthode de Galerkin. Cette étude examine méthodiquement les effets de la vitesse de rotation, du nombre de mode, de la tension externe, du changement de température, des paramètres géométriques, de l'échelle de longueur du matériau et des paramètres non locaux sur les fréquences naturelles et la vitesse critique.

Ce travail représente la première analyse complète de ces facteurs sous diverses conditions aux limites pour les nano-arbres intelligents en rotation, offrant des aperçus précieux sur leur dynamique vibratoire. Les résultats sont contextualisés dans la littérature existante, démontrant la précision et l'efficacité du modèle proposé. Cela établit la formulation comme un outil numérique robuste pour analyser le comportement des structures nanométriques en rotation.

Mot-clé : Solution fermée de Galerkin, Nanotube intelligent, Matériau piézoélectrique, Nanotube rotatif, Vitesse critique, Théorie des poutres d'Euler-Bernoulli.

List of Figures

List of Tables

Nomenclature

Abbreviations

BaTiO3	barium titanate
CaTiO3	calcium titanate
C-C	Clamped- clamped
C-S	Clamped-simply supported
C-F	Clamped-Free
DFT	density functional theory
DQM	Differential quadrature Method
DWCNT	Double-walled carbon nanotube
FEM	Finit element Method
FGM	Functionally graded material
HAP	Hydroxyapatite
Ird	Inward radial deviation
MCST	Modified couple stress theory
MD	Molecular dynamics
MWNT	Multi-walled nanotube
NSFEM	Nanoscale finite element modeling
NSGT	Nonlocal strain gradient theory
PbTiO3	lead titanate
PZT	lead zirconate titanate
RRT	Rotation transmission ratio
RTS	Rotation Transmission Nanosystem
SCNT-MF	Spinning carbon nanotube membrane filter
S-S	Simply supported
SWBNNT	Single-walled Boron nitride nanotube
SWCNT	Single-walled carbon nanotube
SWGaNNT	Single-walled Galium nitride nanotube
SWNT	Single-walled nanotube
SWSiCNT	Single-walled Silicon Carbide Nanotube
SWZnONT	Single-walled Zinc oxide nanotube
TWNT	Triple-walled nanotubes

Roman Symbols

A	cross-section area.	$[nm^2]$
$A_i(1,4)$	The constants with values of 0 or 1, selected based on the boundary conditions.	
C_{ijkl}	Fourth-Order Elasticity Tensor.	
D_x^w	Electrical displacement in x direction.	
D_y	Electrical displacement in y direction.	
D_z	Electrical displacement in z direction.	
E	Young modulus.	[GPa]
E_x^w	Electrical field in x direction	
E_y	Electrical field in y direction	
e_{31}	Transverse piezoelectric constant.	$[C/m^2]$
e_{21}	Lateral piezoelectric constant.	$[C/m^2]$
$e_0 a$	the scale coefficient	
E_z	Electrical field in z direction	
f_w	Forward whirl	[Hz]
G	The gyroscopic matrices	
h	Thickness of the nanotube.	$[nm]$
I	diametral moment of inertia.	$[nm^4]$
K	The stiffness matrices	
L	Length of the nanotube.	$[nm]$
$\mathcal{L}(x,y,t)$	Transvers electrical potential	
M	The mass matrices	
M_y	Moment around z	
M_z	Moment around y	
n	The longitudinal mode numbers.	
r	Radius of the nanotube.	$[nm]$
T	The kinetic energy	
$T(x,z,t)$	Transvers electrical potential	
U_x	the axial displacements.	
U_y	The lateral displacements.	
U_z	The transverse displacements.	
V	the potential energy	
V_0	External electric voltage.	[Volt]
W	The work done by an external forses	
x	Longitudunal axes	
y	Lateral axes	
$Y(x)$	The beam function	
z	Transvers axes	
b_w	Backward whirl	[Hz]
d	diameter of the nanotube.	$[nm]$
l	The strain gradient parameter.	$[nm]$

l_0	The SWNTs bond length.	$[nm]$
λ_i	The real value proportional to the number of axial modes.	
$\frac{\partial v}{\partial x}$	the rotation of nanoshaft cross-section about y axes	
$\frac{\partial w}{\partial x}$	the rotation of nanoshaft cross-section about z axes	

Greek Symbols

$(\vec{a}_1 + \vec{a}_2)$	The basis vectors.	
α	The thermal expansion coefficient	
ΔT	The temperature change	$[K^0]$
ε_{xx}^{v}	The lateral normal strains.	
ε_{xx}^{w}	The transverse normal strains.	
η	The non-local parameter.	$[nm]$
ζ	The dimensionless frequency	
ξ_{11}	Longitudinal dielectric constant.	$[F/m]$
ξ_{22}	Lateral dielectric constant.	$[F/m]$
ξ_{33}	Transvers dielectric constant.	$[F/m]$
Ω	spinning speed.	[Hz]
Ω_{Cr}	Critical speed.	[Hz]
ρ	The mass density.	$[Kg/m^3]$
τ	The dimensionless nonlocal parameter	
θ_0	The armchair chiral angles.	$[rad]$
ω	The natural frequency.	[Hz]
∇^2	the Laplace operator	
υ	Poisson's ratio	

introduction

Richard Feynman's 1959 lecture "There's Plenty of Room at the Bottom," delivered at the annual meeting of the American Physical Society, introduced the groundbreaking concept of manipulating individual atoms as a more powerful form of synthetic chemistry. Although initially overlooked, this visionary idea gained traction in the 1980s.

In his lecture, Feynman proposed the creation of nanomachines capable of arranging atoms precisely, thereby revolutionizing chemical synthesis through mechanical manipulation. He also presented the intriguing concept of "swallowing the doctor," credited to his friend and graduate student Albert Hibbs, who envisioned a miniature, ingestible surgical robot.

Feynman's ideas inspired many researchers in the early 1980s to explore the possibilities of engineering at the atomic scale. This burgeoning field of nanotechnology evolved through key scientific advancements and conceptual frameworks. By the early 2000s, it had captured public attention and sparked controversy, leading to increased government funding and the emergence of commercial applications. However, these initial practical uses were primarily limited to bulk nanomaterials rather than the more ambitious visions of molecular nanotechnology that Feynman had originally proposed.

Just as mechanical engineering pioneered technological advancements before its electrical counterpart, it was also at the forefront of entering the realm of nanotechnology. Nanomechanics has emerged as an interdisciplinary field, bridging classical mechanics, solid-state physics, statistical mechanics, materials science, and quantum chemistry.

The development of piezoelectric materials, also known as smart materials, has sparked scientific interest in their potential applications within nanomechanics. These materials exhibit a unique linear electromechanical interaction between mechanical and electrical states in crystalline structures lacking inversion symmetry.

Atomistic simulation is the most comprehensive theoretical approach to understanding the mechanical behavior of nanoscale materials. However, these simulations can be costly and time-consuming. In response, mechanical engineers developed new theories derived from classical continuum mechanics. In 1972, Eringen proposed a simple stress gradient nonlocal model, positing that "stress at a point in the continuum is a function of the stress field at every point in the continuum." Later, in 1993, Aifantis introduced a higher-order strain gradient elasticity theory for finite and infinitesimal deformations, building on his earlier plasticity studies.

With the advent of carbon nanotubes and initial molecular dynamics (MD) simulation results, comparisons were made between MD simulations and predictions from Eringen and Aifantis theories. However, these theories proved less accurate than MD simulations. To address this discrepancy, Askes and Aifantis (2011) proposed a unified model combining Eringen's strain-driven and Aifantis's stress-driven nonlocal gradient models, termed the "Nonlocal Strain Gradient Model." This new combined theory yields results that closely align with MD simulations and has become one of the most important and widely used approaches for predicting nanostructure behavior.

Piezoelectric nanomaterials possess the unique ability to convert mechanical energy from vibrations, movement, or pressure into electrical energy, and vice versa. This property has potential applications across various nanotechnological fields, including energy harvesting, precision actuation, nanoelectromechanical systems (NEMS), and biomedical devices. To accurately predict the nanoelectromechanical behavior of these materials, it's necessary to combine piezoelectric theory with non-classical mechanics.

The nonlocal strain gradient piezoelectric theory emerged at the beginning of the 2010s and has since been widely adopted by researchers, particularly for studying the vibration behavior of piezoelectric nanostructures such as nanobeams, nanoshells, and nanoplates.

While extensive research has been conducted on the vibration response of rotating nanoshaft systems composed of carbon nanotubes, studies on the free vibration of rotating smart nanoshafts based on piezoelectric nanotubes, such as boron nitride nanotubes, are comparatively scarce. Moreover, there is a notable lack of research applying the nonlocal strain gradient piezoelectric theory to analyze the spin effect in these nanomaterials. This thesis aims to address these knowledge gaps by investigating the vibration of rotating smart nanoshafts using the nonlocal strain gradient piezoelectric theory, thereby making a significant contribution to the rapidly evolving field of nanostructure resear

Thesis Structure

To comprehensively understand the vibration behavior of rotating smart nanoshafts, this thesis is organized into six meticulously structured chapters:

- Chapter 1: This chapter offers a comprehensive overview of rotating nanodevices. It begins by detailing the structural and physical properties of smart nanotubes, including their piezoelectric, mechanical, dielectric, and thermal characteristics. Additionally, it reviews existing rotating nanosystems discussed in the literature, emphasizing vibrational analyses performed using atomistic simulation techniques. The chapter also identifies key gaps in the current research related to the vibration behavior of rotating smart nanoshafts. Finally, it presents the objectives of this thesis, which aim to address these gaps, introduce novel methodologies, and advance the understanding of vibration phenomena in rotating functionally graded nanoshafts.
- Chapter 2: This chapter provides an in-depth analysis of various models for studying rotating smart nanoshafts. It begins by introducing the linear piezoelectric theory, which describes the electromechanical interactions within smart materials. Additionally, we explore several nonclassical continuum mechanics theories commonly used to model nanostructures. Finally, we present our foundational equation for modeling the spinning smart nanoshaft, incorporating piezoelectric theory, Euler-Bernoulli beam theory, and the nonlocal strain gradient theory. In this chapter, we also propose a modified electrical potential function to account for dual polarization effects within the structure.
- Chapter 3: In this chapter, we derive the final equation of motion and boundary conditions for a rotating smart nanoshaft using Hamilton's principle. The resulting equation accounts of piezoelectric, small-scale, thermal, gyroscopic, and centrifugal effects. Furthermore, we introduce a semi-analytical approach based on the Galerkin method to solve the equation and obtain the vibrational response of the rotating smart nanoshaft. Additionally, this chapter discusses the comprehensive code implementation developed to analyze vibrational behavior.
- Chapter 4: This chapter explores the free vibration characteristics of a rotating smart nanoshaft using the nonlocal strain gradient piezoelectric theory. The key findings demonstrate how factors such as the material length scale, nonlocal parameters, rotational speed, applied external voltage, temperature variations, initial hoop tension, and slenderness ratio influence both forward and backward whirls. Special attention is given to the unique vibrational behavior under cantilever boundary conditions.
- Chapter 5: This chapter investigates the stability dynamics of a smart nanoshaft subjected to thermo-electrical loading, employing the nonlocal strain gradient piezoelectric theory. The key findings reveal that factors such as material length scale, nonlocal parameters, and applied external voltage can influence the critical speed of the nanoshaft, thereby enhancing its stability. Additionally, it is observed that smart nanoshafts composed of SWBNNTs exhibit excellent temperature resistance, and the initial hoop tension does not impact the critical speed of the system. Furthermore, this

chapter highlights that shorter nanoshafts demonstrate greater stability compared to longer ones.

- Chapter 6: This chapter presents the key conclusions of the study and outlines promising avenues for future research.

Chapter 1: Literature review

Objective :

This chapter contains three main parts. First, it delves into the properties of smart nanotubes, covering aspects like structure, mechanics, piezoelectricity, magnetism, dielectrics, and heat conductivity. Second, it traces the history of rotating nanosystems, from the early use of double and multi-walled carbon nanotubes to the incorporation of smart single-walled nanotubes. Finally, the chapter reviews existing literature, identifying gaps and limitations that our research aims to address. By identifying areas for further investigation, we hope to contribute to ongoing discussions and advance the field's exploration of new ideas and innovations.

1.1. Structural and physical properties of smart nanotube

1.2. Dynamical response of Rotating nanosystem based on atomistic simulation

1.3. Dynamical response of rotating smart nanotube based on non-classical continuum mechanics

1.4. gaps identification based on existing literature

1.5 Aim and Objectives

1.6 Summary

1.1 Structural and physical properties of smart nanotube

Recently, an exciting new category of materials called "smart materials" has emerged,[10] showcasing remarkable versatility and potential. This group includes perovskites,[11] such as lead zirconate titanate (PZT), barium titanate ($BaTiO_3$), calcium titanate ($CaTiO_3$), and lead titanate ($PbTiO_3$). It also encompasses wurtzite bulk materials,[12] like boron nitride (BN), zinc oxide (ZnO), and gallium nitride (GaN). These materials can convert various types of energy, like electricity and magnetism, into mechanical energy and back again.[12] This versatility makes them useful in many engineering applications. For example, these materials are employed in sensor technology,[13] spanning pressure sensors, accelerometers, and force sensors. When these materials undergo mechanical stress, they produce an electric charge directly proportional to the applied force, rendering them exceptionally adept for sensing tasks. Moreover, they find extensive use in actuator systems,[14] which convert electrical energy into mechanical motion. They are integral components in devices like piezoelectric motors, renowned for their precision in positioning systems, nanopositioning stages, and autofocus mechanisms in cameras. In the realm of medical and industrial technology, piezoelectric crystals, a subset of smart materials, serve as fundamental components in ultrasound transducers.[15] When subjected to an electrical signal, they emit ultrasonic waves crucial for applications such as medical imaging, industrial testing, and cleaning processes. Smart materials also excel in energy harvesting,[16] converting mechanical vibrations or movements from the environment into usable energy. This energy can power low-power electronic devices or recharge batteries, making smart materials crucial for wearable technology and wireless sensor networks. Moreover, smart materials are vital in igniting gas appliances[17] such as barbecues and gas stoves. They are utilized in igniters to safely and reliably produce sparks for igniting gas. In the realm of acoustics, these materials find diverse applications in devices such as speakers, buzzers, and piezoelectric pickups for musical instruments. When subjected to an alternating electric field, these materials vibrate, producing sound waves with remarkable clarity. Lastly, in microphone technology, piezoelectric materials can efficiently convert sound waves into electrical signals. When exposed to sound pressure, they generate an electric charge proportional to the intensity of the sound, facilitating precise audio capture.

In the nanotechnology field, these materials offer unique nano-scale structures and particles, including nanotubes,[18] hexagonal nanosheets,[19], [20] nanowires,[21] and nanorods.[22] **Figure** 1.1 provides a detailed illustration of various configurations of wurtzite bulk smart nanostructures. The arrangement of atoms differs according to the type of material.

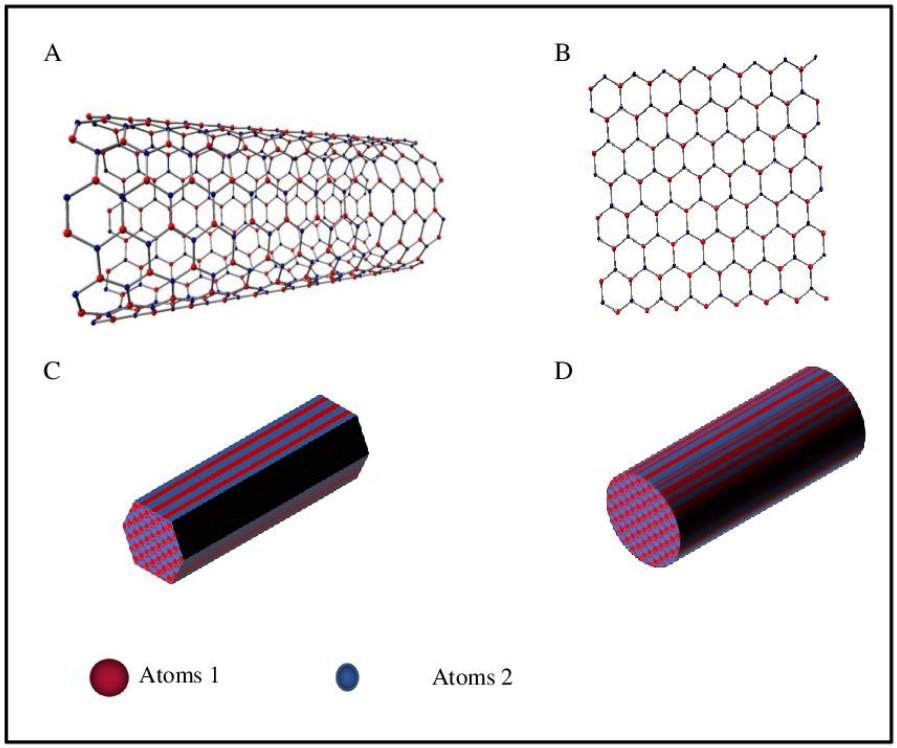

Figure1.1: Detailed illustration of various configuration of wurtzite bulk smart nanostructures

Table 1.1 provides a breakdown of the atom types corresponding to each material type. In perovskite materials, the crystal structure is characterized by the ABC formula., as shown in **Figure** 1.2

Tbale 1.1: Breakdown of the atom types corresponding to each material type

Materials	Atoms 1	Atoms 1
Borone nitride	Borone	nitride
Gallium nitride	Gallium	nitride
Zinc Oxide	Zinc	Oxygen

In this formula, 'A' and 'B' represent two positively charged ions (cations), often with distinct sizes, whereas 'X' signifies a negatively charged ion (an anion), commonly oxide, bonding to both cations.[23] Typically, the 'A' atoms are greater in size than the 'B' atoms. In the ideal cubic structure, the 'B' cation is enveloped by an octahedron of anions in a 6-fold coordination, and the 'A' cation displays a 12-fold cuboctahedral coordination.

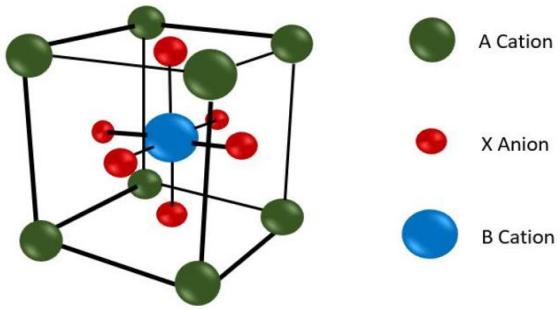

Figure 1.2: Perovskite crystal structure ABX

Perovskite crystal arrangements can adopt various nanostructure geometries, such as nanotubes, nanowires, and nanorods. **Figure** 1.3 and **Table** 1.2 provides a detailed illustration of these different perovskite nanostructures. The detailed structural and electronic properties of different smart nanostructures are illustrated in the next sub-section.

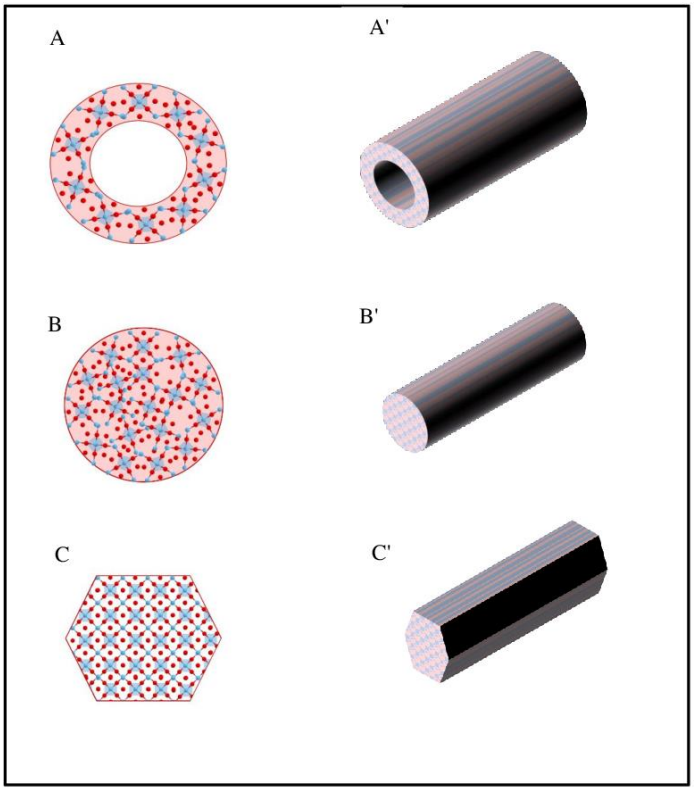

Figure 1.3: Different perovskite nanostructure.

Table 1.2: Type atom of each perovskite crystal structure

	PZT	BaTiO3	CaTiO3	PbTiO3
A Cation	Plomb Atom (Pb)	Barium Atom (Ba)	Calcium Atom (Ca)	Plomb Atom (Pb)
X Anion	Oxygen Atom (O_3)	Titanate Atom Ti	Oxygen Atom (O_3)	Oxygen Atom (O_3)
B Cation	Titanate Atom (Ti), or zirconate Atom (Zr)	Oxygen Atom (O_3)	Titanate Atom (Ti)	Titanate Atom (Ti)

1.1.1 structural properties of smart nanostructure*:*

Single- and multi-walled smart nanotubes are formed by rolling up single- or multi-layer hexagonal nanosheets, As shown in **Figure** 1.4. The rolling direction of these nanosheets is defined by the chirality vector (n, m), where the indices n and m represent the number of unit vectors along three distinct directions in the hexagonal lattice. The nanotubes are called "zigzag" when $m = 0$, "armchair" when $m = n$, and chiral when $m \neq n$, (see **Figures** 4.(b), (c), (d)).[24] Smart nanotubes can crystallize in both single- and multi-walled nanophases. Multi-walled NTs (MW-NTs) consist of multiple concentric single-walled NTs (SW-NTs), (see Figure 1.5). In addition, The atoms A and B are related by the band length, which has a cylindrical form.

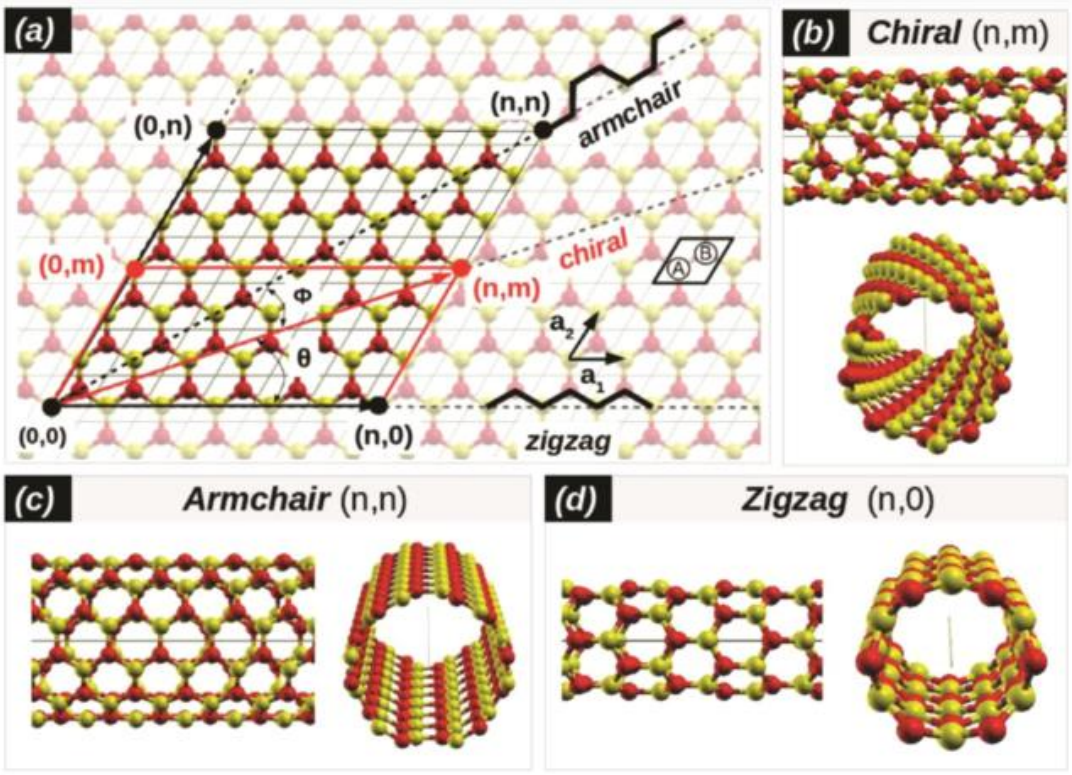

Figure 1.4: Scheme for constructing a generic SWNTs: (a) starting from a monolayer surface to form structures with (b) chiral (n,m), (c) armchair (n,n), and (d) zigzag (n,0) symmetries.[24]

The number of atoms in a single nanotube can be determined using Equation (1.1). Its structure is defined by the chiral vector $R^{\rightarrow} = n\vec{a}_1 + m\vec{a}_2$ in the unrolled sheet, where $\vec{a}_1$ and $\vec{a}_2$ are the base vectors. Additionally, the chiral angle (θ) is defined as the angle between $\vec{R}$ and $\vec{a}_1$ (**Figure** 1.4 (a)). Using $\vec{R}$, the nanotube diameter (d) and θ can be calculated with Equations (1.2) and (1.3).[24]

$$4(n^2 + nm + m^2).gcd^{-1}(2n + m, 2n + m) \tag{1.1}$$

$$d = \sqrt{3}.l\frac{\sqrt{n^2 + nm + m^2}}{\pi} \tag{1.2}$$

$$\theta = tan^{-1}\left(\sqrt{3}\frac{m}{2n + m}\right) \tag{1.3}$$

Here, d represents the A–B bond length. The armchair and zigzag chiral angles are fixed at 30° and 0°, respectively. For chiral nanotubes, however, the angle θ varies depending on the n and m values. The optimal value of the bond lengths for SWZnONT, SWBNNT, and SWGaNNT are approximately $0.1877, 0.147, 0.195\ nm$, respectively.

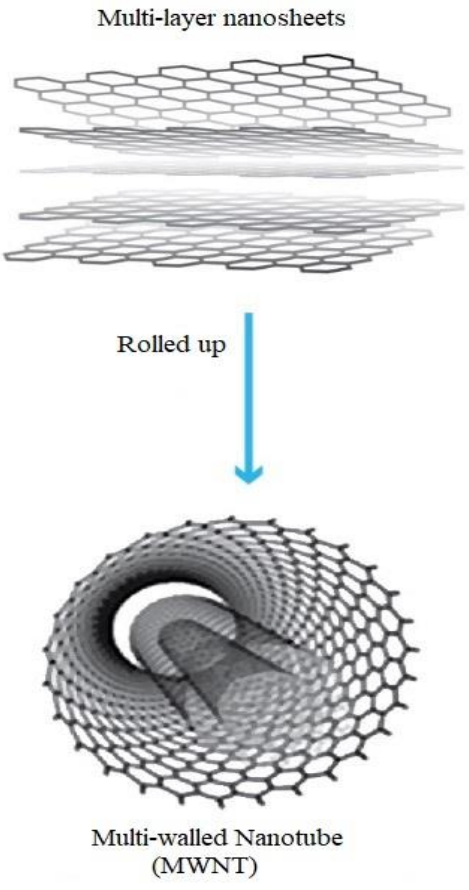

Figure 1.5: Rolled up Multi-walled nanotube from Multi-layer nanosheet

In perovskite nanostructure, the crystal structure changes according to the size of the cations (ABC) and the lengths of their bonds (A-O, B-O). To achieve an ideal cubic structure, the following equation must be met.

$$\left(r_B\sqrt{2} + r_O\right) = (r_A + r_B) = {}^{a_p}/_{\sqrt{2}} \tag{1.4}$$

$$t = \frac{(r_A + r_O)}{\sqrt{2}(r_B + r_O)} = 0.9 - 1 \tag{1.5}$$

where r_A, r_B, and r_O represent the radii of the A, B, and O ions in the lattice, respectively. Also, t and a_p are Goldschmidt tolerance factor and the lattice parameter of the perovskite unit cell. However, the equation can be utilized to calculate the lattice parameters for each perovskite material.

Also, the lattice parameter in terms of bond lengths (A - O) and (B - O) is represented as

$$a_p = 2(B - O) \text{ and } \sqrt{2a_p} = 2(A - O) \tag{1.6}$$

Where

$$\frac{(A-O)}{(B-O)} = \sqrt{2} \text{ or } \frac{(A-O)}{\sqrt{2}(B-O)} \tag{1.7}$$

1.1.2 Mechanical properties

Firstly, the tensile (EA), bending (EI), and torsional (GJ) rigidities of smart nanotubes can be determined through various methods such as experimental tests, molecular dynamics simulations, ab initio simulations, nanoscale finite element modeling (NSFEM), or density functional theory (DFT). In these tests, an axial tensile force (F_x), a transverse force (F_z), and a torsional moment $(M_\theta)$are applied to one end of the nanotube (see Figure (1.6)). Boundary conditions at the opposite end restrict all degrees of freedom for the nodes involved. Finite element analysis allows for the determination of the axial displacement (u_x), transverse displacement (u_z), and twist angle (θ) during these tests. The rigidities $(EA, EI, and\ GJ)$ of the nanotubes with length (L) can be expressed as follows[1]

$$EA = \frac{F_x.L}{u_x} \tag{1.8}$$

$$EI = \frac{F_z.L}{3.u_z} \tag{1.9}$$

$$EG = \frac{M_\theta.L}{\theta} \tag{1.10}$$

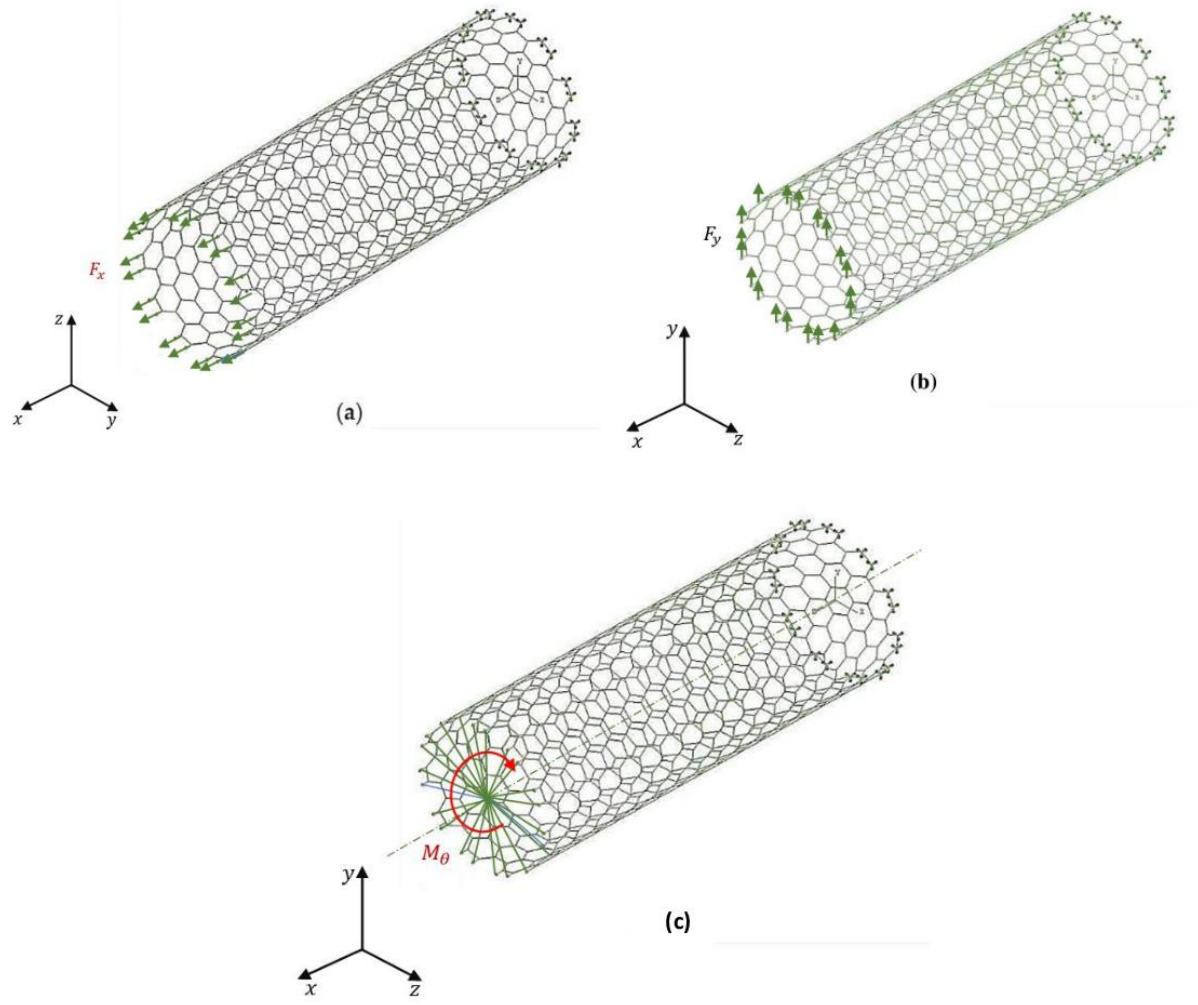

Figure 1.6: Schematic of applied testing forces to determine the mechanical properties of a nanotube: (a) axial force, (b) transverse force, and (c) torsional moment.[1]

The tensile EA, bending EI, and torsional GJ rigidities from Equations (1.9), (1.10), and (1.11) are necessary to determine the Young's modulus (E) and shear modulus (G) of the smart NTs as follows

$$E = \frac{E.A}{\pi.h\sqrt{8.\left(\frac{EI}{EA}\right) - h^2}} \tag{1.11}$$

$$G = \frac{G.J}{2\pi.h\left(\frac{EI}{EA}\right)\sqrt{8.\left(\frac{EI}{EA}\right) - h^2}} \tag{1.12}$$

Furthermore, the Poisson's ratio (ν) can be determined using the bending and torsional rigidity values with the following equation.

$$\nu = \frac{E}{2.G} - 1 = \frac{EI}{GJ} - 1 \tag{1.13}$$

Given the uncertainty regarding the NT wall thickness values, the surface Young's and shear modulus must be determined. These parameters provide a more reliable description of the mechanical response of the Smart NTs, as they are independent of wall thickness. Assuming that $h^2 \ll \left(\frac{EI}{EA}\right)$ and that the term in equations (1.12) and (1.13) can be neglected, the surface Young's modulus (E_s) and shear modulus (G_s) are determined as follows:

$$E_s = E.h = \frac{EA}{\pi\sqrt{8\left(\frac{EI}{EA}\right)}} \tag{1.14}$$

$$G_s = G.h = \frac{GJ}{2\pi\left(\frac{EI}{EA}\right)\sqrt{8\left(\frac{EI}{EA}\right)}} \tag{1.15}$$

Based on our literature review, numerous papers investigate the mechanical properties of smart nanostructures using multiple theories and techniques. Yeau-Ren Jeng et al.[25] examined the mechanical properties of (n,0) and (n,n) GaN nanotubes using classical molecular dynamic simulations with the realistic Tersoff many-body potential model. The results indicate that mechanical properties, such as Young's modulus, are insensitive to the wrapping angle under small strain conditions. However, the wrapping angle significantly influences these mechanical properties under large strain conditions. Zhiguo Wang et al.[26] studied the tensile mechanical attitude of single-walled gallium nitride (SWGaN) nanotubes under coupled tension-torsion employing molecular dynamics simulations with an experimental potential. Their findings reveal that a small torsion rate does not impact the tensile behavior of GaN nanotubes. Specifically, at low temperatures, the nanotubes exhibit brittle properties, whereas at high temperatures, they behave as ductile materials. Shang-Chao Hung et al.[27] used the nanoindentation technique to determine the elastic modulus and measure the compression buckling energy of gallium nitride nanotubes. However, the mechanical properties of single-walled boron nitride nanotubes have been extensively studied in the literature. Meng Zheng et al.[28] used atomic force microscopy to evaluate the effective radial elastic moduli of single-walled boron nitride nanotubes (SW-BNNTs). Their nanomechanical measurements demonstrated the radial deformation of individual SW-BNNTs in both elastic and plastic regimes. Xiaoming Chen et al.[29] examined the effects of high temperature on the structural and mechanical characteristics of boron nitride nanotubes (BNNTs) spanning a comprehensive size range from the nanoscale to the macroscale, employing an array of both in situ and ex-situ material characterization methods. Veena Verma et al.[30] employed the Tersoff-Brenner potential to calculate the Young's modulus and shear modulus of armchair and zigzag single-walled boron nitride nanotubes with varying radii. Additionally, they investigated the impact of nanotube diameter.Sakharova et al.[1] calculated the elastic properties-including rigidities, surface young's modulus, shear modulus, and poisson's ration-of single-walled nanotube made of boron nitride, aluminum nitride, gallium nitride, indium nitride, and thallium nitride using a nanoscale contium modeling technique . Petrushenko et al.[31] employed PBE/SVP calculations to investigate the ionization effects on the mechanical properties of finite-length SWCNT, SWBNNT, and SWSiCNT. Their findings reveal that ionization significantly impacts bulk and shear moduli as well as Poisson's ratio, while the changes in Young's modulus are

comparatively less pronounced. The study of SWZnONT's mechanical properties has also drawn substantial interest from researchers. Mirnezhad et al.[32] studied the effects of four distinct hydrogen adsorption states on the surface Young's modulus and Poisson's ratio of single-walled zinc oxide nanotubes (SWZnONTs) with varying chiralities. Using molecular mechanics, they derived analytical expressions for these mechanical properties. Also, Mirnezhad et al. studied the effects of four distinct hydrogen adsorption states on the surface of Young's modulus and Poisson's ratio of single-walled zinc oxide nanotubes (SWZnONTs) with varying chiralities. Using molecular mechanics, they derived analytical expressions for these mechanical properties. Prajapati et al.[33] utilized the Lennard-Jones interaction potential methodology to predict ZnONTs' second and third-order elastic coefficients. They then used the SOECs to calculate the bulk modulus, Young's, and shear modulus of ZnONTs. Wen et al.[34] employed first-principles computations to explore the elastic modulus of the armchair and zigzag (SWZnONTs). Their findings revealed that an increase in nanotube diameter leads to a higher Young's modulus, which is inversely proportional to the Zn-O bond length.

1.1.3 piezoelectric properties

Piezoelectricity is a phenomenon where smart materials accumulate an electric charge in response to mechanical stress. This effect is reversible; materials demonstrating the piezoelectric effect can also exhibit the reverse piezoelectric effect, where an applied electric field induces mechanical strain within the material. In the mechanics of continuous media, mechanical stress is related to mechanical strain via the elastic tensor. In smart materials, the piezoelectric tensor connects mechanical stress and electric displacement to electrical fields and mechanical strain, respectively. This tensor contains the longitudinal, transverse, and shear coefficients to respond to normal and shear stress, as shown by the following equation.

$$\begin{pmatrix} e_{11} & e_{12} & e_{13} & e_{14} & e_{15} & e_{16} \\ e_{21} & e_{22} & e_{23} & e_{24} & e_{25} & e_{26} \\ e_{31} & e_{32} & e_{33} & e_{34} & e_{35} & e_{36} \end{pmatrix} \tag{1.16}$$

Where

$e_{ij} = e_{ji}$ If $i = j$ then the constants are the longitudinal piezoelectric coefficients
If I,j=1,2,3 then the constants are the transverse piezoelectric coefficients
If $i = 1,2,3$ and $j = 4,5,6$ then the constants are the shear piezoelectric coefficients

According to the Cartesian coordinate system and assuming an infinitesimal volume of piezoelectric material polarized in one direction, the piezoelectric tensor can be simplified as follows.

The polarization in x direction

$$\begin{pmatrix} e_{11} & e_{12} & e_{13} & 0 & 0 & 0 \\ 0 & 0 & 0 & e_{24} & 0 & 0 \\ 0 & 0 & 0 & 0 & e_{35} & 0 \end{pmatrix} \tag{1.17}$$

The polarization in y direction

$$\begin{pmatrix} 0 & 0 & 0 & 0 & e_{15} & 0 \\ e_{21} & e_{22} & e_{23} & 0 & 0 & 0 \\ 0 & 0 & 0 & e_{34} & 0 & 0 \end{pmatrix} \tag{1.18}$$

The polarization in z direction

$$\begin{pmatrix} 0 & 0 & 0 & 0 & e_{15} & 0 \\ 0 & 0 & 0 & e_{24} & 0 & 0 \\ e_{31} & e_{32} & e_{33} & 0 & 0 & 0 \end{pmatrix} \tag{1.19}$$

The piezoelectric coefficients tensor can be derived from the Maxwell equations as follows.

$$e_{ij} = \left(\frac{\partial P_i}{\partial \varepsilon_j}\right)^{E,T} = -\left(\frac{\partial \sigma_j}{\partial E_i}\right)^{\varepsilon,T} \tag{1.20}$$

Where P_i, and E_i the polarization and applied electric field in i direction. Also, σ_j and ε_j are the mechanical stress and strain, respectively. The superscripts E, T, and ε denote the simulation conditions of fixed electric field, temperature, and strain, respectively. On the other hand, smart materials also exhibit piezomagnetic properties. To determine these properties, the same methodology used for identifying piezoelectric properties should be applied. According to our literature assessment, multiple studies have investigated the piezoelectric properties of smart nanostructures utilizing a variety of theories and approaches. Zhang et al.[35] examined the piezoelectric potential of strained intrinsic gallium nitride (GaN) nanotubes using both analytical and numerical methods. The physical properties utilized in their study, derived from molecular dynamics simulations (MDSs), were found to be influenced by temperature and the nanotube's wall thickness. Kundalwal et al.[36] investigated the axial piezoelectric coefficients of boron nitride nanotubes (BNNTs) with vacancies using molecular dynamics simulations (MDS) with a Tersoff potential force field. They considered the impact of diameter and the various types and positions of atom vacancies. Yamakov et al.[37] explored the piezoelectric characteristics of multiwall boron-nitride nanotubes (MWBNNT) using a standard molecular dynamics model with a dipole potential energy component that changed with strain. Salavati et al.[38] examined the piezoelectric coefficients of isolated zigzag BNNT bonds using molecular mechanics simulations, modeled as an equivalent piezoelectric beam element. Utilizing the novel electrostructural analogy technique, Jafari et al.[39] investigated the piezoelectric coefficients of zigzag boron nitride nanotubes (BNNTs). Xiang et al.[40] explored the piezoelectric properties of BNNT using the hybrid density functional procedure (B3LYP). Zhang[41] investigated the impact of the electrocaloric effect on the piezoelectric potential of hexagonal boron nitride (BN) nanotubes using molecular dynamics (MD) simulations and analytical methods. Additionally, Nakhmanson et al.[42] explored the spontaneous polarization and piezoelectricity in boron nitride nanotubes using ab initio calculations. Zhang and Meguid[43] investigated the effect of the number of tube layers on the piezoelectric properties of (MWBNNT). The piezoelectric properties of SWZnONT have also attracted significant research attention. Tu and Hu[44] demonstrate that the piezoelectric properties of SWZONTs depend on their chirality. Additionally, they indicate that twists around the nanotube in both armchair and chiral configurations induce axial polarizations.

1.1.4 dielectric properties

At the macroscopic scale, the dielectric properties of a smart material pertain to its capacity to store and dissipate electrical energy when an electric field is applied. At the nanoscopic scale, these properties describe a crystal's ability to rearrange its charge distribution in response to an electric field. There is a significant reduction in the dielectric tensor component along the polarization direction, attributed to the reduced degrees of freedom parallel to the crystal's spontaneous dipole. the dielectric tensor can be expressed in the matrix form the dielectric tensor can be expressed in the matrix form as follow

$$\begin{pmatrix} \epsilon^{\perp} & 0 & 0 \\ 0 & \epsilon^{\perp} & 0 \\ 0 & 0 & \epsilon^{\parallel} \end{pmatrix} \tag{1.21}$$

Where $\epsilon^{\perp}$ and $\epsilon^{\parallel}$ are the orthogonal and parallel components dielectric tensor, respectively. Based on previous studies. Lan et al.[45] conducted comprehensive ab initio finite electric-field calculations to investigate boron nitride nanotubes' static transverse dielectric properties using the sawtooth potential approach. Yang[46] used the molecular dynamics simulation with several Tersoff-like potential models and Born effective charges to identify the dielectric properties of a SW BNNT. Lacivita et al.[47] utilized a Gaussian basis set and the B3LYP hybrid functional, as implemented in the periodic ab initio CRYSTAL code, to examine the dielectric properties of (SWZnONT). Mao et al.[48] used first-principles methods within the pseudopotential density functional theory (DFT) framework to investigate the dielectric function of a (6,6) armchair single-walled zinc oxide nanotube (SWZONT).

1.1.5 The thermal properties

The thermal properties of a substance include its behavior and characteristics in reaction to temperature variations. These properties include

- Thermal conductivity: this evaluates a material's capacity to conduct heat. High thermal conductivity implies that the material easily conducts heat, whereas low thermal conductivity indicates superior insulating characteristics.
- Specific Heat Capacity: This is the quantity of heat necessary to change the temperature of a material by a specific amount. A high specific heat capacity indicates that the material can absorb a lot of heat without causing a major temperature increase.
- Thermal Expansion: This term refers to how a material's dimensions change with temperature. Materials with high thermal expansion coefficients expand or contract dramatically as temperature changes.
- Thermal diffusivity: This is a combination of thermal conductivity, density, and specific heat capacity that describes how quickly a material's temperature can be adjusted to match that of its surroundings.
- Melting Point: The temperature at which the material changes from a solid to a liquid.

- Thermal Stability: This refers to the material's ability to maintain its qualities at high temperatures without degrading.

Based on our literature review, various studies have explored smart nanotubes' thermal properties, employing diverse theories and approaches. Zhou et al.[49] explored the phonon thermal conductivity of gallium nitride (GaN) nanotubes with diameters ranging from a few to 120 nanometers, employing the Boltzmann transport equation. Chang et al.[50] utilized a microfabricated test fixture to measure the temperature-dependent thermal conductivity of individual multiwall boron nitride nanotubes through direct transmission electron microscopy. Huang et al.[51] employed molecular dynamics (MD) simulations to investigate the impact and mechanisms of tubular configuration, temperature, length, diameter, and chirality on the thermal conductivity of BNNTs. Stewart et al.[52] utilized first-principles calculations to examine the effect of isotopic composition on the thermal conductivity of boron nitride nanotubes. Jiang et al.[53] conducted a theoretical study on the thermal conductivity of (SWBNTs) utilizing kinetic theory. Chang et al.[54] investigated the temperature-dependent thermal conductivity of mats made from boron-carbon-nitride (B-C-N) and boron-nitride (BN) nanotubes.

1.2 Dynamical response of Rotating nanosystem based on atomistic simulation

In recent years, many nanodevices have emerged due to their use in various fields, including nanomedicine, nanoelectronics, biomaterials, energy production, and consumer products. Numerous innovative nanodevices feature rotating components, which are pivotal for efficient energy production and conversion on a microscopic scale. This technological requirement has prompted engineers and researchers to concentrate on developing and comprehensively studying the dynamic behaviors exhibited by various rotating nanosystems. Prime examples of such systems include nanogears, which enable precise mechanical motion; nanomotors, which convert energy into movement; nano-bearings, which reduce friction in small mechanical systems; nano-turbines, which harness fluid or gas flow to generate power; and rotary nano-transmission systems, which ensure efficient transfer of mechanical energy. These extensive R&D endeavors are essential to improving the functionality and applications of nanodevices, pushing the boundaries of what is technologically possible, and opening new frontiers in science and industry. Using molecular dynamics simulations, Tuzun et al.[55] simulated the dynamic response of a nano-bearing system, considering frictional properties that were dependent on size, temperature, and velocity. The nano-bearing system consists of an inner carbon nanotube serving as the shaft and an outer carbon nanotube acting as the stator, as illustrated in **Figure** 1.7 Zhang et al.[56] employed molecular dynamics simulations to investigate the impact of temperature on the performance of rotating (DWCNTs) as nano-bearings. Also, Zhu et al.[57] utilized molecular dynamics simulations to examine the thermal effects of rotational friction in a molecular bearing consisting of DWCNTs. Huang[58] investigated the coaxial stability of a nano-bearing system consisting of (DWCNTs). Yao and Huang[59] examined the coaxial stability of a DWCNT-based nano-bearing subjected to two-axis-deviation perturbations. Using molecular dynamics (MD) simulations, Cook et al.[60] studied the friction mechanisms in rotating carbon nanotube bearings.

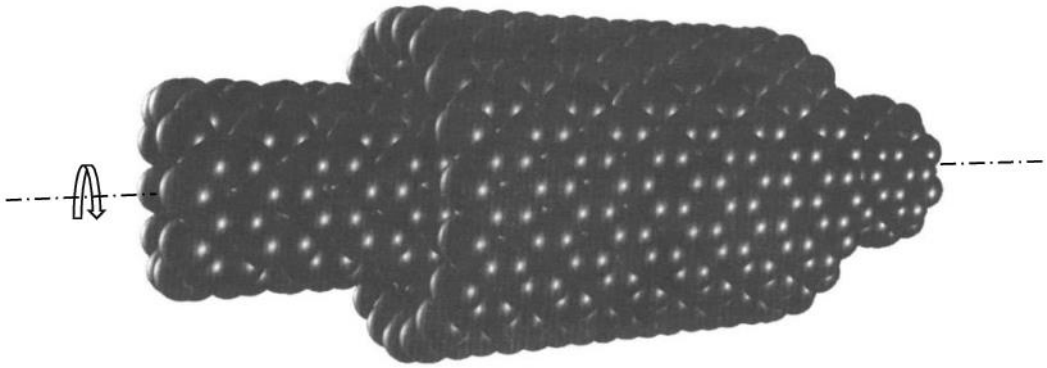

Figure 1.7: Diagram of a basic graphite molecular bearing.[55]

Another spinning nanodevice is the nanogear system. Various studies have investigated its dynamic behavior using molecular dynamics simulations. For example, Taşcı et al.[2] examined the stability of two nanogears and two nanotubes serving as shafts through molecular dynamics simulations. **Figure** 1.8 presents a schematic of the initial system views for simulating 6-toothed nanogears. Also, Han et al.[61] utilized molecular dynamics simulations to explore the properties and design space of molecular gears made from carbon nanotubes, with teeth added through a benzyne reaction known to occur with C_{60}. Fu et al.[62] developed an innovative nano wheel gear with ultrahigh speed, simple assembly, and low friction by leveraging the principle that carbon nanotubes (CNTs) suspended in aqueous solutions can rotate in response to water dipoles induced by rotating electric fields. Jiao et al.[63] employed molecular dynamics simulations to examine the dynamic behavior of a nanogear drive system constructed from carbon nanotubes (CNTs), consisting of a motor and a nano bearing.

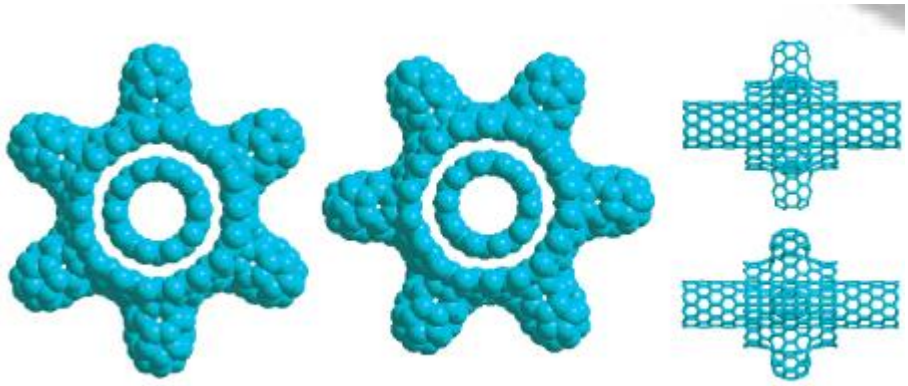

Figure 1.8: Preliminary system perspectives of the 6-toothed nanogears simulation.[2]

One of the most prominent rotary nanodevices is the nanomotor. Numerous researchers have investigated its dynamic behaviors using molecular dynamics simulations. These nanomotors are exclusively based on carbon nanotubes. Negi et al.[3] employed molecular dynamics simulation to investigate the rotational motion of a double-walled carbon nanotube (DWCNT) motor. This motor comprises two coaxial carbon nanotubes, with the inner tube functioning as a shaft and the outer tube acting as a sleeve, see **Figure** 1.9 The rotational motion within the system is induced by applying a sinusoidally varying electric field. Also, S. Negi et al. conducted molecular dynamics simulations on a double-walled carbon nanotube (DWNT)

motor, driven by an externally applied sinusoidally varying electric field, within a 'frozen' sleeve configuration. Their simulations revealed that achieving unidirectional, motor-like rotation requires operation within a specific 'useful' region in the parameter space defined by the amplitude and frequency of the applied electric field. Holek et al.[64] simulated the interactions of frictional, van der Waals, and thermal forces and the noise effects in a nanomotor system comprising two coaxial carbon nanotubes of differing lengths. Cai et al.[65] proposed a probe test method to measure the rotation of a thermal carbon nanotube-based nanomotor, considering the centrifugal effect. Also, Cai et al.[66] investigated the rotation of a nanomotor where two outer carbon nanotubes function as the stator and an inner carbon nanotube serves as the rotor. Fu et al.[67] designed a Y-shaped nanomotor system based on carbon nanotubes immersed in an aqueous solution. They used molecular dynamics simulations to analyze systems with varying Y-shaped structure angles. Finally, Cai et al. determined the rotational acceleration of a carbon nanotube (CNT)-based nanomotor using two methods. First, they applied inward radial deviation (IRD) to some of the atoms at the edges of the CNT stators, which confine and support the rotor tube. Second, they used a rotating electric field on the water box where the bladed segment of the rotor is submerged.[68]

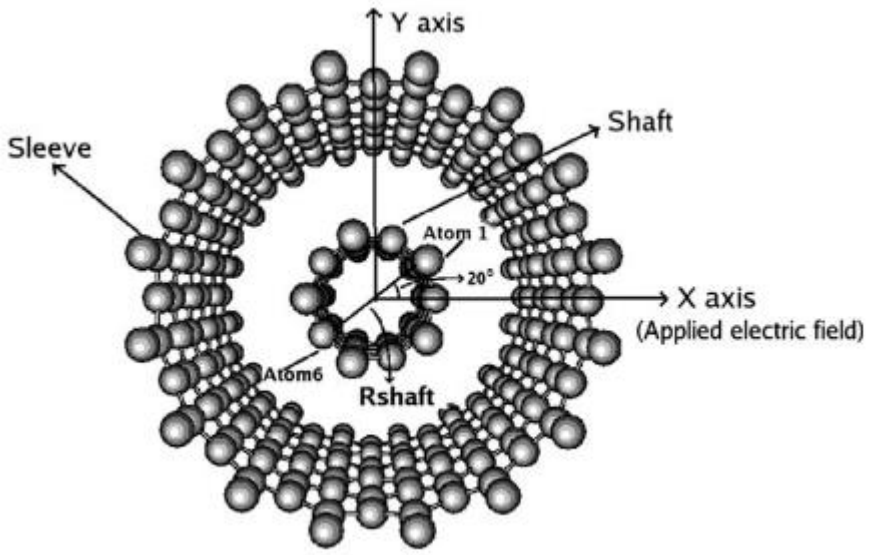

Figure 1.9: End-on view of the DWNT arrangement: At time t = 0 s, a sinusoidally varying electric field is applied in the x direction to atoms 1 and 6. The line connecting these diametrically opposite atoms forms a 20° angle with the direction of the applied electric field (X-axis).[3]

In nanotechnology, nanomotors, nano bearings, and nanogears can be used to manufacture various rotating nanodevices. Notably, nano turbines and nanopumps are significant devices in this field. Li et al.[69] constructed a fluid-powered nanoturbine using carbon nanotubes and graphene nanoblades. Molecular dynamics simulations of this model system were used to objectively investigate the nanoturbine's rotating motion. Niu et al.[70] employed molecular dynamics simulations to investigate the nano-pumping process of the C20 molecule within carbon nanotubes under varying electric fields and atomic defects. They analyzed the C20 molecule's nano-pumping process by observing changes in kinetic energy, potential energy, entropy, stress, temperature, and internal energy. Lohrasebi and Jamali[71]

utilized molecular dynamics simulations to investigate the functioning of a rotary nanopump made up of three coaxial carbon nanotubes and multiple graphene blades. On the other hand, Tu et al.[72] developed a porous nanofluidic desalination device using a spinning carbon nanotube membrane filter (SCNT-MF) for reverse osmosis, effectively transforming salt water into fresh water.(see **Figure** 1.10)

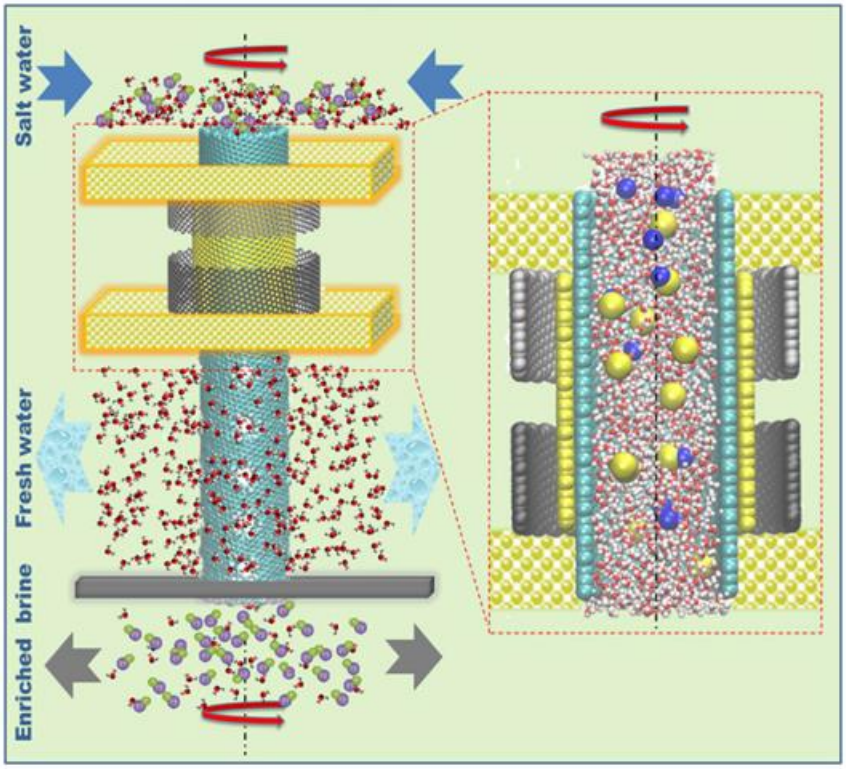

Figure 1.10: Diagram of the design concept for the rotating CNT membrane filter and its desalination mechanism, based on the operating principle of the double-walled rotating CNT.[73]

One of the most important nanodevices that can provide power and torque for motion is the Rotation Transmission Nanosystem (RTS). This system features an independent single-walled carbon nanotube (SWCNT) acting as a nanomotor and a set of coaxially arranged double-walled carbon nanotubes (DWCNTs) functioning as nanobearings. In the proposed RTS, the transfer of rotational energy from the motors to the rotors is facilitated by hydrogen atoms at the ends of the motors and rotors.(see **Figure** (1.11)) Cai et al.[74] demonstrated that the hydrogen interaction between the motor and rotor was too weak to ensure that the rotor achieved the same rotational frequency as the motor, as shown in **Figure** 1.11(c) . In another study, Yin et al.[75] examined similar structures, where the end atoms of the motor and rotor were not hydrogenated, as illustrated in **Figure** 1.11(d). They found that the carbon atoms on the adjacent ends of the motor and rotor bonded, resulting in the rotor achieving synchronous rotation under the motor's excitation.

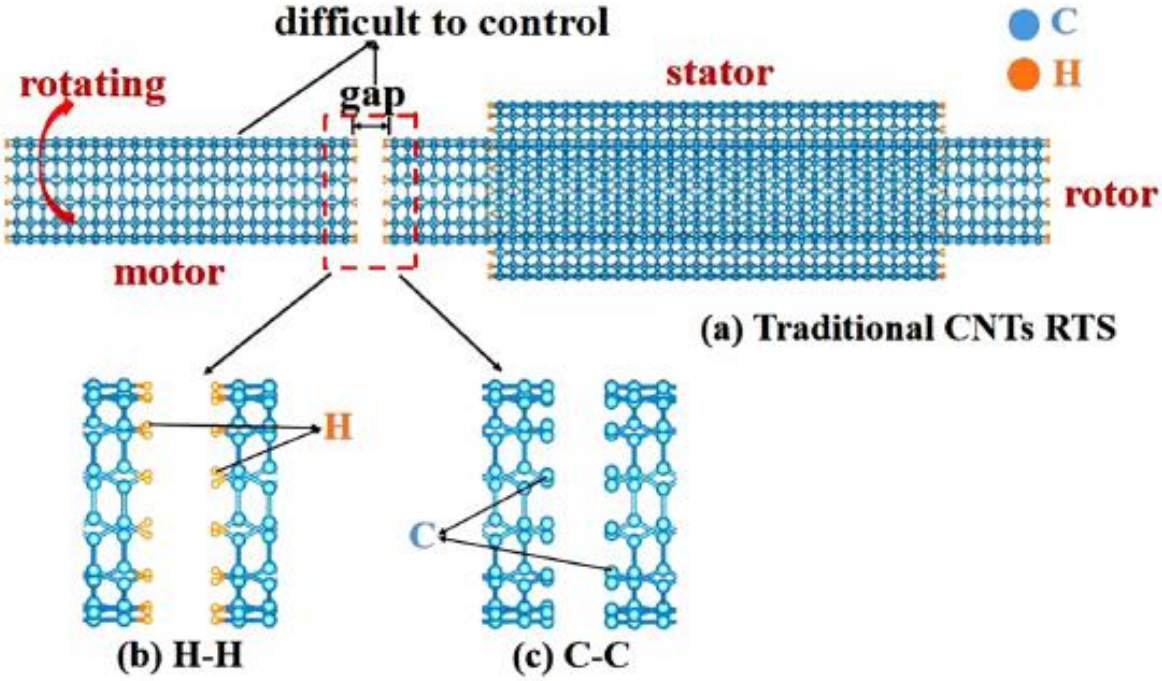

Figure 1.11: Schematic diagram of a conventional rotational transmission nano-system (RTS) based on carbon nanotubes (CNTs): (a) traditional CNTs RTS, (b) both motor and rotor ends with H–H bonds, and (c) both motor and rotor ends with C–C bonds.[4]

Due to the excellent piezo-magneto-electric, thermal, and mechanical properties of smart BNNT, Zheng et al.[4] introduced BNNTs as nanomotors for the first time to develop a new RTS using MD simulation. This innovative system comprises heterogeneous triple-walled nanotubes (TWNTs), as depicted in **Figure** 1.12. The inner nanotube, a CNT, acts as the rotor; the middle nanotube, a BNNT, functions as the motor; and the outer nanotube, another CNT, serves as the stator. The transmission between the motor and the rotor is achieved through interlayer van der Waals interactions and end effects. Additionally, the system provides a specific stable speed output and remains stable at temperatures ranging from 100K to 600K, thanks to the exceptional thermal and piezoelectric properties of BNNTs.

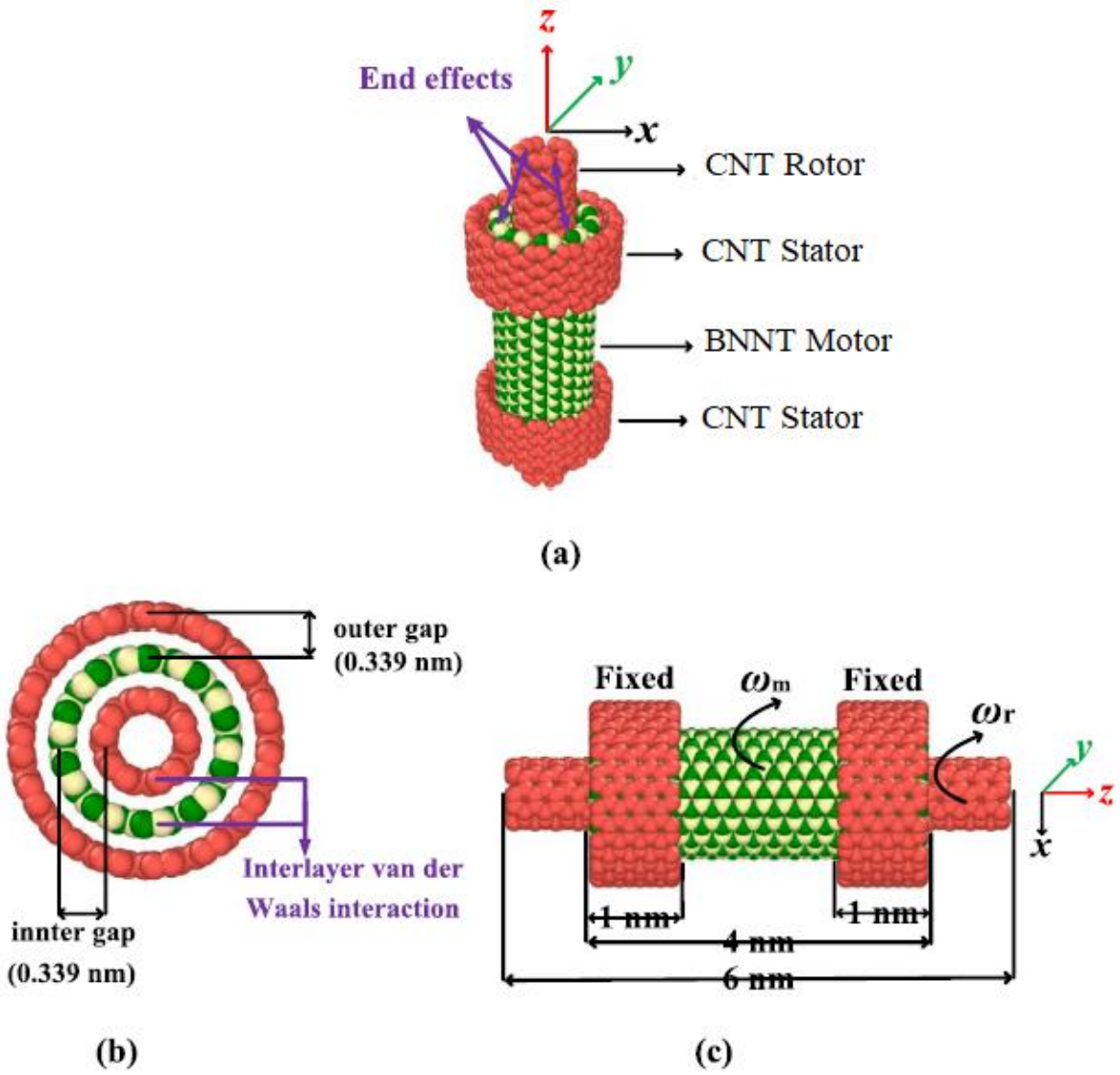

Figure 1.12: Schematic diagram of a heterogeneous rotational transmission nano-system (RTS) of CNT@BNNT@CNT: (a) 3D view, (b) left view, and (c) front view.[4]

As illustrated in the **Figure** 1.13, Zheng et al.[5] Also underestimated is shielding gas's influence on the same system's dynamic behavior in a helium environment. Their molecular dynamics simulation shows that the rotor's output signal stays stable when the gas density is below a certain level, and the rotation transmission ratio (RRT) of the rotor transmission system (RTS) can reach 1. However, when the gas density exceeds this critical range, the rotor's output signal becomes unstable due to a significant drop in the RRT caused by increased friction between helium and the RTS.

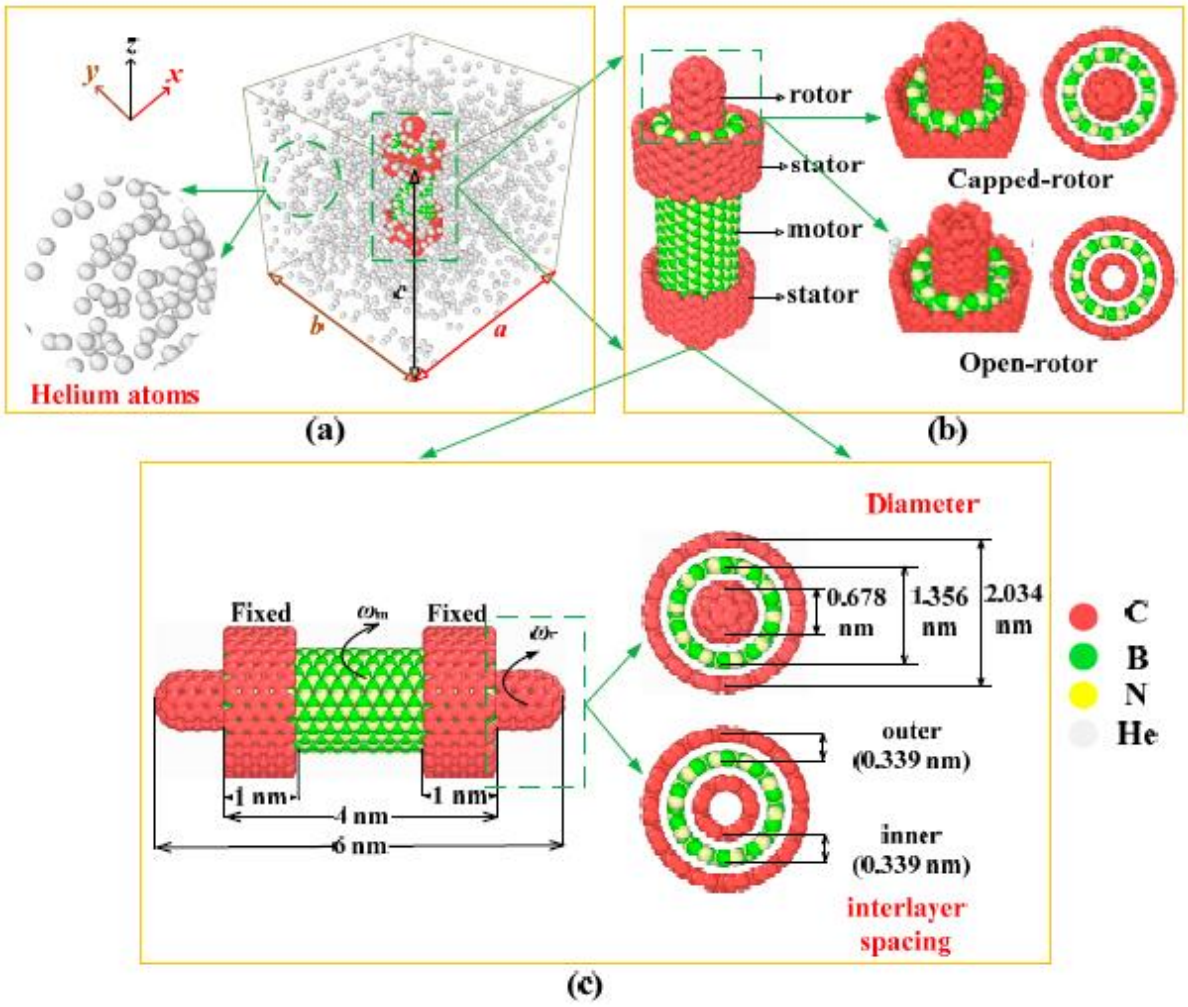

Figure 1.13: Rotational transmission nano-system (RTS) model composed of CNT (5, 5)/BNNT (10, 10)/CNT (15, 15): (a) RTS model in a helium environment, (b) RTS model with various rotor end structures, and (c) structural parameters of the RTS model.[5]

1.3 Dynamical response of rotating smart nanotube based on non-classical continuum mechanics

All the studies as mentioned above employed atomistic simulation approaches to understand the dynamic response of rotating nanosystems and devices. While molecular dynamics (MD) simulations are currently the most feasible theoretical method, they can be both costly and time-consuming. As an alternative, various non-classical continuum mechanics theories—such as the modified couple stress theory,[76] Eringen's nonlocal theory,[77] and strain gradient theory[78]—have been developed to investigate the dynamic behavior of nanostructures. In this review, we will examine the existing research on the vibrational behavior of rotating smart nanotubes using these non-classical continuum mechanics approaches. Shojaeefard et al.[79] explored how angular velocity, length scale parameter, external voltage, external amperage, FG power index, and viscoelastic factors affect the free vibration characteristics of a high speeds rotating functionally graded (FG) piezomagnetic nanotube made from $BaTiO_3$ and $CoFe_2O_4$ perovskite materials. In other words, Shojaeefard et al.[80] studied the same nanotube placed on a Winkler foundation and subjected to thermo-electro-magneto-

elastic conditions, using the modified couple stress theory based on the first-order shear deformation shell theory for their analysis. Similarly, Habibi et al.[81] employed Taylor's series expansion based on first-order shear deformation shell theory to examine the vibration properties of a high-speed spinning GNPRC nanotube coupled with a $BiTiO_3$–$CoFe_2O_4$ perovskite piezoelectric layer. Mahinzare et al.[82] combined a first-order shear-deformable shell model with nonlocal strain gradient theory (NSGT) to analyze the vibrations of a rotating smart nanotube made from $BiTiO_3$–$CoFe_2O_4$ perovskite piezoelectric functionally graded material (FGM). Additionally, Sadeghzadeh and Mahinzare[83] utilized first-order shear deformation shell theory alongside NSGT and the generalized differential quadrature method (GDQM) to investigate the thermo-magneto vibrations of a rotating FG piezomagnetic nanotube composed of BaTiO3 and CoFe2O4 perovskite materials. They also[84] applied NSGT to study the vibration behavior of a rotating FG piezomagnetic nanotube made from BaTiO3 and CoFe2O4 perovskite material. Finally, Zhang et al.[85] researched the smart control and vibration analysis of a thick sandwich nanostructure featuring a honeycomb core and piezoelectric face sheets made of BiTiO3–CoFe2O4 perovskite material, using NSGT based on higher-order shear deformation shell theory.

1.4 Gaps identification based on existing literature

In the study of spinning smart nanostructures, a significant research gap exists due to the lack of comprehensive studies on rotating smart nano-shafts based on smart single-walled nanotubes. It is noted that all rotating nanosystems rely on single-walled nanotubes or configurations of multiple single-walled nanotubes, which offer superior mechanical properties and capabilities.

BNNT, SWZnONT, and GANNT nanotubes exhibit exceptional piezoelectric, magnetic, and thermal properties, making them highly suitable for applications in spinning nanoelectromechanical systems, nanothermal rotary actuators, rotation transmission nanosystems, and nanogears. Such integration is promising for enhancing the stability and durability of these nanodevices.

1.5 Aim and Objectives

The primary goal of this thesis is to explore the electro-mechanical coupling effect on rotating smart nano-shafts under various conditions. To achieve this, the following objectives were pursued

- Develop a new mathematical formulation based on Timoshenko beams theory, Maxwell electrostatic equation, and nonlocal strain gradient theory.
- Develop a semi-analytical solution using the Galerkin closed-form method to determine the vibration response of the system.
- Explore the vibration response on rotation smart nano-shaft based on SWZnONT.
- Explore the vibration response on rotation smart nano-shaft based on SWBNNT.

1.6 Summary

This chapter offers a comprehensive examination of smart nanotubes' structure and physical properties, along with an in-depth review of nanoscale machines, including nanomotors, nanogears, nanobearings, and nanotransmission systems, analyzed using atomistic methods. We present a historical overview of carbon nanotubes in rotating devices, culminating in the pioneering use of smart nanotubes. The unique properties of smart nanotubes and their significance in rotating devices are elucidated. Our well-defined objectives aim to address existing research gaps, effectively setting the stage for focused and purposeful investigation. This chapter provides a solid foundation for subsequent studies in the field.

The following chapter will introduce various theories and methods employed in modeling rotating smart nanoshafts.

Chapter 2:Theorical Fundation

Objective:

This chapter is divided into three main sections. First, it explores the size-dependent piezoelectric effect and the electro-mechanical coupling equation that links mechanical strain and stress to electrical displacement and fields. Second, it delves into various nanoscale modeling theories, providing explanations and definitions. Finally, the third section introduces the non-classical piezoelectric continuum model, designed to capture both piezoelectric and small-scale effects.

2.1 Piezoelectric materials.
2.2 Theories of modeling the nanostructures
2.3 Spinning smart shaft based on Multi-scale piezoelectric Euler-Bernouli beams model
2.4 Summary

2.1 Piezoelectric materials

2.1.1 Piezoelectric effect

A piezoelectric material can generate an electric field as a result of mechanical deformation. Conversely, when an electric field is applied to the material, it can induce mechanical deformation (shrinking or expanding), a phenomenon known as the reverse piezoelectric effect. These materials exhibit a polarization structure that depends on the arrangement of atoms within the crystal and the formation of the crystals. In a nanocrystal, all dipoles align their polar axes in a single direction, making the crystal symmetrical.[86] **Figure** 2.1a presents a basic molecular model illustrating the direct piezoelectric effect. Before applying any external stress, the centers of gravity for the negative and positive charges within each molecule coincide, resulting in the mutual cancellation of their external effects and the appearance of an electrically neutral molecule. However, when pressure is applied to the material, its internal lattice structure deforms, separating the positive and negative centers of gravity within the molecules and forming small dipoles (**Figure** 2.1b). The opposing poles within the material cancel each other out, leading to a distribution of bound charges on the material's surfaces (**Figure** 2.1c). This process polarizes the material, generating an electric field that can convert the mechanical energy used in deforming the material into electrical energy.[6]

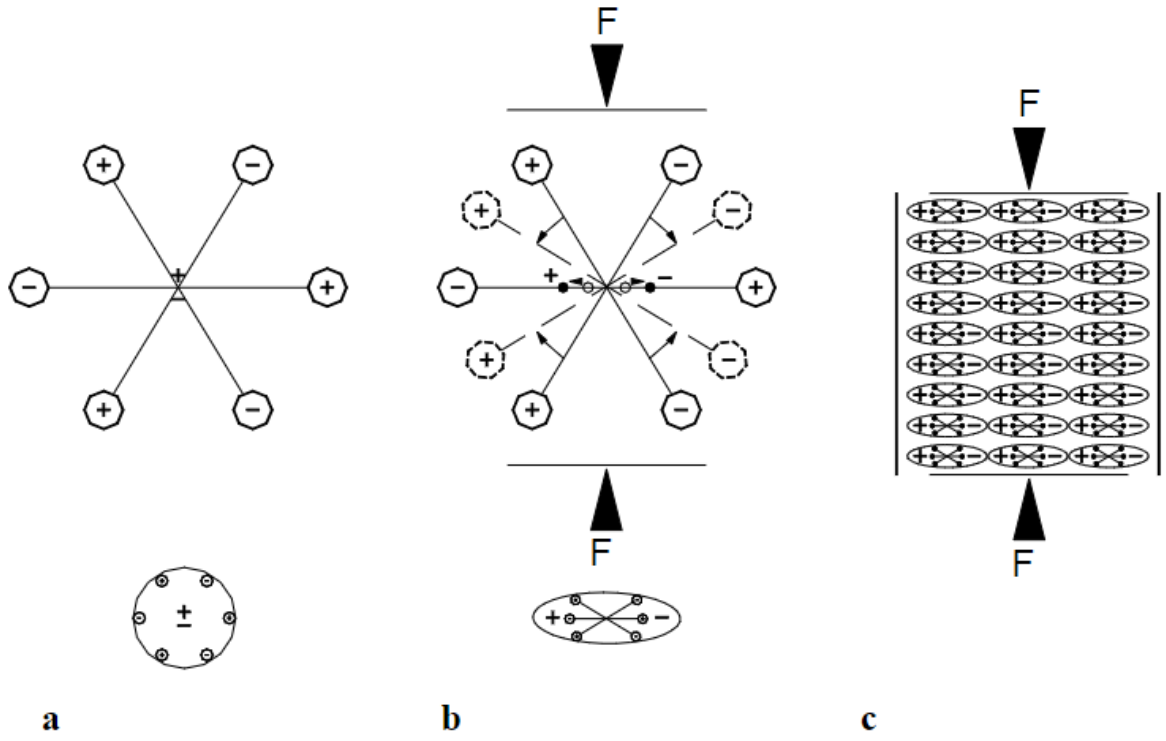

Figure 2.1 Simple molecular model illustrating the piezoelectric effect: (a) an undisturbed molecule, (b) a molecule under external force, and (c) the resulting polarization effect on the material's surfaces.[6]

Considering a cubic crystal structure as an infinitesimal volume, **Figure** 2.2 provides a schematic illustration of all longitudinal, transverse, and shear inverse piezoelectric effects, representing the various actuation modes in piezoelectric materials. When the applied electric

field aligns with the polarization direction, longitudinal extension/contraction (ΔT) and transverse extension/contraction (ΔL) occur (**Figures** 2.2(b) and (c)). Linear actuation primarily uses the longitudinal mode (ΔT) due to the significant deformation along the longitudinal axis compared to the transverse deformation (ΔL). When the applied electric field and polarization are perpendicular, shear deformation (Δx) occurs, as shown in **Figure** 2.2(d). The bending mode of actuation happens when one end of the piezo actuator is fixed (**Figure** 2.2(e)). The choice of actuation mode depends on the type of precision motion required for the specific application utilizing piezoelectric materials. **Table** 2 presents the expressions for displacement in different piezoelectric actuation modes.[7]

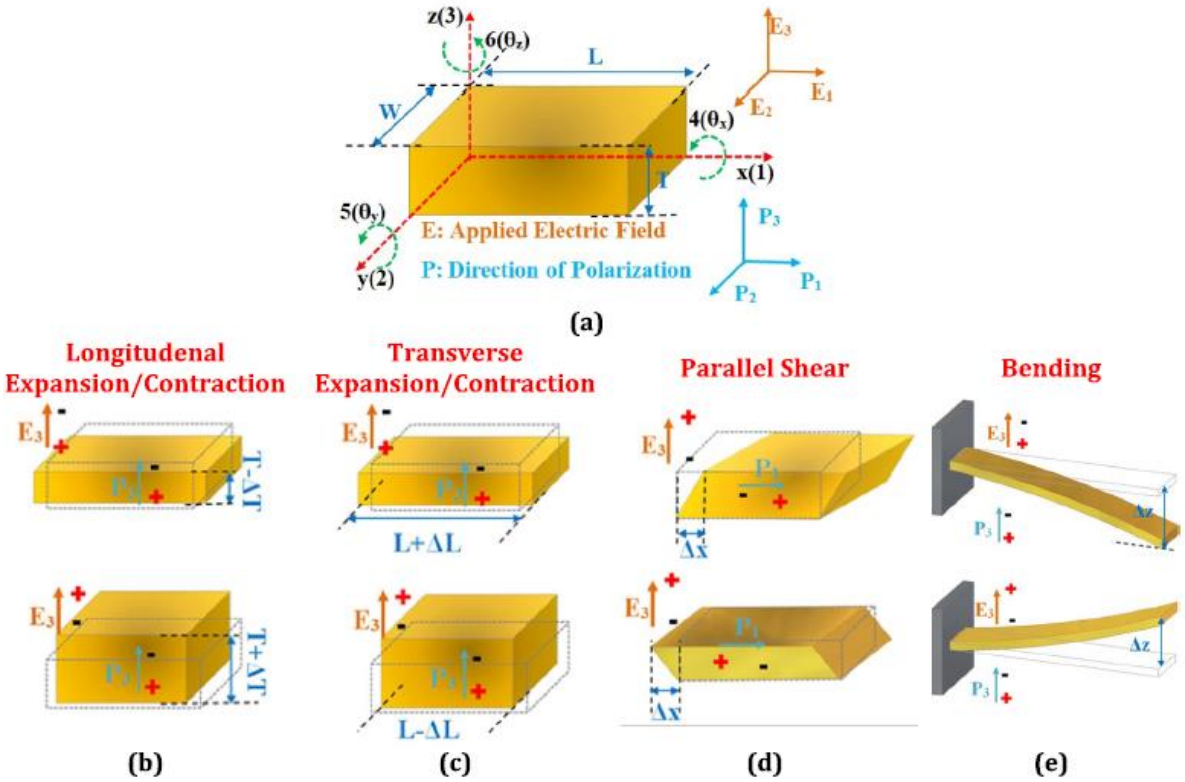

Figure 2.2: Representation of piezoelectric materials with corresponding coordinate systems and the direction of polarization/electric field: (b) Longitudinal expansion/contraction mode, (c) Transverse expansion/contraction mode, (d) Parallel shear mode, (e) Bending mode.[7]

Table 2.1: Different actuation modes of piezoelectric materials.[7]

Mode	Coupling Coefficient	Linear Expression
Longitudinal expansion/Contraction mode	e_{33}	$\Delta T = E_3 e_{33}$
Transverse expansion/Contraction mode	e_{31}	$\frac{\Delta L}{L} = \frac{\Delta w}{w} = \frac{E_3 e_{31}}{T}$
Parallel shear mode	e_{15}	$\Delta x = E_3 e_{15}$

In wurtzite bulk smart nanostructures, such as boron nitride, a local dipole moment between positive and negative atoms induces the piezoelectric effect, as illustrated in **Figure** 2.3[8]

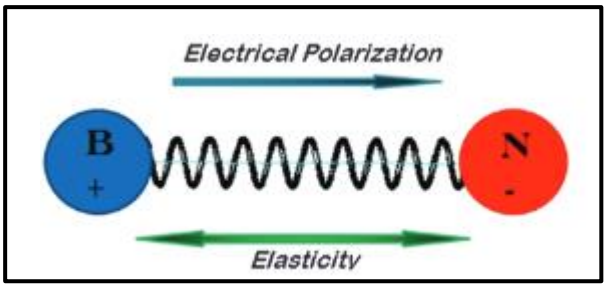

Figure 2.3: Axial piezoelectric effect resulting from electrical polarization along the bonding axis.[8]

2.1.2 Constitutive equation of a piezoelectric material

The IEEE Standard on Piezoelectricity extensively covers the constitutive equations for linear piezoelectric materials. The relationship among four field variables, stress (σ), strain (ε), electric field (E), and electric displacement (D), mathematically represents both the direct and converse piezoelectric effects. The most typical way to express these constitutive relations using Voigt notation is presented as[87]

$$\begin{pmatrix}\sigma_{xx}\\ \sigma_{yy}\\ \sigma_{zz}\\ \sigma_{yz}\\ \sigma_{xz}\\ \sigma_{xy}\end{pmatrix}=\begin{pmatrix}C_{11} & C_{12} & C_{13} & C_{14} & C_{15} & C_{16}\\ C_{21} & C_{22} & C_{23} & C_{24} & C_{25} & C_{26}\\ C_{31} & C_{32} & C_{33} & C_{34} & C_{35} & C_{36}\\ C_{41} & C_{42} & C_{43} & C_{44} & C_{45} & C_{46}\\ C_{51} & C_{52} & C_{53} & C_{54} & C_{55} & C_{56}\\ C_{61} & C_{62} & C_{63} & C_{64} & C_{65} & C_{66}\end{pmatrix}\begin{pmatrix}\varepsilon_{xx}\\ \varepsilon_{yy}\\ \varepsilon_{zz}\\ \gamma_{yz}\\ \gamma_{xz}\\ \gamma_{xy}\end{pmatrix}-\begin{pmatrix}e_{11} & e_{21} & e_{31}\\ e_{12} & e_{22} & e_{32}\\ e_{13} & e_{23} & e_{33}\\ e_{14} & e_{24} & e_{34}\\ e_{15} & e_{25} & e_{35}\\ e_{16} & e_{26} & e_{36}\end{pmatrix}\begin{pmatrix}E_x\\ E_y\\ E_z\end{pmatrix} \tag{2.1}$$

$$\begin{pmatrix}D_x\\ D_y\\ D_z\end{pmatrix}=\begin{pmatrix}e_{11} & e_{12} & e_{13} & e_{14} & e_{15} & e_{16}\\ e_{21} & e_{22} & e_{23} & e_{24} & e_{25} & e_{26}\\ e_{31} & e_{32} & e_{33} & e_{34} & e_{35} & e_{36}\end{pmatrix}\begin{pmatrix}\varepsilon_{xx}\\ \varepsilon_{yy}\\ \varepsilon_{zz}\\ \gamma_{yz}\\ \gamma_{xz}\\ \gamma_{xy}\end{pmatrix}-\begin{pmatrix}\xi_{11} & \xi_{12} & \xi_{13}\\ \xi_{21} & \xi_{22} & \xi_{23}\\ \xi_{31} & \xi_{32} & \xi_{33}\end{pmatrix}\begin{pmatrix}E_x\\ E_y\\ E_z\end{pmatrix} \tag{2.2}$$

Where $\sigma_{ij,}$ ε_{ij}, $(i,j=x,y,z)$, E_k, and D_k $(k=x,y,z)$ represent the components of stress, strain, electric fields, and electric displacements, respectively. Additionally, C_{kl} $(k,l=1,\dots,6)$, e_{kl} $(k=1,..3.\,l=1,\dots,6)$ denote the elastic and piezoelectric constants, respectively, and ξ_{kl} $(k,l=1,\dots,3)$ indicates dielectric terms.

2.1.3 Distribution of electrical potential

Assuming a piezoelectric continuum poled in the thickness direction as depicted in the **Figure** 2.4, different assumptions regarding the electric potential distribution in the thickness direction result in various mechanical models for piezoelectric coupled structures. Recently, Gopinathan et al.[88] and Wang and Quek [89] highlighted that the commonly used assumption of a uniform electric potential distribution in the longitudinal direction and a linear distribution in the flexural direction violates Maxwell's static electricity equation. In response, they proposed a quadratic or half-cosine distribution of the electric potential in the flexural direction of the structure, which has been numerically verified using FEM [22]. This proposed

distribution of the electric potential provides a precise mathematical representation of the electrical potential distribution in a piezoelectric continuum.[90]

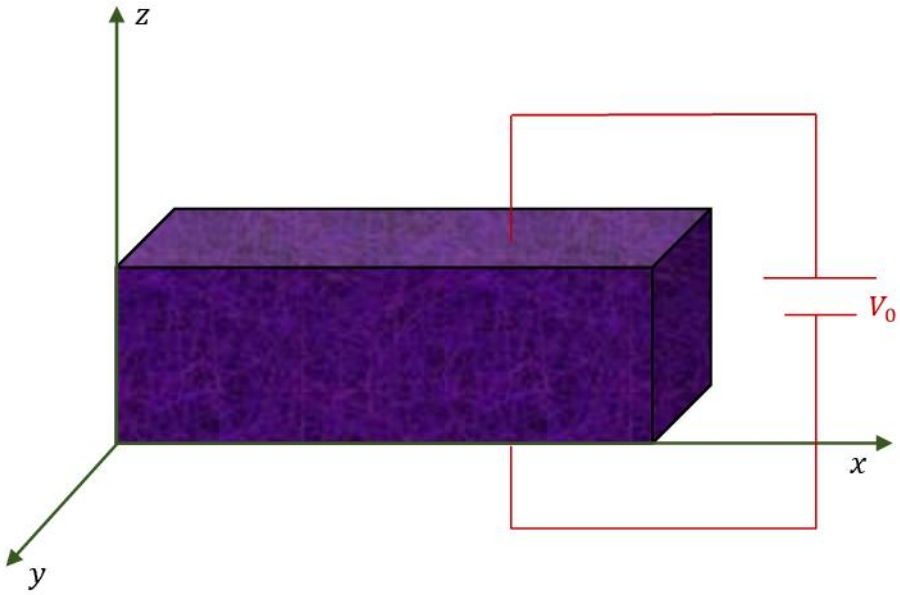

Figure 2.4: Piezoelectric continuum poled in the thickness direction

The electric potential is assumed as a combination of a half-cosine and linear variation as

$$\phi(x,y,z,t) = -cos\left(\frac{\pi z}{h}\right)\phi(x,y) + \frac{2z}{h}V_0 \qquad 2.3$$

Here, z is measured from the center of the piezoelectric layer along the global $z-axis$; h represents the layer's thickness; $\phi(x,y)$ denotes the spatial variation of the electric potential in the global x and y axis. V_0 is the external electric voltage applied to the electrodes.

2.2 Theories of modeling the nanostructures

Researchers have developed various approaches, including experimental methods and atomistic simulations to understand the physical and mechanical behavior of nanostructures, including vibrational behavior, dynamic response, and nanofluid flow. Meanwhile, engineers have created new mathematical techniques to approximate nanostructure behaviors based on classical continuum mechanics. **Figure** 2.5 shows common methods for modeling nanostructure.

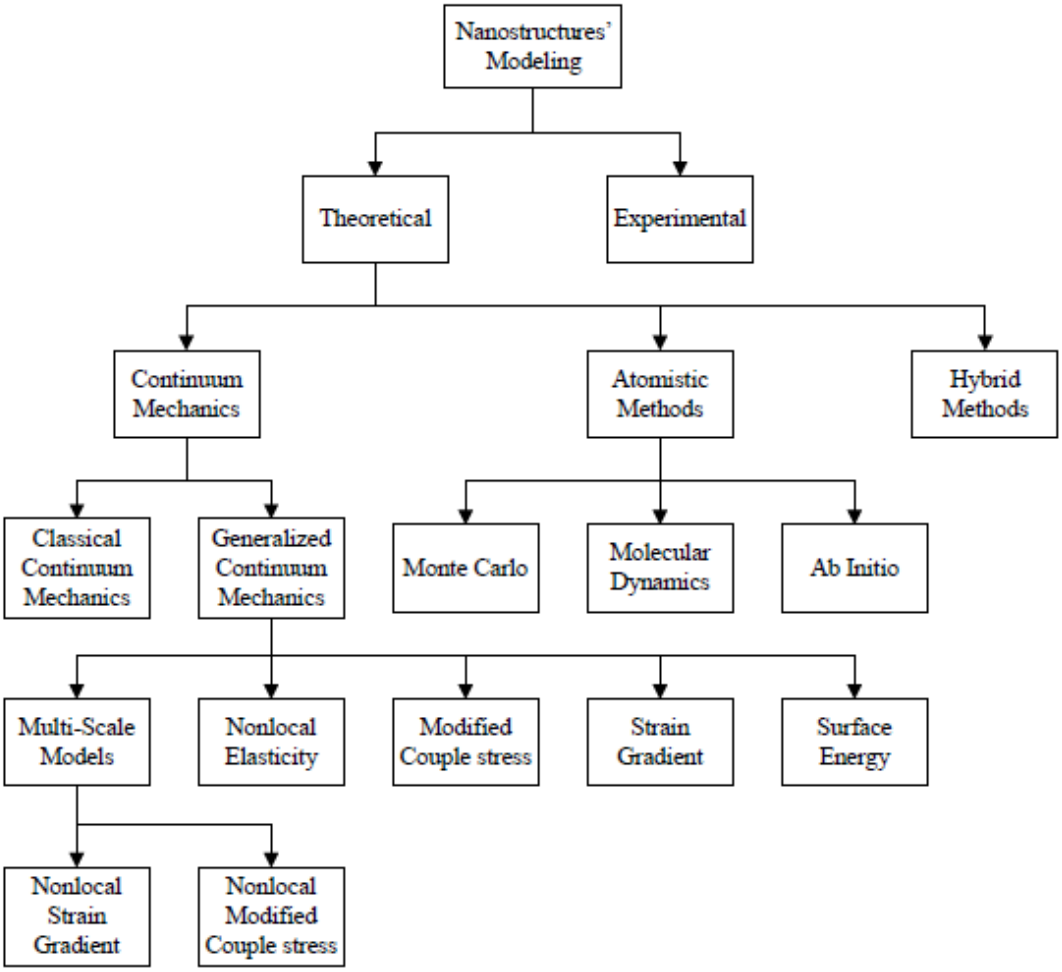

Figure 2.5: Different methods used to model nanostructures[9]

2.2.1 Experimental

The experimental approach includes creating nanostructures using both physical and chemical synthesis methods, followed by employing analytical techniques to examine their properties [91]. Techniques such as scanning electron microscopy, transmission electron microscopy, atomic force microscopy, and various forms of spectroscopy are utilized to manipulate and test the characteristics of nanoscale materials [92]. While this method allows for precise measurement of material properties, it is constrained by the difficulties associated with handling small samples and investigating certain properties at the nanoscale. [93]

2.2.2 Atomestic Approaches

Experimental methods for studying nanostructures are costly. To mitigate this, researchers have developed various theories grounded in atomic simulations.

2.2.2.1 Ab initio

Ab initio calculations, also referred to as the first principles method, are employed to solve the Schrödinger equation. This technique enables the exploration of the structure and properties of various materials at the atomic level. Common methods used in ab initio

calculations include Hartree–Fock and DFT, which help determine energy levels. By using a suitable wave function, these calculations can be applied to study different polymers, large macromolecules, and minerals, including the structure of hydroxyapatite (HAP). As HAP is a primary mineral component of bone, essential for its mechanical strength, it is crucial to calculate its electronic structure and lattice parameters.[94]

2.2.2.2 Molecular dynamics (MD)

Molecular dynamics (MD) is a computational simulation technique used to study the physical behavior of atoms and molecules over time. In this method, atoms and molecules interact within a set timeframe, providing insights into the system's dynamic evolution. Typically, the trajectories of these particles are obtained by numerically solving Newton's equations of motion for a system of interacting particles. The forces and potential energies between the particles are commonly calculated using interatomic potentials or molecular mechanical force fields. This technique is predominantly utilized in chemical physics, materials science, and biophysics.

2.2.2.3 Monte Carlo simulation

Monte Carlo simulation is a statistical technique that creates random and stochastic samples to approximate the probability distribution of different outcomes. This method employs equilibrium statistical mechanics to generate states according to the Boltzmann distribution, rather than relying on molecular dynamics. Instead of modeling the dynamics of a system, it generates states that reflect the system's equilibrium behavior. This approach is frequently utilized to analyze the statistical properties of materials, including their thermodynamic characteristics and phase transitions.

2.2.3 Non-classical continuum mechanics

Due to the high cost, time demands, and specialized expertise required for experimental and atomistic computational methods, researchers may opt for classical continuum mechanics as an alternative methode. We know that nanometric structures consist of atoms bonded together in discrete arrangements. However, non-classical continuum mechanics assumes these structures to be continuous, incorporating discretization through modifications to classical continuum mechanics. This modification accounts for small-scale effects. In the following section, we introduce several methods developed by researchers to account for size effects in nanostructures.

2.2.3.1 Surface elasticity

Due to the high surface-to-bulk ratios of Micro and Nano-scale structures, surface effects significantly impact their mechanical properties and behavior, which classical mechanics models cannot capture. Gurtin and Murdoch [95], [96] developed a surface elasticity theory to address this, treating the surface as a thin membrane with distinct material properties that adhere to the bulk material. This theory introduces non-classical boundary conditions involving surface stresses, which, combined with classical elasticity equations for bulk material, form a coupled system of field equations. This approach provides a continuum

mechanics model for analyzing the mechanical behavior of materials with surface effects and is widely used in studies of thin beams and plates.

2.2.3.2 Modified couple stress theory

The modified couple stress theory (MCST) introduced by Yang et al. builds on the classical couple stress theory by Mindlin et al. Its main advantage is the inclusion of only one additional material length scale parameter. In the MCST, the strain energy density depends on both the strain tensor (associated with the stress tensor) and the curvature tensor (associated with the couple stress tensor).

2.2.3.3 Eringen's nonlocal theories

One of the most effective theories for understanding the mechanical behavior of nanostructures is Eringen's nonlocal theory. According to this theory, the stress at a point in a body is influenced not only by the strain at that specific point but also by the strains at all other points x within the body. Nonlocal elasticity theory successfully explains phenomena at atomic and molecular scales, such as high-frequency vibrations and wave dispersion. Mathematically, the fundamental equations for a homogeneous, nonlocal solid without body forces can be expressed as[97]

$$\sigma_{ij} = \int_{\dot{V}} \alpha(|x' - x|, \mu) C_{ijkl} \varepsilon_{kl}(x') \qquad 2.4$$

The term $\alpha(|x' - x|, \mu)$ represents the nonlocal attenuation function, which is incorporated into the constitutive equations at the reference point x due to the local strain at the source x'.Here, $|x' - x|$ denotes the Euclidean distance, and $\mu = e_0 a/l$ is the scale coefficient that accounts for the small scale factor. In this expression, e_0 is a material constant determined experimentally or approximated by matching the dispersion curves of plane waves with those of atomic lattice dynamics, while l and a represent the internal (e.g., granular size, lattice parameter) and external characteristic lengths (e.g., crack length, wavelength) of the nanostructures, respectively.

On the auter hand, the equation 2.4 can be equivalently expressed in differential form as follows:

$$\sigma_{ij} - (e_0 a)^2 \nabla^2 \sigma_{ij} = C_{ijkl} \varepsilon_{kl} \qquad 2.5$$

Where ∇^2 represents the Laplace operator and $e_0 a$ a denotes the scale coefficient, indicating the size effect on the response of nanoscale structures.

2.2.3.4 Strain gradient theory

One of the theories utilized in modeling micro- and nano-structures is the strain gradient theory. It is important to note that this theory has been more extensively applied to micro-scale structures than to nano-scale structures, with various atomistic simulations supporting this observation. Strain gradient elasticity was originally developed by Mindlin in the 1960s.[98], [99] In this theory, it is posited that in addition to the strain tensor, the gradient of the strain tensor should also be considered when calculating the elastic strain energy function. Thus, the

stress-strain relationship based on this theory can be expressed in a simple differential form as follows

$$\sigma_{ij} = [1 - l^2\,\nabla^2]C_{ijkl}\varepsilon_{kl} \quad 2.6$$

Where l is the material length-scale parameter that indicates the influence of the higher-order strain gradient stress field.

2.2.3.5 Multi-scale method

The non-local parameter in non-local elasticity encompasses information such as lattice spacing. This theory is primarily used to capture the stiffness softening effect, associated with an increase in the non-local parameter. Strain gradient theory, on the other hand, considers the stiffness enhancement effect, where micro/nanoscale materials are presumed to consist of atoms with higher-order deformation mechanisms and cannot be modeled merely as collections of points. The multi-scale method allows for the combination of non-local elasticity with strain gradient theories to account for both stiffness softening and enhancement effects simultaneously. This integration leads to a new theory called the non-local strain gradient theory.[100] This theory provides accurate results compared to molecular dynamics simulations and has gained widespread use over the years due to its effectiveness. Mathematically, the constitutive equation for a continuum solid based on this theory can be expressed as follows

$$[1 - (e_0 a)^2\,\nabla^2]\sigma_{ij} = [1 - l^2\,\nabla^2]C_{ijkl}\varepsilon_{kl} \quad 2.7$$

2.3 Spinning smart shaft based on Multi-scale piezoelectric Euler-Bernouli beams model

2.3.1 Euler-Bernoulli beams theory

Harik's[101], [102] studies examine the applicability and validity of the Euler-Bernoulli beam hypothesis. He demonstrates that the Euler-Bernoulli beam theory can effectively model nanotube structures, such as CNTs. Considering a rotating smart nanoshaft with length L, average radius r, and thickness h, as illustrated in **Figure** 2.6 Based on this theory and his hypotheses, the displacement field of a rotating smart nanoshaft in the rotating frame (x, y, z) is described as follows

$$U_x(x,y,z,t) = -z\frac{\partial w}{\partial x} - y\frac{\partial v}{\partial x} \quad 2.8$$

$$U_y(x,y,z,t) = v(x,t) \quad 2.9$$

$$U_z(x,y,z,t) = w(x,t) \quad 2.10$$

in which U_x; U_y; U_z are the displacement components in the axial, lateral, and transverse directions, and $\frac{\partial w}{\partial x}$; $\frac{\partial v}{\partial x}$ are the rotation of nanoshaft cross-section about z and y axes, respectively. The relationships between normal strain (ε_{xx})and displacement and rotation components for a spinning smart nanoshaft are described as follows

$$\varepsilon_{xx} = -z\frac{\partial^2 w}{\partial x^2} + y\frac{\partial^2 v}{\partial x^2} = \varepsilon_{xx}^w + \varepsilon_{xx}^v \quad 2.11$$

Additionally, the local stress-strain relationship is expressed as

$$\sigma_{xx}^w = E\varepsilon_{xx}^w, \quad \sigma_{xx}^v = E\varepsilon_{xx}^v \quad 2.12$$

Where σ_{xx}^{w} and σ_{xx}^{v} E, and ϑ are the transverse and lateral normal strains, Young's modulus, and poisson ratio , respectively.

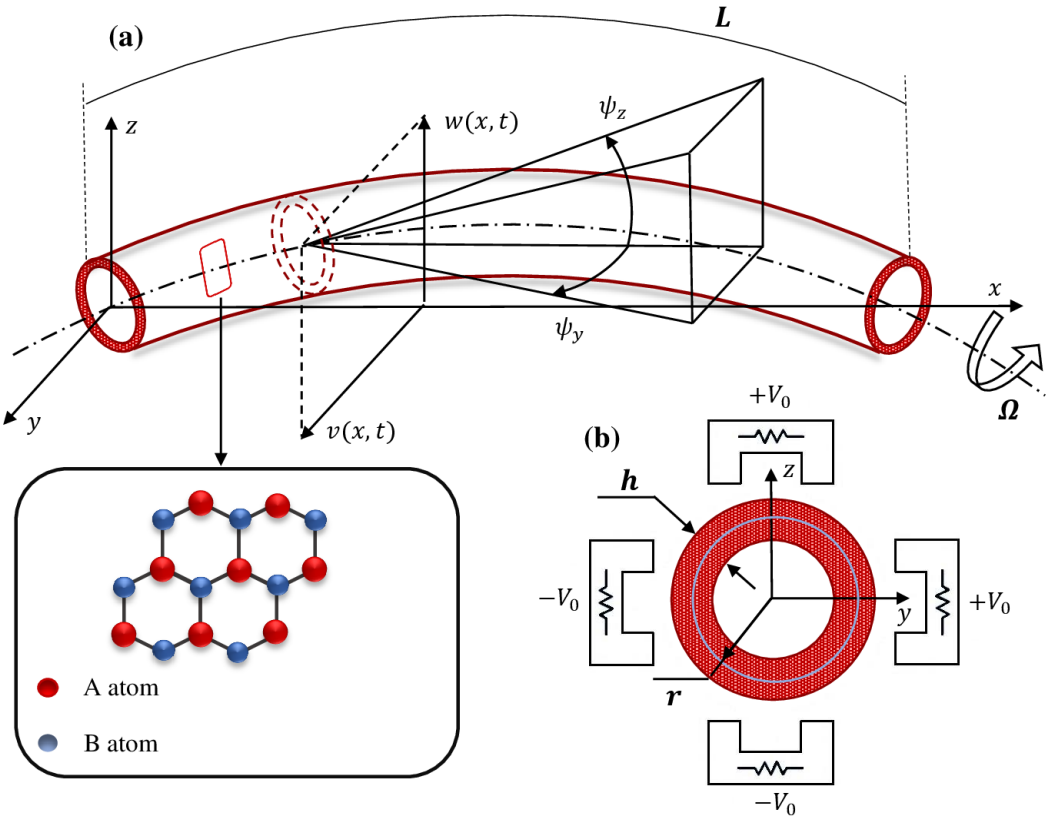

Figure 2.6: Continuum model of rotating smart nanoshaft; (a) the 3D perspective of spinning nanoshaft in the rotating frame; (b) the nanoshaft orthogonal cross-section under lateral and transverse electrical voltages

2.3.2 Small-scale constitutive equations for a spinning smart nanoshaft

The flexural vibration mode splits into two independent orthogonal bending modes as the beam rotates around its central axis. Two orthogonal electric fields must be applied to thoroughly investigate the piezoelectric effect on these modes.[103] This requirement is clearly illustrated in **Figure** 2.6 (b). By doing so, we can comprehensively understand the behavior of each mode under the influence of piezoelectricity, ensuring accurate analysis and results. Based on the nonlocal strain gradient theory and the Euler Bernoulli beam hypotheses, the constitutive equation for a spinning piezoelectric nanoshaft subjected to lateral and transverse polarization is formulated as follows:

$$[1-\eta^2\nabla^2]\begin{Bmatrix}\sigma_{xx}^{v}\\ \sigma_{xx}^{w}\\ D_x^{v}\\ D_x^{w}\\ D_y\\ D_z\end{Bmatrix}=[1-l^2\nabla^2]\begin{bmatrix}E & 0 & 0 & 0 & -e_{21} & 0\\ 0 & E & 0 & 0 & 0 & -e_{31}\\ 0 & 0 & \xi_{11} & 0 & 0 & 0\\ 0 & 0 & 0 & \xi_{11} & 0 & 0\\ e_{21} & 0 & 0 & 0 & \xi_{22} & 0\\ 0 & e_{31} & 0 & 0 & 0 & \xi_{33}\end{bmatrix}\begin{Bmatrix}\varepsilon_{xx}^{v}\\ \varepsilon_{xx}^{w}\\ E_x^{v}\\ E_x^{w}\\ E_y\\ E_z\end{Bmatrix} \quad 2.13$$

In this context, the terms ξ_{11}, ξ_{22}, and ξ_{33} link the electric fields in the longitudinal, lateral, and transverse directions to their respective electric displacements. Consequently, for an isotropic and symmetrical beam, it holds that $e_{21} = e_{31}$ and $\xi_{22} = \xi_{33}$.

Since the nanotube was polarized in the y and z directions, the electrical distribution function must be reformulated to account for this orthogonal polarization. To address this, Behar et al.[103] proposed a new mathematical expression, which is presented as follow

$$\begin{Bmatrix} T(x,z,t) \\ \mathcal{L}(x,y,t) \end{Bmatrix} = \begin{pmatrix} \cos\left(\frac{\pi}{h}z\right) & 0 \\ 0 & \cos\left(\frac{\pi}{h}y\right) \end{pmatrix} \begin{Bmatrix} \phi_{tr} \\ \phi_{la} \end{Bmatrix} + \begin{pmatrix} \frac{2z}{h} \\ \frac{2y}{y} \end{pmatrix} V_0 \tag{2.14}$$

It should be noted that in this study, the external voltage V_0 applied in both directions is identical.

To satisfy Maxwell's electrostatic equations in the proposed method, the electric field is represented as the negative gradient of the electric potential. Thus, in cylindrical coordinates $z = r\sin\theta$ and $y = r\cos\theta$, it can be written as follows

$$\begin{Bmatrix} E_x^w \\ E_x^v \\ E_z \\ E_y \end{Bmatrix} = \begin{Bmatrix} \cos\left(\frac{\pi}{h}r\sin\theta\right)\frac{\partial\phi_{tr}}{\partial x} \\ \cos\left(\frac{\pi}{h}r\cos\theta\right)\frac{\partial\phi_{la}}{\partial x} \\ -\frac{\pi}{h}\sin\left(\frac{\pi}{h}r\sin\theta\right)\phi_{tr} - \frac{2V_0}{h} \\ -\frac{\pi}{h}\sin\left(\frac{\pi}{h}r\cos\theta\right)\phi_{la} - \frac{2V_0}{h} \end{Bmatrix} \tag{2.15}$$

Using equation 2.17 the size-dependent Electro-mechanical coupling forces and moment can be obtained

$$[1-\eta^2\nabla^2]M_z = [1-l^2\nabla^2]EI\frac{\partial^2 w}{\partial x^2} + F_{31}\phi_{tr} \tag{2.16}$$

$$[1-\eta^2\nabla^2]M_y = [1-l^2\nabla^2]EI\frac{\partial^2 v}{\partial x^2} + F_{21}\phi_{la} \tag{2.17}$$

$$\int_2^{2\pi}\int_{r_1}^{r_2}[1-\eta^2\nabla^2]D_x^w\cos\left(\frac{\pi}{h}r\sin\theta\right)rdrd\,\theta = [1-l^2\nabla^2]\left(X_{11}\frac{\partial^2\phi_{tr}}{\partial x^2}\right) \tag{2.18}$$

$$\int_2^{2\pi}\int_{r_1}^{r_2}[1-\eta^2\nabla^2]D_x^v\cos\left(\frac{\pi}{h}r\cos\theta\right)rdrd\,\theta = [1-l^2\nabla^2]\left(X'_{11}\frac{\partial^2\phi_{la}}{\partial x^2}\right) \tag{2.19}$$

$$\int_2^{2\pi}\int_{r_1}^{r_2}[1-\eta^2\nabla^2]D_z\frac{\pi}{h}\sin\left(\frac{\pi}{h}r\sin\theta\right)rdrd\,\theta = [1-l^2\nabla^2]\left[F_{31}\left(\frac{\partial^2 w}{\partial x^2}\right) - X_{33}\phi_{tr}\right] \tag{2.20}$$

$$\int_2^{2\pi}\int_{r_1}^{r_2}[1-\eta^2\nabla^2]D_y\frac{\pi}{h}\sin\left(\frac{\pi}{h}r\cos\theta\right)rdrd\,\theta = [1-l^2\nabla^2]\left[F_{21}\left(\frac{\partial^2 v}{\partial x^2}\right) - X_{22}\phi_{la}\right] \tag{2.21}$$

The supplementary terms outlined in Equations (2.20-2.27) are

$$F_{31} = \int_{2}^{2\pi} \int_{r_1}^{r_2} e_{31} \frac{\pi}{h} \sin\left(\frac{\pi}{h} r \sin\theta\right) r \sin\theta \, r dr d\theta \tag{2.22}$$

$$F_{21} = \int_{2}^{2\pi} \int_{r_1}^{r_2} e_{21} \frac{\pi}{h} \sin\left(\frac{\pi}{h} r \cos\theta\right) r \cos\theta \, r dr d\theta \tag{2.23}$$

$$X_{11} = \int_{2}^{2\pi} \int_{r_1}^{r_2} \xi_{11} \cos^2\left(\frac{\pi}{h} r \sin\theta\right) r dr d\theta \tag{2.24}$$

$$X'_{11} = \int_{2}^{2\pi} \int_{r_1}^{r_2} \xi_{11} \cos^2\left(\frac{\pi}{h} r \cos\theta\right) r dr d\theta \tag{2.25}$$

$$X_{33} = \int_{2}^{2\pi} \int_{r_1}^{r_2} \xi_{33} \left[\frac{\pi}{h} sin\left(\frac{\pi}{h} r sin\theta\right)\right]^2 r dr d\theta \tag{2.26}$$

$$X_{22} = \int_{2}^{2\pi} \int_{r_1}^{r_2} \xi_{22} \left[\frac{\pi}{h} sin\left(\frac{\pi}{h} r cos\theta\right)\right]^2 r dr d\theta \tag{2.27}$$

In which I and A are the diametral moment of inertia and cross-section area, respectively.

2.4 Summary

In this chapter, we presented an overview of the essential concepts and approaches for modeling spinning smart nanoshafts. Firstly, we discussed the notion of nanoscale piezoelectricity, along with the constitutive equation for piezoelectric materials at the macroscale, and the function of electrical potential distribution. Following this, we presented an overview of various modeling techniques employed to describe the behavior of nanostructures. These techniques encompass experimental, atomistic, and continuum mechanics approaches. Among these methods, we introduced the NSGT, which accounts for both nonlocal and strain gradient effects. Additionally, we explored the application of Timoshenko beam theory and NSGT to derive the electro-mechanical coupling forces and moments.

Chapter 3 Equations of Motions and vibrational response

Objective:

This chapter is divided into two main sections. In the first section, we derive the size-dependent equation of motion and its associated boundary conditions using the Hamiltonian principle. This rigorous approach ensures that the dynamic behavior of the nanoshaft is accurately captured, taking into account its scale-dependent properties. In the second section, we apply a semi-analytical approach based on the Galerkin technique to obtain the vibrational response of the system. This method provides a detailed analysis of the system's vibrational characteristics, enabling us to understand the complex interactions and responses of the spinning smart nanoshaft.

3.1 Motion Equations and boundary conditions.

3.2 Solving the equations

3.3 Vibration response of spinning smart nanotube

3.1 Motion Equations and boundary conditions

The equations of motion and the corresponding boundary conditions for a uniform rotating smart nanoshaft, modeled using the Timoshenko hypotheses, can be derived through the application of Hamilton's principle as

$$\int_{t_1}^{t_2} (\delta T - \delta V + \delta W) dt \tag{3.1}$$

Here, T represents the kinetic energy, V denotes the potential energy, and δW is the virtual work done by an external forses. We assume that the spinning smart nanoshaft has a uniform hollow circular cross-section and rotates about its central axis at a constant speed of Ω (rad/s) to accommodate small amplitude vibrations.

3.1.1 Potential energy

The variation of strain energy of spinning smart nanoshaft is written as[103]

$$\delta V = \int_0^L \int_0^{2\pi} \int_{r_1}^{r_2} \left(\sigma_{xx}^w \delta\varepsilon_{xx}^w + \sigma_{xx}^v \delta\varepsilon_{xx}^v - D_x^w \delta E_x^w - D_x^v \delta E_x^v - D_z \delta E_z - D_y \delta E_y\right) r dr d\theta dx \tag{3.2}$$

$$= \int_0^L \left\{ -M_z \delta \frac{\partial^2 w}{\partial x^2} - M_y \delta \frac{\partial^2 w}{\partial x^2} \right.$$
$$+ + \int_0^{2\pi} \int_{r_1}^{r_2} \left(-D_x^w cos\left(\frac{\pi}{h} r sin\theta\right) \frac{\partial \delta\phi_{tr}}{\partial x} - -D_x^v cos\left(\frac{\pi}{h} r cos\theta\right) \frac{\partial \delta\phi_{la}}{\partial x} \right.$$
$$\left. \left. + D_z \left(\frac{\pi}{h} sin\left(\frac{\pi}{h} r sin\theta\right)\right) \delta\phi_{tr} + D_y \left(\frac{\pi}{h} sin\left(\frac{\pi}{h} r cos\theta\right)\right) \delta\phi_{la} \right) r dr d\theta \right\} dx \tag{3.3}$$

Where M_z and M_y represent the bending moments around the z and y axes, respectively. Also, Q_{xz} and Q_{xy} denote the transverse shear forces in oxz and oxy, respectively. The expression of these moments and forces are

$$\begin{Bmatrix} M_z \\ M_y \end{Bmatrix} = \int_0^{2\pi} \int_{r_1}^{r_2} \begin{Bmatrix} \sigma_{xx}^w r sin\theta r dr d\theta \\ \sigma_{xx}^w r cos\theta r dr d\theta \end{Bmatrix} \tag{3.4}$$

3.1.2 kinetic energy

Figure 3.1 illustrates the displacement of an arbitrary point P on the cross-section of the rotating smart nanoshaft. This new position of P results from both lateral and transverse deformations. The fixed coordinates are denoted by x, y, z, while the mobile coordinates attached to the rotating smart nanoshaft and its cross-section are denoted by x_1, y_1, z_1. Before the deformation, the center Gc of the cross-section coincides with the center O

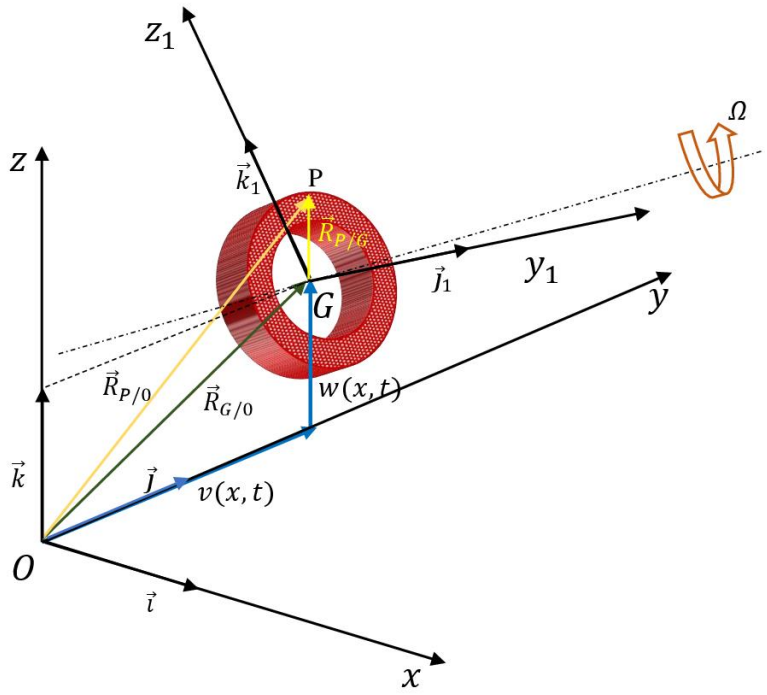

Figure 3.1: Displacement of an arbitrary point P of the cross-section of the rotating smart nanoshaft.

The position vector is[104] $\vec{R}_{P/O} = \vec{R}_{G/O} + \vec{R}_{P/G} = \left(v(x,t)\vec{j} + w(x,t)\vec{k}\right) + \left(y_1\vec{j}_1 + z_1\vec{k}_1\right)$

we can write the vector position in terms of the Euler angle (see **Figure** 3.2) that characterizes the rotation of cross-section of the smart nanoshat. by adopting the Euler angle with the rotation of the cross-section as $\Phi_z = \frac{\partial w}{\partial x}$, $\Phi_y = \frac{\partial v}{\partial x}$, $\Phi_x = \Omega t$, the vector position is expressed as[104]

$$\begin{aligned}\vec{R}_{P/O} = {} & \left(-y_1\psi_y cos\Omega t + y_1\psi_z sin\Omega t - z_1\psi_y sin\Omega t + z_1\psi_z cos\Omega t\right)\vec{\imath} \\ & + \left(v(x,t) - y_1 cos\Omega t + y_1\psi_y\psi_z sin\Omega t - z_1 sin\Omega t + z_1\psi_y\psi_z cos\Omega t\right)\vec{j} \\ & + \left(w(x,t) + y_1 sin\Omega t + z_1 cos\Omega t\right)\vec{k}\end{aligned} \qquad 3.5$$

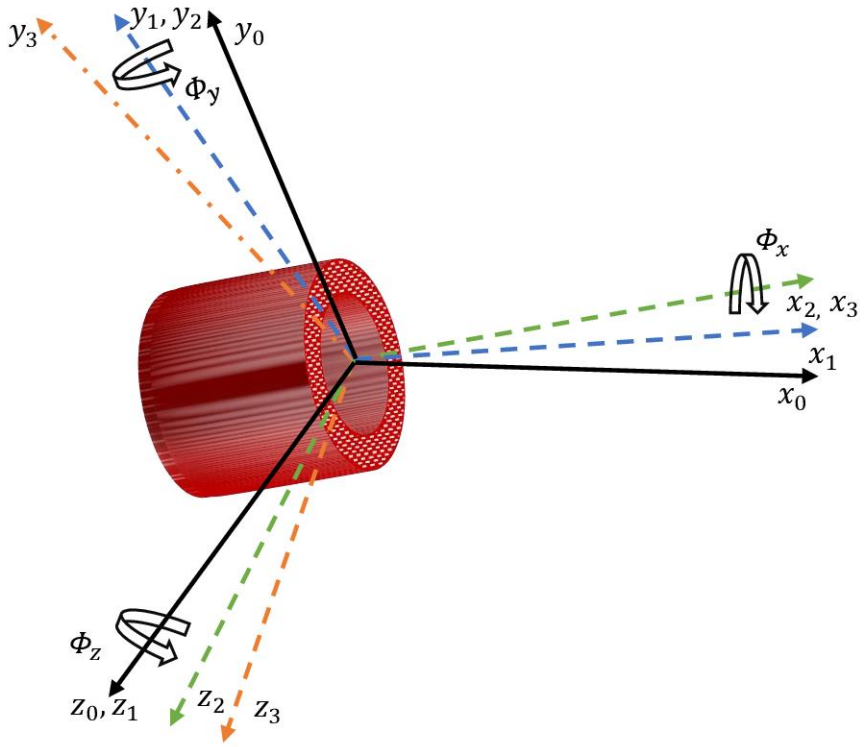

Figure 3.2: Euler angle

Also, The velocity vector is written as

$$\frac{\partial \vec{R}_{P/O}}{\partial t} = \dot{\vec{R}}_{P/O} \tag{3.6}$$

However, the following equation gives the expression for the kinetic energy of the smart nano shaft:

$$V = \frac{1}{2}\int_0^L \int_0^{2\pi} \int_{r_1}^{r_2} \rho \left(\dot{\vec{R}}_{P/O}.\dot{\vec{R}}_{P/O}\right) r dr d\theta dx \tag{3.7}$$

Though, The kinetic energy in the expanded form is

$$V = \frac{1}{2}\int_0^L \left[\rho A\left\{\left(\frac{\partial v(x,t)}{\partial t}\right)^2 + \left(\frac{\partial w(x,t)}{\partial t}\right)^2\right\} + \rho I\left\{\left(\frac{\partial^2 w}{\partial x \partial t}\right)^2 + \left(\frac{\partial^2 w}{\partial x \partial t}\right)^2\right\} - 2\rho\Omega I \frac{\partial w}{\partial x}\frac{\partial^2 v}{\partial x \partial t} + 2I\rho\Omega^2 + \Omega^2 I\left\{\left(\frac{\partial w(x,t)}{\partial x}\right)^2 + \left(\frac{\partial v(x,t)}{\partial x}\right)^2\right\}\right] dx \tag{3.8}$$

Finally, the variation of kinetic energy is expressed as

$$\delta V = \int_0^L \left[\rho A\left\{\left(\frac{\partial v(x,t)}{\partial t}\frac{\partial \delta v(x,t)}{\partial t} + \frac{\partial w(x,t)}{\partial t}\frac{\partial \delta w(x,t)}{\partial t}\right) + \rho I\left\{\frac{\partial^2 \psi_y}{\partial t \partial x}\frac{\partial^2 \delta \psi_y}{\partial t \partial x} + \frac{\partial^2 \psi_z}{\partial t \partial x}\frac{\partial^2 \delta \psi_z}{\partial t \partial x}\right\} + \Omega\rho I \frac{\partial w}{\partial x}\frac{\partial^2 \delta v}{\partial x \partial t} + \Omega\rho I \frac{\partial^2 v}{\partial x \partial t}\frac{\partial \delta w}{\partial x} + \overbrace{\Omega^2 I\rho\left(\frac{\partial w}{\partial x}\frac{\partial \delta v}{\partial x} + \frac{\partial v}{\partial x}\frac{\partial \delta w}{\partial x}\right)}^{Neglected}\right\}\right] dx \tag{3.9}$$

Where ρ is the density of the smart nanoshaft, $\rho I\left\{\frac{\partial^2\psi_y}{\partial t\partial x}\frac{\partial^2\delta\psi_y}{\partial t\partial x}+\frac{\partial^2\psi_z}{\partial t\partial x}\frac{\partial^2\delta\psi_z}{\partial t\partial x}\right\}$ represents the rotational inertia effect, $+\Omega\rho I\frac{\partial w}{\partial x}\frac{\partial^2\delta v}{\partial x\partial t}+\Omega\rho I\frac{\partial^2 v}{\partial x\partial t}\frac{\partial\delta w}{\partial x}$ represents the gyroscopic effect. Moreover, the therm $\Omega^2 I\rho\left(\psi_y\delta\psi_y+\psi_z\delta\psi_z\right)$ represents centrifugal hardening. The effect of centrifugal hardening becomes significant at high rotational speeds, while at low rotational speeds, its impact is negligible.

3.1.3 Work of external forces

As previously mentioned, the nanotube is polarized in both lateral and transverse directions. However, when an external voltage is applied along this axis, it induces two distinct axial forces. Furthermore, we consider the rotating smart nanoshaft within a thermal environment, where temperature variations may influence its behavior. Additionally, the rotation of the smart nanoshaft at high speeds generates a hoop tension due to thr centrifugal force, further affecting its structural dynamics.

So, the variation of the initial external electric voltage's work is represented as

$$\delta V=\frac{1}{2}\int_0^L\left(N_T+N_{C_f}\right)\left[N_{E_1}\left(\frac{\partial w(x,t)}{\partial x}\frac{\partial\delta w(x,t)}{\partial x}\right)+N_{E_2}\frac{\partial v(x,t)}{\partial x}\frac{\partial\delta v(x,t)}{\partial x}\right]dx \tag{3.10}$$

Where, N_T, N_{C_f}, N_{E_1}, and N_{E_2} are the axial thermal, hoop tension, and external voltage forces.

In which the axial electrical forces are as[103]

$$\begin{Bmatrix}N_{E_1}\\N_{E_2}\end{Bmatrix}=-A\frac{2V_0}{h}\begin{Bmatrix}e_{31}\\e_{21}\end{Bmatrix} \tag{3.11}$$

Also, the axial force induced by thermal expansion, can be expressed as[105]

$$N_T=-\alpha EA\Delta T \tag{3.12}$$

where α is the thermal expansion coefficient, and ΔT is the temperature change.

To accurately calculate the axial hoop force resulting from centrifugal effects, the corresponding axial stress must first be evaluated. This stress, originally derived by Behzad and Bastami,[106] was based on the plane strain assumption

$$\sigma_{xx}(r)=\frac{\upsilon}{4(1-\upsilon)}[(3-2\upsilon)(r_1^2-r_2^2)-2r^2]\rho\Omega^2 \tag{3.13}$$

By integrating this stress over the cross-section, the net axial hoop force N_{C_f} can be obtained[107]

$$N_{C_f}=\int_{r_1}^{r_2}2\pi r\sigma_{xx}dr=\upsilon\rho 2I\Omega^2 \tag{3.14}$$

The axial hoop force is proportional to the square of the smart nanoshaft rotational speed, rendering its impact more pronounced at higher speeds

3.1.4 The final form of the gouverning equations

The final form of the governing equations is derived by substituting Equations (3.3), (3.9), and (3.10) into Equation (3.1) performing some manipulations

$$\delta w: \quad \frac{\partial^2 M_z}{\partial x^2} - N_1 \frac{\partial^2 w}{\partial x^2} = \rho A \frac{\partial^2 w}{\partial t^2} - \Omega I_p \frac{\partial^3 v}{\partial x^2 \partial t} \tag{3.15}$$

$$\delta v: \quad \frac{\partial^2 M_y}{\partial x^2} - N_2 \frac{\partial^2 v}{\partial x^2} = \rho A \frac{\partial^2 v}{\partial t^2} + \Omega I_p \frac{\partial^3 w}{\partial x^2 \partial t} \tag{3.16}$$

$$\int_0^{2\pi} \int_{r_1}^{r_2} \left[D_x^w cos\left(\frac{\pi}{h} r sin\theta\right) + D_z \frac{\pi}{h} sin\left(\frac{\pi}{h} r sin\theta\right) \right] r dr dx = 0 \tag{3.17}$$

$$\int_0^{2\pi} \int_{r_1}^{r_2} \left[D_x^v cos\left(\frac{\pi}{h} r cos\theta\right) + D_y \frac{\pi}{h} sin\left(\frac{\pi}{h} r scos\theta\right) \right] r dr dx = 0 \tag{3.18}$$

The required geometrical and natural boundary conditions at the end of the smart nanoshaft $(x = 0, L)$ are

$$\begin{aligned}
&w = 0 \quad \text{or} \quad \frac{\partial M_z}{\partial x} = 0 && x = 0, L \\
&v = 0 \quad \text{or} \quad \frac{\partial M_y}{\partial x} = 0 && x = 0, L \\
&\frac{\partial w}{\partial x} = 0 \quad \text{or} \quad M_z = 0 && x = 0, L \\
&\frac{\partial v}{\partial x} = 0 \quad \text{or} \quad M_y = 0 && x = 0, L \\
&\phi_{tr} = 0 \text{ or} \\
&\int_0^{2\pi} \int_{r_1}^{r_2} \left[D_x^w cos\left(\frac{\pi}{h} r sin\theta\right) \right] r dr dx = 0 && x = 0, L \\
&\phi_{la} = 0 \text{ or} && x = 0, L \\
&\int_0^{2\pi} \int_{r_1}^{r_2} \left[D_x^v cos\left(\frac{\pi}{h} r cos\theta\right) \right] r dr dx = 0
\end{aligned} \tag{3.19}$$

The small-scale piezoelectric bending moments and shear forces of a spinning smart nanotube are derived by substituting Equations (3.15) and (3.16) into Equations (2.16-) and (2.17)

$$[1 + \eta^2 \nabla^2] M_y = [1 + l^2 \nabla^2] \left(-EI \frac{\partial^2 w}{\partial x^2} + E_{31}\, \phi_z \right) \tag{3.20}$$

$$[1 + \eta^2 \nabla^2] M_z = [1 + l^2 \nabla^2] \left(-EI \frac{\partial^2 v}{\partial x^2} + E_{21}\, \phi_y \right) \tag{3.21}$$

Unlike M_z and M_y, in Equations. (3.15-3.16), the electric displacements D_x^w, D_x^v, D_z, and D_y cannot be directly derived by substituting Equations. (3.17-3.18) into Eqs. (2.18-2.21) because there are two unknowns but only one equilibrium equation, Equatio,s. (3.16-3.17). However, Eq. (3.17-3.18) can be reformulated in terms of w, v, ϕ_{tr}, and ϕ_{la} using Eqs. (2.18-

2.21). Subsequently, using Equations. (3.18-3.21) along with Equations. (2.16-2.21), the governing equations (3.15-3.18) for the spinning smart nanoshaft can be formulated as follows

$$[1+l^2\nabla^2]\left[E_{31}\frac{\partial^2\,\phi_z}{\partial x^2}-EI\frac{\partial^4 w}{\partial x^2}\right]+[1+\eta^2\nabla^2]\left(N_{E_1}+N_T+N_C\right)\frac{\partial^2 w}{\partial x^2}$$
$$=[1+\eta^2\nabla^2]\left[\rho A\frac{\partial^2 w}{\partial t^2}-2\rho\Omega I\frac{\partial^3 v}{\partial x^2\partial t}\right] \quad 3.22$$

$$[1+l^2\nabla^2]\left[E_{21}\frac{\partial^2\,\phi_y}{\partial x^2}-EI\frac{\partial^4 v}{\partial x^2}\right]+[1+\eta^2\nabla^2]\left(N_{E_1}+N_T+N_C\right)\frac{\partial^2 v}{\partial x^2}$$
$$=[1+\eta^2\nabla^2]\left[\rho A\frac{\partial^2 v}{\partial t^2}+2\rho\Omega I\frac{\partial^3 w}{\partial x^2\partial t}\right] \quad 3.23$$

$$[1+l^2\nabla^2]\left[\xi_{11}\frac{\partial^2\,\phi_y}{\partial x^2}-E_{21}\frac{\partial^2\,v}{\partial x^2}-\xi_{22}\phi_y\right]=0 \quad 3.24$$

$$[1+l^2\nabla^2]\left[X_{11}\frac{\partial^2\,\phi_z}{\partial x^2}-E_{31}\frac{\partial^2\,w}{\partial x^2}-X_{33}\phi_z\right]=0 \quad 3.25$$

3.2 Solving the equations

3.2.1 Computational Galerkin Mthode

The Galerkin technique used here is a semi-analytical method, where the axial function that satisfies the geometric boundary conditions is chosen analytically. Specifically, the axial function $Y(x)$

is selected as the beam function as follows[108]

$$Y(x)=A_1\cosh\left(\frac{\lambda_n x}{L}\right)+A_2 cos\left(\frac{\lambda_n x}{L}\right)-\varkappa_n\left[A_3 sinh\left(\frac{\lambda_n x}{L}\right)+A_4 sin\left(\frac{\lambda_n x}{L}\right)\right] \quad 3.26$$

Here, $A_i(1{,}4)$ are constants with values of 0 or 1, selected based on the boundary conditions. Additionally, λ_n is a real value proportional to the number of axial modes, and it must be calculated for each specific set of boundary conditions.

The geometric boundary conditions at the ends of the smart nanoshaft $(x=0,L)$ for Simply Supported-Simply Supported (S-S), Clamped-Clamped (C-C), Clamped-Simply Supported (C-S), and Clamped-Free (C-F) configurations can be mathematically expressed in terms of $Y(x)$ as follows

For S-S boundary condition

$$Y(x)|_0^L=Y''(x)|_0^L=0 \quad 3.27$$

$$\begin{pmatrix} 1 & 1 & 0 & 0 \\ \left(\frac{\lambda_n}{L^2}\right)^2 & -\left(\frac{\lambda_n}{L^2}\right)^2 & 0 & 0 \\ cosh(\lambda_n) & cos(\lambda_n) & sinh(\lambda_n) & sin(\lambda_n) \\ \frac{\lambda_n{}^2 cosh(\lambda_n)}{L^2} & -\frac{\lambda_n{}^2 cos(\lambda_n)}{L^2} & -\frac{\lambda_n{}^2 cosh(\lambda_n)}{L^2} & \frac{\lambda_n{}^2 sin(\lambda_n)}{L^2} \end{pmatrix} \begin{Bmatrix} A_1 \\ A_2 \\ A_3 \\ A_4 \end{Bmatrix} = \begin{pmatrix} 0 \\ 0 \\ 0 \\ 0 \end{pmatrix} \quad 3.28$$

The determinant of Equation (1), which defines the characteristic equation for the wave number value of the S-S boundary condition, is given by

$$\cosh(\lambda_n)\sin(\lambda_n) = 0 \quad 3.29$$

The roots of this equation provide the value of λ_n for each vibration mode number, and are given by

$$\lambda_n = m\pi \quad \text{Where} \quad for = 1,2,3, \ldots \ldots \quad 3.30$$

However, Equation 4 also provides the value of $A_i(1,4)$, given by

$$A_1 = A_2 = A_3 = 0, \quad A_4 = -1 \quad 3.31$$

For C-C boundary condition

$$Y(x)|_0^L = Y'(x)|_0^L = 0 \quad 3.32$$

$$\begin{pmatrix} 1 & 1 & 0 & 0 \\ 0 & 0 & -\left(\frac{\lambda_n}{L}\right) & -\left(\frac{\lambda_n}{L}\right) \\ cosh(\lambda_n) & cos(\lambda_n) & sinh(\lambda_n) & sin(\lambda_n) \\ \frac{\lambda_n sinh(\lambda_n)}{L} & -\frac{\lambda_n sin(\lambda_n)}{L} & -\frac{\lambda_n cosh(\lambda_n)}{L} & \frac{\lambda_n sin(\lambda_n)}{L} \end{pmatrix} \begin{Bmatrix} A_1 \\ A_2 \\ A_3 \\ A_4 \end{Bmatrix} = \begin{pmatrix} 0 \\ 0 \\ 0 \\ 0 \end{pmatrix} \quad 3.33$$

Also, the determinant of Equation (1), defining the characteristic equation for the wave number under the C-C boundary condition, is expressed as

$$\cos(\lambda_n)\cosh(\lambda_n) - 1 = 0 \quad 3.34$$

The roots of this equation yield the value of λ_n for each vibration mode number, and are expressed as

$$\lambda_n = \frac{(2m+1)\pi}{2} \quad \text{for } m \geq 3 \quad 3.35$$

Nevertheless, the value of $A_i(1,4)$ for C-C boundary condition, are given by

$$A_1 = A_3 = 1, \quad A_2 = A_4 = -1 \quad 3.36$$

To avoid redundancy and keep the reader engaged, we can use the same methodology applied to S-S and C-S conditions to present the characteristic equations and the values of λ_n and $A_i(1,4)$ constants in Table 3.1

Table 3.1: Values of $A_i(1,4)$, and λ_n for C-S and C-F different boundary conditions[108]

BCs	$A_i(1,4)$	Characteristic equations	Values of λ_n
C-S	$A_1 = A_3 = 1,$ $A_2 = A_4 = -1$	$\tan(\lambda_n) - \tan(\lambda_n) = 0$	$\lambda_n = \frac{(4m+1)\pi}{4}\ for \quad m \geq 2$
C-F	$A_1 = A_3 = 1,$ $A_2 = A_4 = -1$	$\cos(\lambda_n)\cosh(\lambda_n) + 1 = 0$	$\lambda_n = \frac{(2m-1)\pi}{2}\ for \quad m \geq 2$

Also, the value of $\varkappa_n$ for each boundary condition is presented as

For S-S boundary condition

$$\varkappa_n = 1 \tag{3.37}$$

For C-S and C-C boundary condition

$$\varkappa_n = \frac{\cosh(\lambda_n) - \cos(\lambda_n)}{\sinh(\lambda_n) - \sin(\lambda_n)} \tag{3.38}$$

For C-F boundary condition

$$\varkappa_n = \frac{\sinh(\lambda_n) - \sin(\lambda_n)}{\cosh(\lambda_n) + \cos(\lambda_n)} \tag{3.39}$$

It is worth noting that the value of λ_n obtained by solving the characteristic equations for C-C, C-S, and C-F conditions is approximate, as these characteristic equations cannot be solved analytically. Therefore, this method is considered a semi-analytical approach.

3.3 Vibration response of spinning smart nanotube

The displacement and electric potential components of the spinning smart nanoshat are assumed to be the sum of spatial variations and time-harmonic exponential functions based on the Fourier series, and are expressed as follows

$$w(x,t) = w_n Y(x) e^{i\omega t} \tag{3.40}$$
$$v(x,t) = v_n Y(x) e^{i\omega t} \tag{3.41}$$
$$\phi_{tr}(x,t) = \phi_{tr_n} Y(x) e^{i\omega t} \tag{3.42}$$
$$\phi_{la}(x,t) = \phi_{la_n} Y(x) e^{i\omega t} \tag{3.43}$$

Here, w_n, v_n, ϕ_{tr_n}, and ϕ_{la_n} are constants representing the amplitudes of the vibrations, while $Y(x)$ is the axial function that satisfies the geometric boundary conditions. Additionally, n and ω denote the longitudinal mode numbers and the natural frequency of the vibration, respectively.

By substituting equations (3.39-3.44) into equations (3.23-3.28) and integrating the spatial variations and their derivatives from 0 to L, we obtain the following simple algebraic equations.

$$\left\{\begin{pmatrix} M_{11} & 0 & 0 & 0 \\ 0 & M_{22} & 0 & 0 \\ 0 & 0 & 0 & 0 \\ 0 & 0 & 0 & 0 \end{pmatrix}\omega^2 + \begin{pmatrix} 0 & G_{12} & 0 & 0 \\ -G_{21} & 0 & 0 & 0 \\ 0 & 0 & 0 & 0 \\ 0 & 0 & 0 & 0 \end{pmatrix} i\omega + \begin{pmatrix} K_{11} & 0 & K_{13} & 0 \\ 0 & K_{22} & 0 & K_{24} \\ K_{31} & 0 & K_{33} & 0 \\ 0 & K_{42} & 0 & K_{44} \end{pmatrix}\right\} \begin{pmatrix} v_n \\ w_n \\ \phi_{y_n} \\ \phi_{z_n} \end{pmatrix} = \begin{pmatrix} 0 \\ 0 \\ 0 \\ 0 \end{pmatrix} \tag{3.44}$$

Therefore, the compact form of Eq. (26) can be expresed as:

$$\{[M]\omega^2 + [G]i\omega + [K]\}(X) = 0$$

$$[A(\boldsymbol{\omega})](X) = 0 \tag{3.45}$$

The matrices M, G, and K represent the mass, gyroscopic, and stiffness properties of the spinning smart nanoshaft, respectively. The elements of the matrix above are given as follows

$$M_{11} = M_{22} = -\rho A\eta^2 \int_{\mathbf{0}}^{\boldsymbol{L}} \frac{\partial^2 Y(x)}{\partial x^2}\, Y(x)dx + \rho A \int_{0}^{L} Y(x)Y(x)dx \tag{3.46}$$

$$G_{12} = -G_{21} = a_{12} = -2\rho\Omega I\eta^2 \int_{\mathbf{0}}^{\boldsymbol{L}} \frac{\partial^4 Y(x)}{\partial x^4}\, Y(x)dx + 2\rho\Omega I \int_{\mathbf{0}}^{\boldsymbol{L}} \frac{\partial^2 Y(x)}{\partial x^2}\, Y(x)dx \tag{3.47}$$

$$K_{11} = K_{22} = -EI \int_{\mathbf{0}}^{\boldsymbol{L}} \frac{\partial^4 Y(x)}{\partial x^4}\, Y(x)dx + EIl^2 \int_{\mathbf{0}}^{\boldsymbol{L}} \frac{\partial^6 Y(x)}{\partial x^6}\, Y(x)dx \tag{3.48}$$

$$K_{13} = E_{21} \int_{\mathbf{0}}^{\boldsymbol{L}} \frac{\partial^2 Y(x)}{\partial x^2}\, Y(x)dx - l^2 E_{21} \int_{\mathbf{0}}^{\boldsymbol{L}} \frac{\partial^4 Y(x)}{\partial x^4}\, Y(x)dx \tag{3.49}$$

$$q_{23} = q_{14} \tag{3.50}$$

$$q_{26} = q_{15} \tag{3.51}$$

$$K_{24} = E_{31} \int_{\mathbf{0}}^{\boldsymbol{L}} \frac{\partial^2 Y(x)}{\partial x^2}\, Y(x)dx - l^2 E_{31} \int_{\mathbf{0}}^{\boldsymbol{L}} \frac{\partial^4 Y(x)}{\partial x^4}\, Y(x)dx \tag{3.52}$$

$$K_{31} = -K_{13} \tag{3.53}$$

$$K_{33} = \left(\xi_{11} \int_{\mathbf{0}}^{\boldsymbol{L}} \frac{\partial^2 Y(x)}{\partial x^2}\, Y(x)dx - \xi_{22} \int_{0}^{L} Y(x)Y(x)dx \right) [1 + l^2\nabla^2] \tag{3.54}$$

$$K_{44} = \left(X_{11} \int_{\mathbf{0}}^{\boldsymbol{L}} \frac{\partial^2 Y(x)}{\partial x^2}\, Y(x)dx - X_{33} \int_{0}^{L} Y(x)Y(x)dx \right) [1 + l^2\nabla^2] \tag{3.55}$$

To solve Equation (40), it is essential to first transform it into the standard eigenvalue problem form

$$\left(\begin{bmatrix} 0 & I \\ -K & -G \end{bmatrix} \omega^2 + \begin{pmatrix} I & 0 \\ 0 & M \end{pmatrix} \omega \right) \begin{Bmatrix} [X] \\ \omega[X] \end{Bmatrix} = \begin{Bmatrix} 0 \\ 0 \end{Bmatrix} \tag{3.56}$$

In Equation (41),$[0]$, and $[I]$ denote order four's zero and identity matrices, respectively. The standard eigenvalue problem, which describes the nanotube's vibration frequency, is solved using MATLAB software. The equation's solutions yield two frequency values, corresponding to the direction of rotation: the positive value indicates forward whirl, while the negative value indicates backward whirl

3.3.1 implementation of calculation code

The MATLAB software package is used to solve the standard eigenvalue problem that characterizes the vibration frequency of spinning smart nanoshaft. To create the code, you must first input the Electro-mechanical properties of the system. Next, define the axial beams function and the wave number for the boundary conditions. Then, create the mass, gyroscopic, and stiffness of the systeme. By using the $[V, D] = eig(A)$ Matlab fuction The eigenvalue and eigenvectors of the system can be determined.

The output result will match the stationary vibration frequency when the rotational speed is zero. As the rotational speed changes, the system yields two frequency values, one smaller and one larger, depending on the rotation direction. Note that the output result provides the frequency in radians per second (rad/s). It is necessary to convert this result to Hertz (Hz) and then to Gigahertz (GHz). The calculation scheme of the Galerkin computational method using the Matlab software package is presented in the appendix.

3.4 Summary

In this chapter, we present the methodology for obtaining the governing equation of motion using the Hamiltonian principle based on the variational energy method. First, we derive the strain and kinetic energy along with the work of the applied external voltage of a rotating smart (piezoelectric) nanoshaft. Following this, we use the Hamiltonian principle to obtain the equations of motion and their associated boundary conditions. Next, we introduce the Galerkin-based closed-form solution method used to determine the vibrational response. Finally, we employ this method to discretize our governing equations and obtain the vibrational response. We also explain our developed MATLAB code utilizing the Galerkin computational method.

Chapter 4

Electro-mechanical vibration analysis of rotating smart nanoshaft using piezoelectric nonlocal strain gradient theory

Objective:

This chapter is divided into two main sections. In the first section, we conduct a comprehensive comparative study of our results with those existing in the literature to validate the accuracy and reliability of our methodology. In the second section, we perform an extensive parametric analysis to understand the effects of rotating speed, applied external voltage, small-scale parameters, and various boundary conditions on the behavior of the spinning smart nanoshaft. This analysis provides valuable insights into the dynamic characteristics and performance of the nanoshaft under different operational scenarios.

4.1 Comparative study.

4.2 Parametric study.

4.1 Comparative study

Due to the lack of similar publications addressing the full scope of the problem, directly validating the results presented in this study poses a significant challenge. Nevertheless, this section undertakes a comprehensive validation through four examinations of the current study's findings. Firstly, we calculate the first natural frequency of a stationary piezoelectric nanotube under specific boundary conditions—simply supported (S-S) and clamped-simply supported (C-S)—without considering the effects of spin and strain gradient parameters. This verification spans a range of nonlocal parameters, comparing our results with those of Ke et al.[109], who employed the Kirchhoff-Love shell model in conjunction with the Navier solution procedure and the differential quadrature (DQ) method. The comparative data is presented in **Table** 4.1, where the dimensionless nonlocal parameter $\tau = \eta/L$ and and the axial mode number n are highlighted. Secondly, **Table** 4.2 presents a comparison of the fundamental dimensionless frequencies of a steady-state piezoelectric nanobeam with parameters $\left(E = 132GPa,\ e_{31} = -4.1\frac{C}{m^2},\ \zeta_{11} = 5.841 \times 10^{-9}(\mathrm{F/m}),\ \zeta_{33} = 7.124 \times 10^{-9}(\mathrm{F/m}),\ \rho = 7500\,\mathrm{Kg/m^3},\ \eta = 0.1L\right)$ across various standard ratios. These findings are compared with those of Zeng et al. ,[110] who employed the Differential Quadrature Method (DQM) based on the Euler–Bernoulli beam model. In this context, the dimensionless frequency is represented as $\zeta = \omega L\sqrt{\rho/E}$. In the third verification, by excluding piezoelectric and spin effects, the first natural frequency (THz) of a simply-supported carbon nanotube (CNT) as a function of the length-to-diameter ratio is determined using the nonlocal strain gradient Euler-Bernoulli beam model. **Table** 4.3 presents these findings, which are compared with results obtained by Mehralian et al.[111] and Ghorbani et al.[112] using first-order shear deformation shell theory and molecular dynamics (MD) simulations. Furthermore, **Table** 4.4 examines the variation of forward and backward whirl frequencies of a spinning single-walled carbon nanotube (SWCNT) for various spinning speeds and nonlocal parameters, employing Timoshenko beam theory under clamped-clamped (C-C) and clamped-free (C-F) boundary conditions. This comparison excludes piezoelectric effects and strain gradient parameters, and the results are compared with those from Ikhani et al.[113]Finally, A spinning macro-shaft's forward and backward whirls, subjected to four hard boundary conditions (S–S, C–C, C–S, C–F), are analyzed and validated. The results are compared with those obtained by Choi et al.[114] And Aounat et al.,[115] who employed the (DQM) based on the Timoshenko beam theory and the state-space analytical method based on the Euler-Bernoulli beam hypotheses.

Table 4.1: Comparison of the first natural frequency ω (GHz) of a stationary piezoelectric nanotube with S-S, and C-S boundary conditions for various nonlocal parameters using Love's shell theory ($E = 85.66\text{GPa},\ e_{31} = -13.05\text{C/m}^2,\ \zeta_{11} = 5.841 \times 10^{-9}(\text{F/m}),\ \zeta_{33} = 5.395 \times 10^{-9}(\text{F/m}),\ \rho = 7500\ \text{Kg/m}^3,\ h = 1\text{nm},\ r/h = 50$).

BCs	L/d	$\eta = 0$			$\eta = 0.02L$			$\eta = 0.03L$		
		Ref.[109]	Present	Err %	Ref.[109]	Present	Err %	Ref.[109]	Present	Err %
S-S	30	0.07876	0.08349	5.66	0.06745	0.07075	4.66	0.05839	0.06753	13.5
	40	0.04453	0.04696	5.17	0.03432	0.03976	13.6	0.02850	0.03417	16.5
	50	0.02866	0.03005	4.62	0.01692	0.02545	33.5	0.01585	0.02187	27.5
C-S	30	0.1202	0.13038	7.80	0.1029	0.10787	4.60	0.08607	0.09132	5.74
	40	0.06873	0.07333	6.27	0.05358	0.06068	11.7	0.04391	0.05139	14.5
	50	0.04436	0.04693	5.47	0.03134	0.03883	19.2	0.02456	0.03289	25.3

Table 4.2: Comparisons of the first dimensionless natural frequency $\zeta = \omega L\sqrt{\rho/E}$ of the steady-state piezoelectric nanobeam. $\eta = 0.1L$

L/h	S-S		C-S		C-C		C-F	
	Ref.[110]	Present	Ref.[110]	Present	Ref.[110]	Present	Ref.[110]	Present
6	0.4570	0.4569	0.707 7	0.7058	1.024 5	1.0184	0.171 4	0.1700
8	0.3428	0.3427	0.531 0	0.5294	0.768 4	0.7638	0.128 5	0.1275
10	0.2742	0.2741	0.425 0	0.4235	0.616 7	0.6110	0.102 8	0.1020
16	0.1714	0.1714	0.265 8	0.2647	0.384 2	0.3819	0.064 3	0.0637
20	0.1371	0.1371	0.212 7	0.2118	0.307 3	0.3055	0.051 4	0.0510
30	0.0914	0.0914	0.142 0	0.1412	0.204 9	0.2037	0.034 3	0.0340

Table 4.3: Comparison of the first natural frequency (TPa) of armchair (5,5) CNT obtained from MD simulation and NSGT theory ($E = 1.06\ \text{TPa},\ \upsilon = 0.19,\ h = 0.34\ \text{nm},\ d = 0.678\ \text{nm},\ \rho = 2300\ \text{kg/m}^3$)

L/r	Mehralian et la. (MD)[111]	Ghorbani et al. (MD)[112]	Mehralian et al. (Navier's & NSGT)[111]	Present (Galerkin & NSGT)	Err %	Err %	Err %
14.94	0.466	0.462	0.448	0.423	9.22	8.44	5.58
27.78	0.190	0.191	0.192	0.190	0	0.52	1.05
34.94	0.122	0.124	0.126	0.129	5.42	1.58	2.32

Table 4.4: Comparison of the first, second forward, and backward whirls of rotating carbon nanotubes for various nonlocal parameters and boundary conditions ($E = 1\text{TPa},\ \rho = 2750\ Kgm^{-3},\ r_1 = 1nm,\ h = 0.34nm,\ L = 40nm$)

	$\Omega\left(\frac{\text{rad}}{\text{s}}\right) \times 10^{12}$		0	1	20	0	1	20
C-C	η (nm^2)	Ref	Whirl type	First frequency (THz)			Second frequency (THz)		
	0	Ref.[113]	ω_f	0.034257	0.035009	0.050198	0.090530	0.093022	0.139257
			ωb	0.034257	0.033515	0.021923	0.090530	0.088067	0.051195
			ωf	0.034451	0.035221	0.051532	0.091974	0.094547	0.144411
			ω_b	0.034451	0.033693	0.022111	0.091974	0.089440	0.052241
	2	Ref.[113]	ω_f	0.034000	0.034779	0.050595	0.088079	0.090683	0.138917

			ω_b	0.034000	0.033231	0.021365	0.088079	0.085509	0.047986
			ω_f	0.034186	0.034984	0.051896	0.089404	0.092089	0.143737
			ω_b	0.034186	0.033402	0.021547	0.089404	0.086765	0.048886
C-F	0	Ref.[113]	ω_f	0.005576	0.005636	0.007698	0.034941	0.035871	0.055766
			ω_b	0.005576	0.005517	0.004690	0.034941	0.034023	0.018101
		Present	ω_f	0.005575	0.005635	0.006895	0.034940	0.035877	0.058012
			ω_b	0.005575	0.005516	0.004508	0.034940	0.034028	0.021044
	2	Ref.[113]	ω_f	0.005578	0.005638	0.007645	0.034654	0.035571	0.055195
			ω_b	0.005578	0.005520	0.004705	0.034654	0.033748	0.018102
		Present	ω_f	0.005578	0.005637	0.006873	0.034653	0.035617	0.058538
			ω_b	0.005578	0.005520	0.004527	0.034653	0.033716	0.020514

Table 4.5: Comparison of the first four forward, and backward whirls of rotating steady-state shaft (rad^{-1}) ($r_1 = 0.025m,\ \rho = 7800\text{Kg}.m^{-3},\ L = 1.3m,\ \Omega = 500rad^{-1}$)

BCs	n	Choi et al.(TBT & DQM)[114]		Aouinat et al.(EBBT & Stat space)[115]		Present (TBT & Galerkin)	
		ω_f	ω_b	ω_f	ω_b	ω_f	ω_b
S-S	1	735.818	732.258	741.127	737.477	737.477	735.602
	2	2882.80	2869.54	2964.50	2949.90	2964.50	2949.90
	3	6280.74	6254.04	6670.14	6637.29	6670.14	6637.29
	4	10717.9	10676.6	11858.0	11799.6	11858.0	11799.6
C-S	1	1631.02	1626.94	1678.18	1673.63	1638.53	1634.37
	2	4343.24	4329.44	4628.23	4611.20	4400.23	4386.07
	3	8163.07	8136.95	9074.78	9038.21	8305.06	8278.44
	4	12,847.4	12,809.1	13384.1	13323.1	13384.1	13323.2
C-C	1	1137.83	1133.80	1157.05	1152.80	1157.05	1152.80
	2	3587.19	3573.51	3750.64	3734.78	3750.64	3734.78
	3	7206.41	7179.96	7826.26	7791.48	7826.26	7791.48
	4	11781.4	11741.4	15002.5	14939.2	15002.6	14939.2
C-F	1	263.334	261.635	264.503	262.782	263.530	263.213
	2	1618.49	1607.18	1662.43	1650.37	1652.92	1648.01
	3	4395.50	4370.97	4663.03	4634.13	4629.96	4612.99
	4	8272.69	8232.56	9157.59	9103.94	9074.61	9038.03

The outcomes of the verification review demonstrate a high degree of consistency with the referenced literature, underscoring the robustness of the current mathematical formulation. This strong alignment suggests that the formulation is highly effective in accurately modeling and capturing the complex electro-mechanical vibrations of spinning smart nanoshafts, thereby affirming its reliability for further analytical and practical applications.

4.2 Parametric study

Our study highlights a significant gap in the literature, as most smart single-walled nanotubes (SWNTs) have not been thoroughly examined regarding their electro-mechanical properties, such as Young's modulus, dielectric constants, and piezoelectric coefficients. Notably, the electro-mechanical properties of SWZnONTs and SWBNNTs have been identified only with considerable difficulty. Despite these challenges, we have selected (6,6) armchair

SWNTs as the models for both nanotubes. The electro-mechanical properties of SWZnONTs, sourced from [31, 32, 36, 73], are presented in Table 4.6

In the mathematical modeling of the vibrational characteristics of single-walled nanotubes, thickness emerges as a critical parameter. Our review of the literature reveals that no experimental or theoretical studies have conclusively established the optimal thickness for SWZnONTs. Consequently, we propose two estimates. First, we assume that the nanotube's thickness is equivalent to that of a graphene-like ZnO nanosheet, measured at 0.26 nm [74]. Alternatively, we estimate the thickness of SWZnONTs to be 0.08 nm, approximately 44% of the average theoretical diameters of oxygen (0.1286 nm) and zinc (0.2386 nm) atoms. This latter estimate is derived using the method employed by Panchal et al. [75] to determine the thickness of SWBNNTs, given the structural similarities between SWZnONTs and SWBNNTs. Additionally, the thermo-electro-mechanical properties of SWBNNTs are referenced from[38], [116], [117], [118], [119] and are presented in **Table** 4.6 Additionally, with the effective thickness of BNNTs adopted from Yan et al.[119]

Table 4.6: The physical properties of SWBNNT and SWZnONT

	SWBNNT (6,6)	SWZnONT (6,6)
Young's modulus E (TPa)	3.5001	0.177
Piezoelectric constant e_{31}/e_{21} C/m^2	-0.43	-0.33
Orthogonal component of dielectric tensor ξ_{11} F/m	$3.29e^{-8}$	$3.29e^{-8}$
Parallel components of dielectric tensor ξ_{22}/ξ_{33} F/m	$6.82e^{-8}$	$6.82e^{-8}$
Density ρ $(\frac{Kg}{m^3})$	2280	5610
Poisson's ratio ν	0.1937	/
Coefficient of thermal expansion (room temperature)K^{-1}[117]	$-0.3e^{-8}$	/
Coefficient of thermal expansion (High temperature)K^{-1}[117]	$0.2e^{-6}$	/

Before conducting our parametric study, it is crucial to compare the natural frequencies of the two nanotubes with identical geometrical properties. This comparison will help us determine their vibrational responses and identify the nanotubes with higher frequencies, which will be the focus of the remainder of the study. **Table** 4.7 presents a comparison of the variation in forward and backward whirls between a (SWBNNT) and a (SWZnONT) across various mode numbers. From this data, it is evident that the natural frequencies of the SWBNNT are higher than those of the SWZnONT. This difference can be attributed to the fact that the SWBNNT has a higher Young's modulus and exhibits superior piezoelectric properties. Therefore, understanding the vibrational response of SWBNNTs is particularly crucial for their potential application as spinning components in nanodevice rotors.

Table 4.7: The comparison of the whirling frequency between SWBNNT and SWZnONT

BCs	Material type	Whirls type	Ω	0			1			2		
			n	1	2	3	1	2	3	1	2	3
S-S	SWZnONT	f_w		12.901	47.919	97.649	12.951	48.056	97.789	13.004	48.194	97.929
		b_w		12.901	47.919	97.649	12.852	47.781	97.509	12.800	47.645	97.370
	SWBNNT	f_w		112.68	402.08	789.01	112.73	402.17	789.01	112.77	402.15	789.02
		b_w		112.68	402.08	789.01	112.64	401.99	789.00	112.59	401.91	789.00
C-S	SWZnONT	f_w		20.064	60.180	113.56	20.111	60.303	113.64	20.174	60.426	113.73
		b_w		20.06	60.180	113.56	20.010	60.057	113.47	19.955	59.935	113.39
	SWBNNT	f_w		174.76	503.18	915.10	174.80	503.24	915.17	174.85	503.30	915.24
		b_w		174.76	503.18	915.10	174.72	503.12	915.02	174.67	503.07	914.95
C-C	SWZnONT	f_w		29.052	73.763	130.61	29.102	73.859	130.63	29.102	73.956	130.63
		b_w		29.052	73.763	130.61	29.003	73.666	130.60	29.003	73.570	130.60
	SWBNNT	f_w		252.78	614.81	1050.0	252.75	614.85	1050.2	252.78	614.87	1050.3
		b_w		252.78	614.81	1050.0	252.68	614.82	1048.8	252.65	614.81	1049.7
C-F	SWZnONT	f_w		4.7390	28.536	73.815	4.7445	28.591	73.911	4.7501	28.646	74.007
		b_w		4.7390	28.536	73.815	4.7445	28.481	73.719	4.7279	28.426	73.623
	SWBNNT	f_w		42.244	247.82	615.36	42.251	24.786	615.37	615.39	247.90	615.39
		b_w		42.244	247.82	615.36	42.239	247.78	615.34	615.33	247.74	615.33

4.2.1 Effect of spinning speed and mode number

In a rotating structure, the interplay between rotational speed and natural frequency gives rise to a fascinating phenomenon known as frequency bifurcation. As the rotational speed increases, the system's natural frequency is split into two distinct whirl modes: forward (f_w) and backward (b_w). The forward whirl occurs when the whirl motion and rotational speed align in the same direction, creating a synchronous effect. Conversely, the backward whirl represents the inverse scenario, where the whirl motion opposes the direction of rotation.

This bifurcation has significant implications for the dynamic behavior of rotating systems. To elucidate this complex relationship, **Figure** 4.1 presents a comprehensive benchmark investigation. This analysis meticulously explores the impact of rotating speed—and by extension, the gyroscopic effect—on the dimensionless forward and backward whirls. The study encompasses various boundary conditions and examines multiple mode numbers, providing a holistic view of the system's response across different configurations. The impact of rotational speed on the system's behavior varies significantly across different boundary conditions and mode numbers. In the simply supported-simply supported (S-S) configuration, the influence of rotational speed diminishes as the mode number increases, becoming negligible at higher modes.

For the clamped-simply supported (C-S) boundary condition, the second mode exhibits a slightly reduced sensitivity to spinning speed compared to the S-S case. Interestingly, at higher mode numbers, the C-S configuration shows a marginally increased susceptibility to rotational effects relative to its S-S counterpart.

The clamped-clamped (C-C) boundary condition presents a distinct behavior pattern. Here, the impact of rotational speed becomes more pronounced at higher mode numbers, while the second mode demonstrates a reduced sensitivity to spinning speed.

In the case of the clamped-free (C-F) boundary condition, the second mode number exhibits the most significant response to rotational speed. However, this effect diminishes considerably at higher mode numbers.

Notably, the data reveals that the first mode number remains consistently unaffected by changes in spinning speed across all boundary conditions. This observation underscores the fundamental nature of the first mode in rotating systems.

Furthermore, the analysis clearly demonstrates that the boundary conditions at the ends of the spinning smart nanotube play a crucial role in modulating the effects of rotational speed, particularly for the second and higher mode numbers.

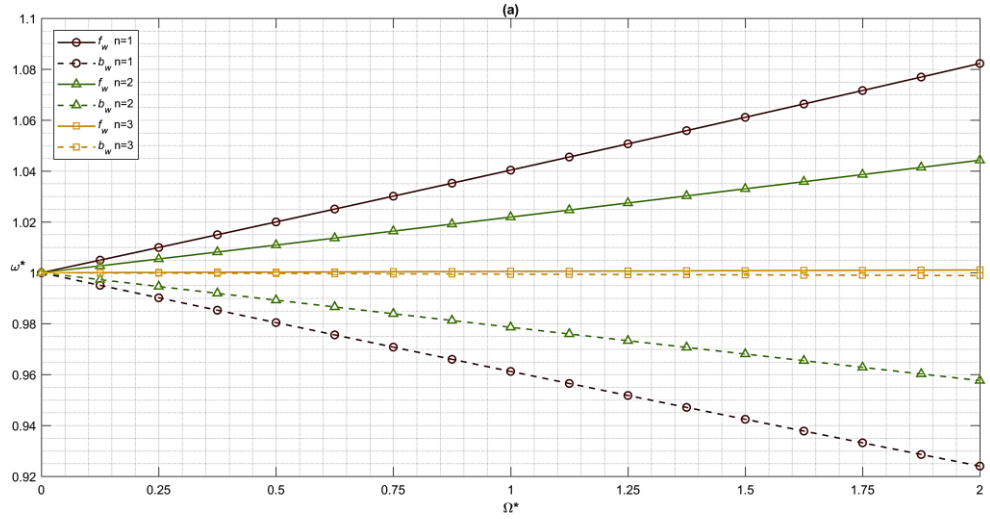

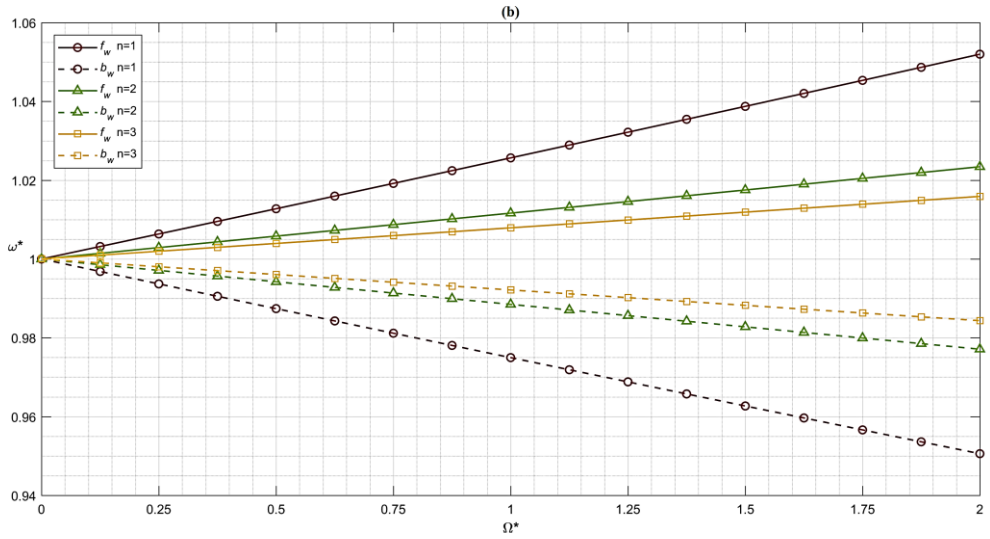

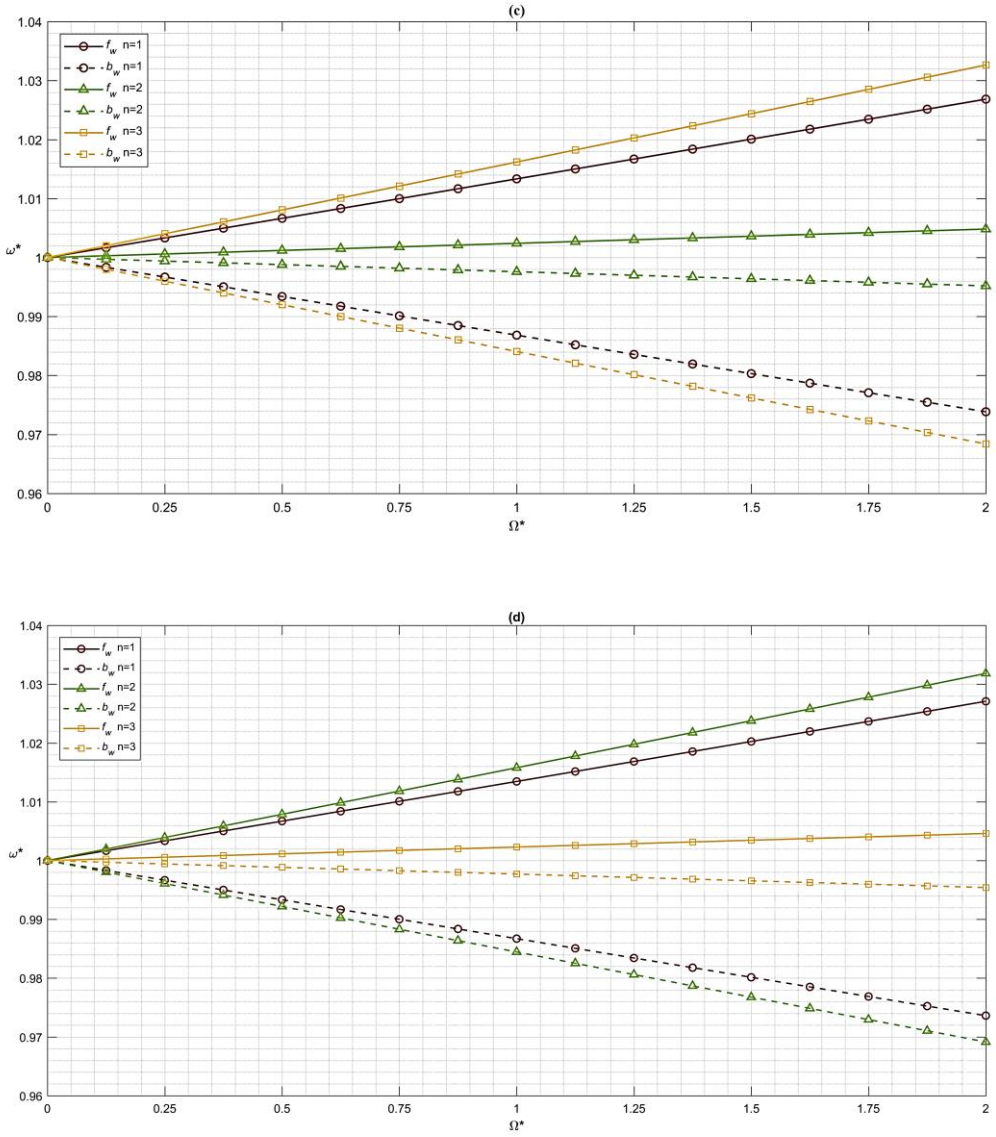

Figure 4.1: Variations of the dimensionless forward and backward whirls of spinning smart nanoshaft for different mode numbers: (a) S-S, (b) C-S, (c) C-C, (b) C-F ($\frac{L}{D} = 15, \eta = 1.3nm, l = 0.4nm, V_0 = 0\ volt, \Delta \mathrm{T} = 0$)

4.2.2 The effect of rotating speed and small scale parameters

In this section the effect of rotating speed and small scale parameters on forward and backward whirl are investigated. **Figure** 4.2(a) illustrates the effect of spinning speed and the nonlocal parameter on whirling frequency under simply-supported (S-S) boundary conditions. An increase in the local parameters reduces the forward whirl and increases the backward whirl. Furthermore, increasing the nonlocal parameters in the S-S boundary condition diminishes the influence of rotating speed. **Figure** 4.2(b) demonstrates that in clamped-simply-supported (C-S) boundary conditions, increasing the nonlocal parameter from 0 to 2 nm reduces the forward whirl and increases the backward whirl. However, at higher nonlocal parameters, the behavior reverses. According to **Figure** 4.2(c, which examines clamped-clamped (C-C) boundary conditions, an increase in the nonlocal parameter similarly decreases the forward whirl and

increases the backward whirl, though this behavior also reverses at higher nonlocal parameters. Unlike in the S-S boundary condition, in the clamped-free (C-F) boundary condition, an increase in the nonlocal parameter increases the forward whirl and decreases the backward whirl (see figure (1(d)). Thus, it can be concluded that in the C-F boundary condition, an increase in the nonlocal parameter amplifies the effect of rotating speed.

In **Figure** 4.3, the coupling effect of rotating speed and the strain gradient parameter is presented. **Figure** 4.3(a-c) shows that increasing the strain gradient parameter in the S-S, C-S, and C-C boundary conditions reduces the forward whirl and increases the backward whirl. However, in the C-F boundary condition, the strain gradient term loses its influence at lower rotating speeds. On the other hand, at higher mode numbers, the forward whirl begins to increase while the backward whirl decreases (see **Figure** 4.3(d)). In conclusion, the nonlocal term has a smaller impact on the natural frequencies in the C-F boundary condition compared to other boundary conditions.

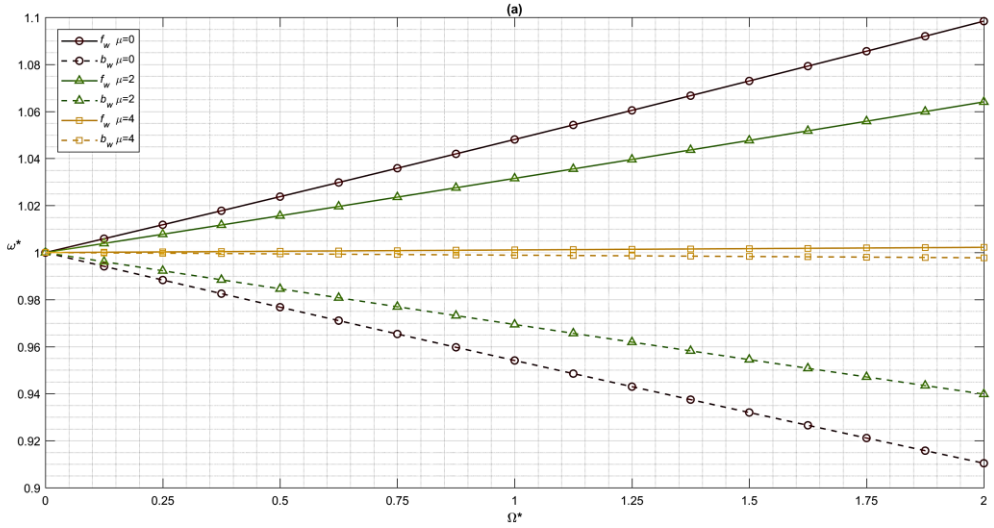

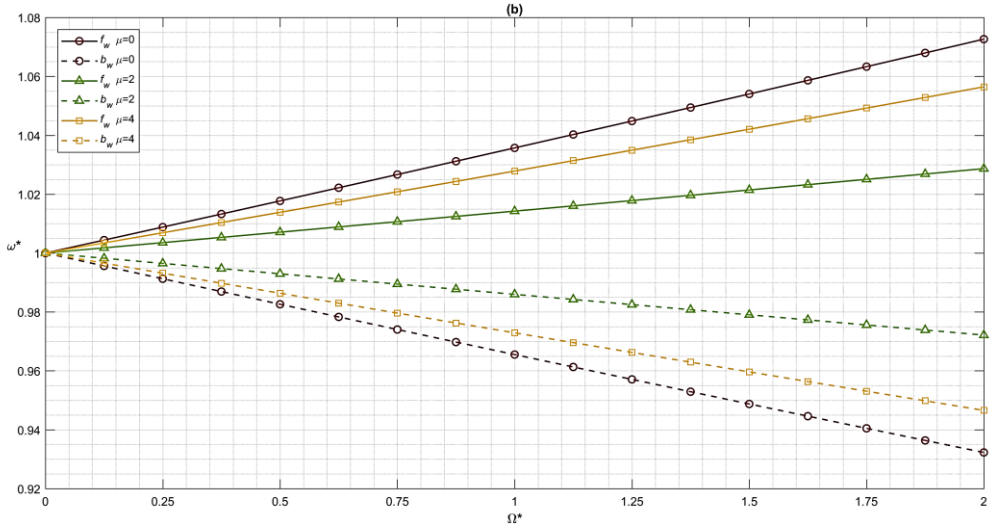

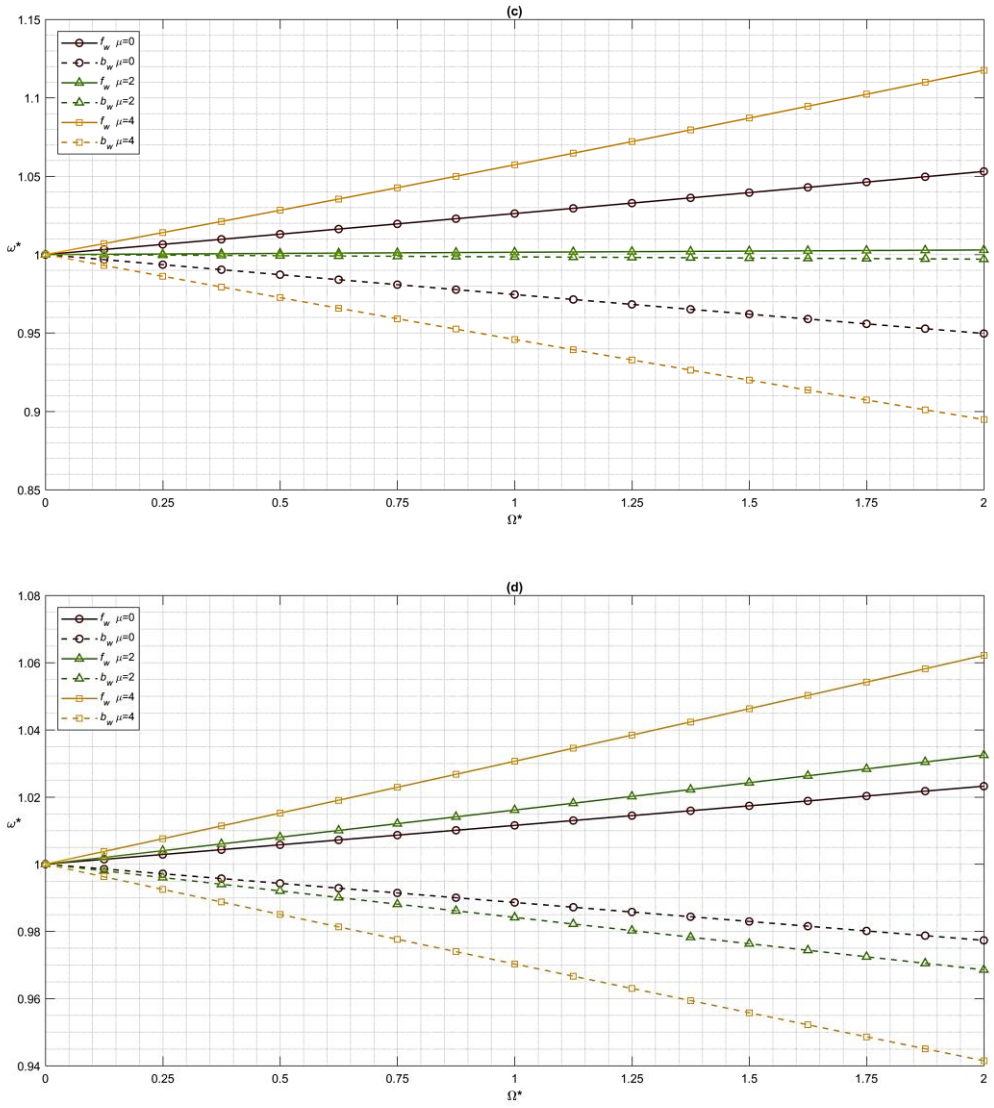

Figure 4.2 : Variations of first dimensionless forward and backward whirls of spinning smart nanoshaft for different nonlocal parameters: (a) S-S, (b) C-S, (c) C-C, (b) C-F ($\frac{L}{D} = 15, n = 1, V_0 = 0\ volt, \Delta \mathrm{T} = 0$)

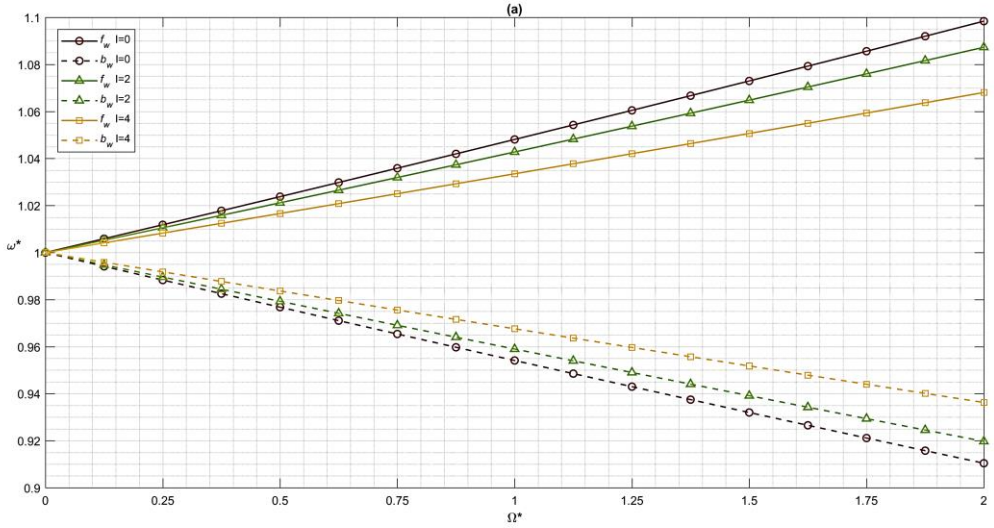
(a)
f_w l=0
b_w l=0
f_w l=2
b_w l=2
f_w l=4
b_w l=4
ω*
Ω*

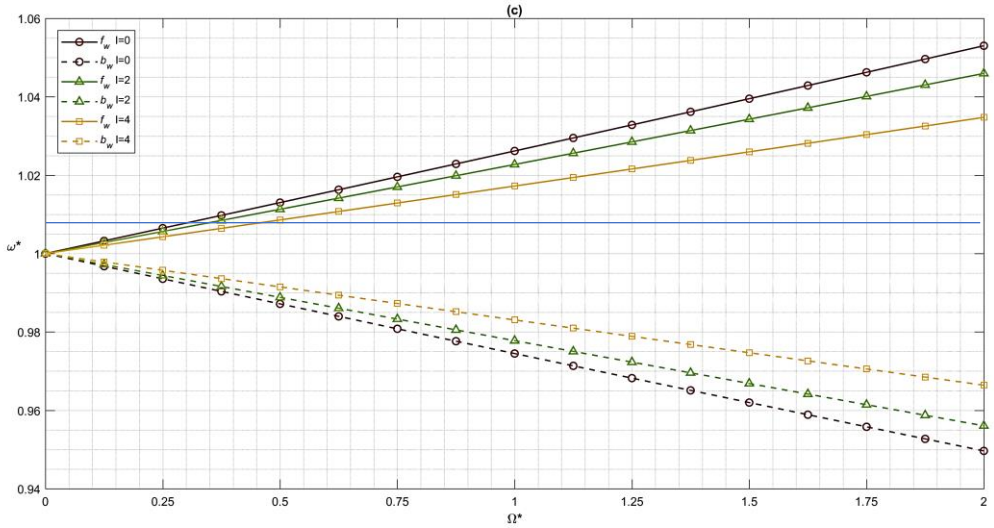
(c)
f_w l=0
b_w l=0
f_w l=2
b_w l=2
f_w l=4
b_w l=4
ω*
Ω*

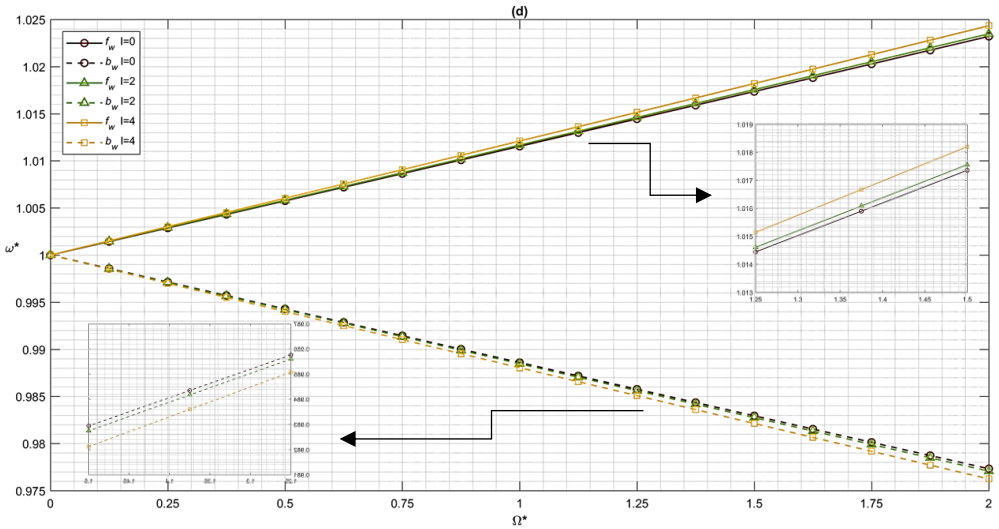
(d)
f_w l=0
b_w l=0
f_w l=2
b_w l=2
f_w l=4
b_w l=4
ω*
Ω*

Figure 4.3: Variations of first dimensionless forward and backward whirls of spinning smart nanoshaft for different material length scale parameters: (a) S-S, (b) C-S, (c) C-C, (b) C-F ($\frac{L}{D} = 15, n = 1, V_0 = 0\ volt, \Delta \mathrm{T} = 0$)

4.2.3 The effect of external electric voltage

Figure 4: illustrates the influence of external electric voltage (V_0) on the forward and backward whirls (measured in GHz) across various boundary conditions. The analysis reveals intriguing behavior patterns across different structural configurations.

For simply supported-simply supported (S-S), clamped-simply supported (C-S), and clamped-clamped (C-C) boundary conditions (as shown in Figures 4.3 a-c), a clear trend emerges: positive voltages lead to a decrease in whirling frequencies. In contrast, negative voltages increase. This phenomenon can be attributed to the voltage-induced axial forces within the nanobeams. Specifically, positive voltages generate compressive forces, whereas negative voltages produce tensile forces, altering the system's dynamic response.

Interestingly, the clamped-free (C-F) boundary condition exhibits a contrasting behavior, as depicted in Figure 4.3 (d). In this configuration, the relationship between applied voltage and whirling frequencies is inverted compared to the other boundary conditions. This one-of-a-kind response emphasizes the importance of end constraints for electromechanical coupling in smart nanoshafts.

These results illustrate the intricate relationship between external electric fields, structural boundary conditions, and the dynamic behavior of nanoscale rotating systems. Such insights are critical for the development and optimization of complex nanoelectromechanical systems.

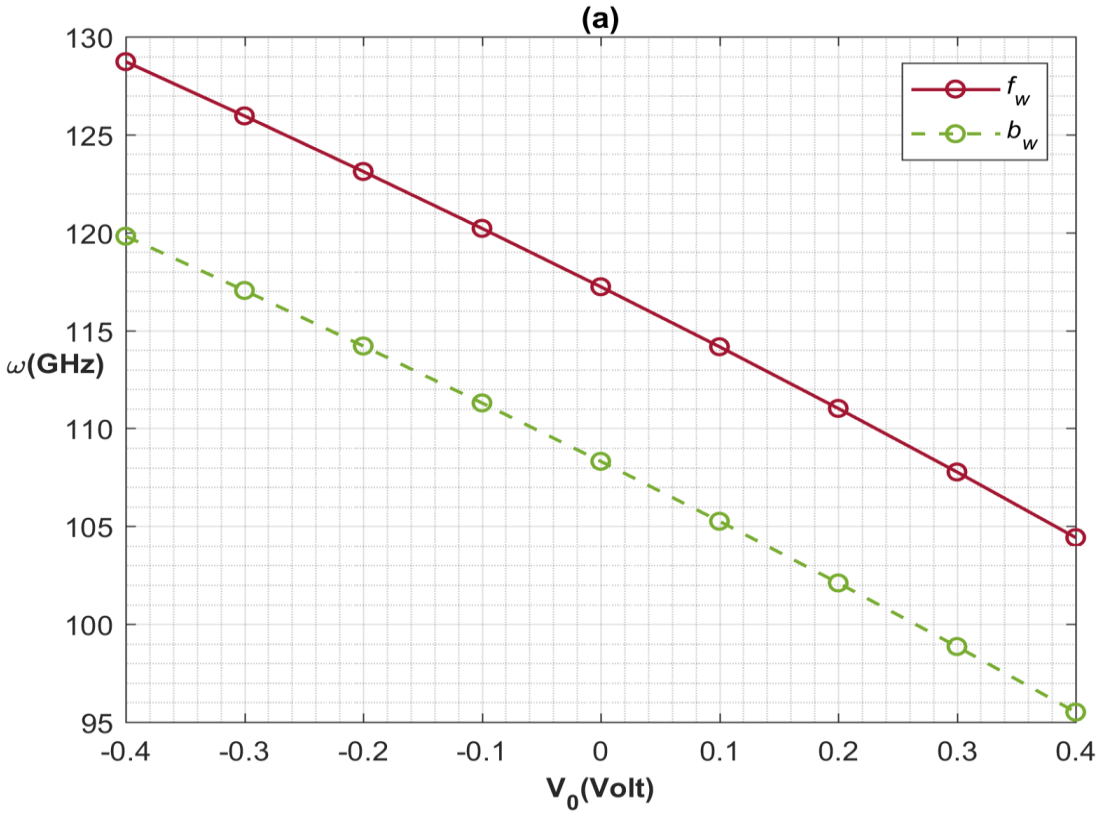

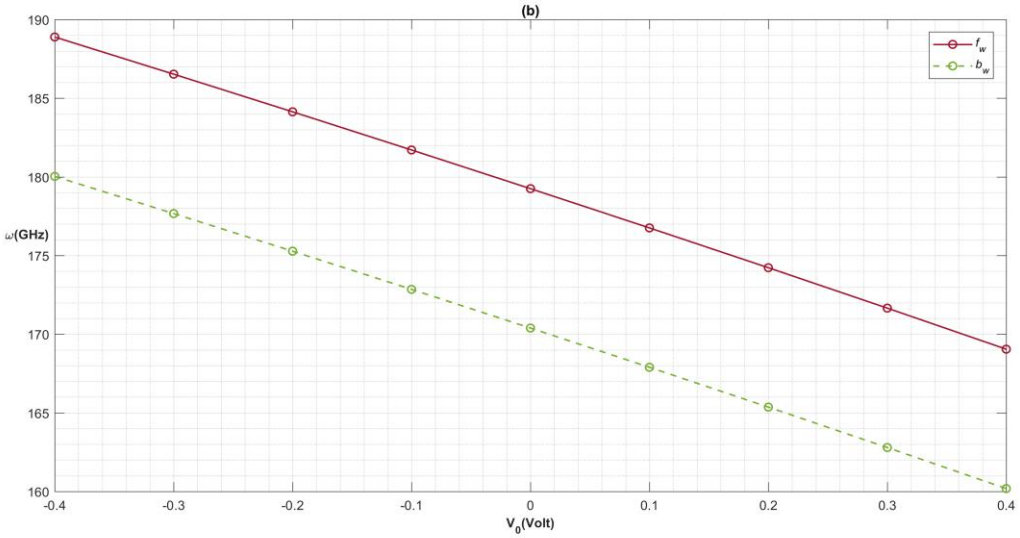
(b)
190
185
180
175
170
165
160
ω(GHz)
-0.4
-0.3
-0.2
-0.1
0
0.1
0.2
0.3
0.4
V0(Volt)
fw
bw

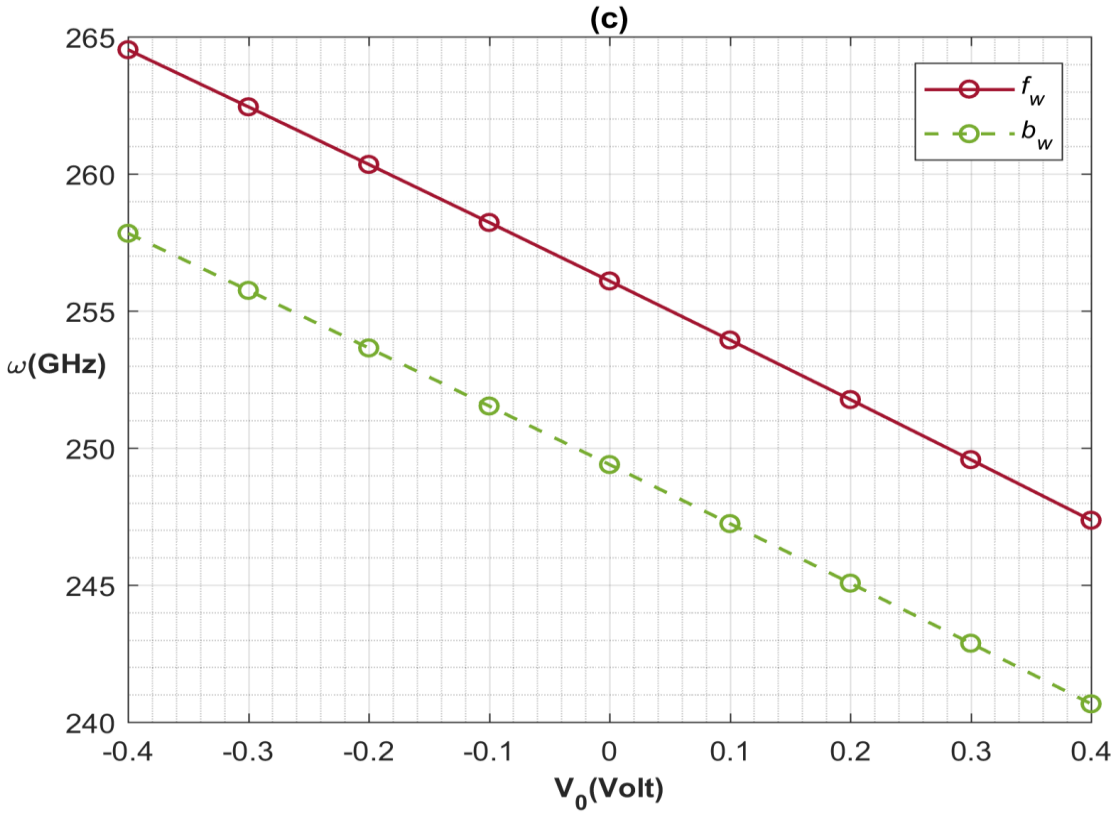
(c)
265
260
255
250
245
240
ω(GHz)
-0.4
-0.3
-0.2
-0.1
0
0.1
0.2
0.3
0.4
V0(Volt)
fw
bw

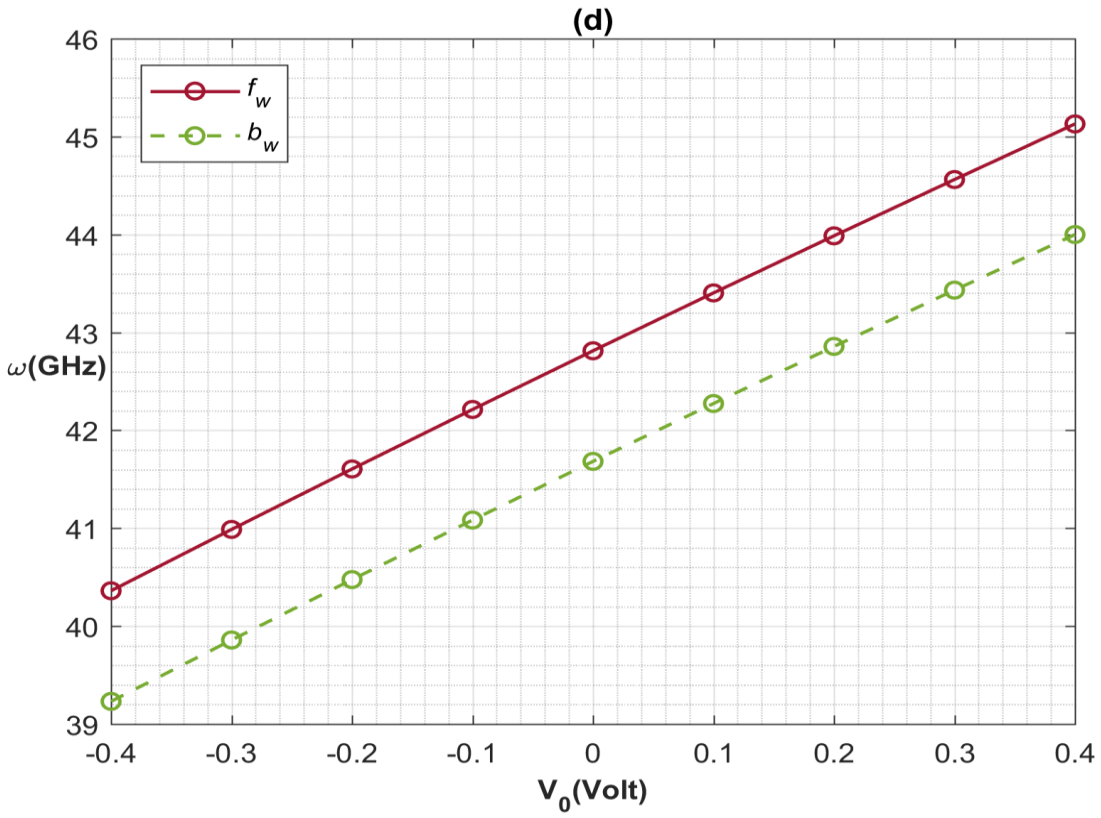

Figure 4.4: Variations of the forward and backward whirls (GHr) of spinning smart nanoshaft for different applied external voltage : (a) S-S, (b) C-S, (c) C-C, (b) C-F ($\frac{L}{D} = 15,\ \eta = 1.3nm, l = 0.4nm,\ \Delta\mathrm{T} = 0$)

4.2.4 The effect of temperature change

Figures 4.4 and 4.5 illustrate the impact of temperature change on the forward and backward whirl frequencies under room and high-temperature conditions, respectively, across various boundary configurations.

At room temperature, as depicted in Figure 4.4, an increase in temperature change reduces the structural rigidity of the smart nanoshaft, resulting in a decrease in whirling frequencies. This trend is consistent across simply supported-simply supported (S-S), clamped-simply supported (C-S), and clamped-clamped (C-C) boundary conditions, as shown in Figures 4.4 (a-c). However, the clamped-free (C-F) boundary condition exhibits a contrasting behavior, where temperature increases lead to higher whirling frequencies.

The analysis extends to high-temperature scenarios in Figure 4.5, revealing a distinct set of behaviors. Under high temperatures, increasing the temperature differential enhances the structural rigidity of the smart nanoshaft for S-S, C-S, and C-C boundary conditions. This increased rigidity manifests as higher forward and backward whirl frequencies. Once again, the C-F boundary condition stands out, displaying an inverse relationship between temperature change and whirling frequencies.

These outcomes highlight the intricate relationship between thermal impacts, boundary conditions, and the dynamic behavior of smart nanoshafts. The observed temperature-

dependent responses underscore the necessity of taking thermal considerations into account when designing and operating nanoelectromechanical systems, especially in situations with considerable temperature changes.

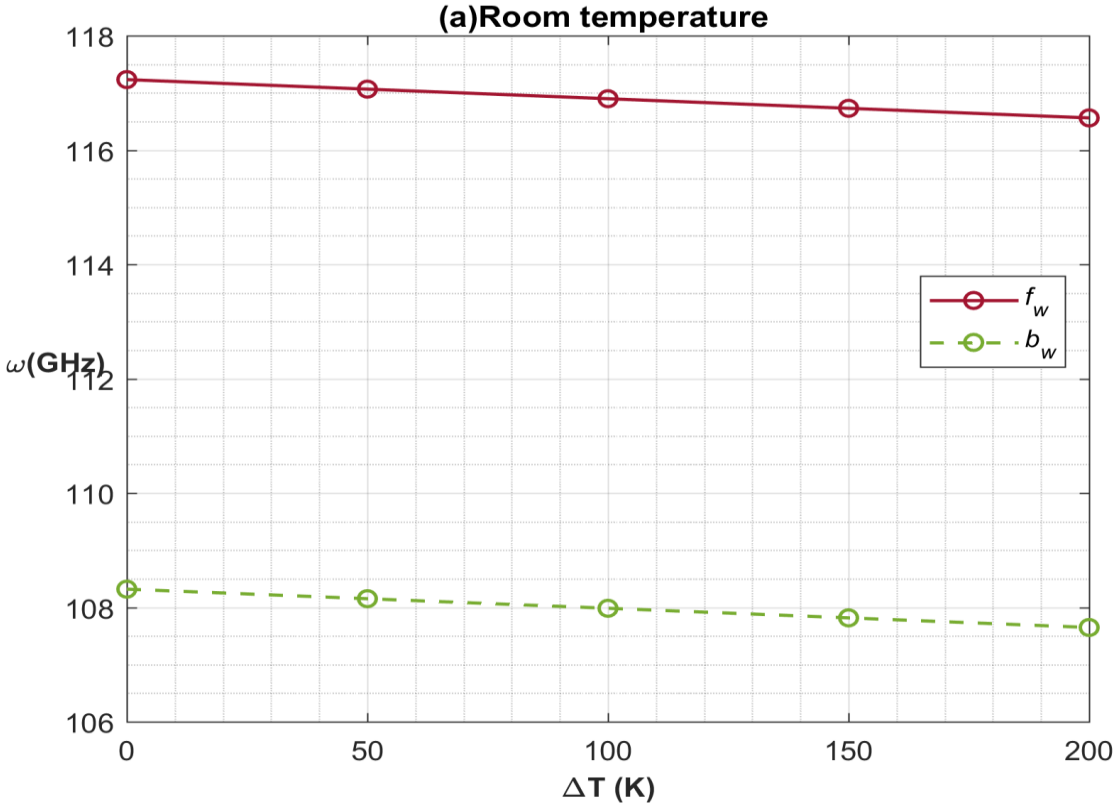

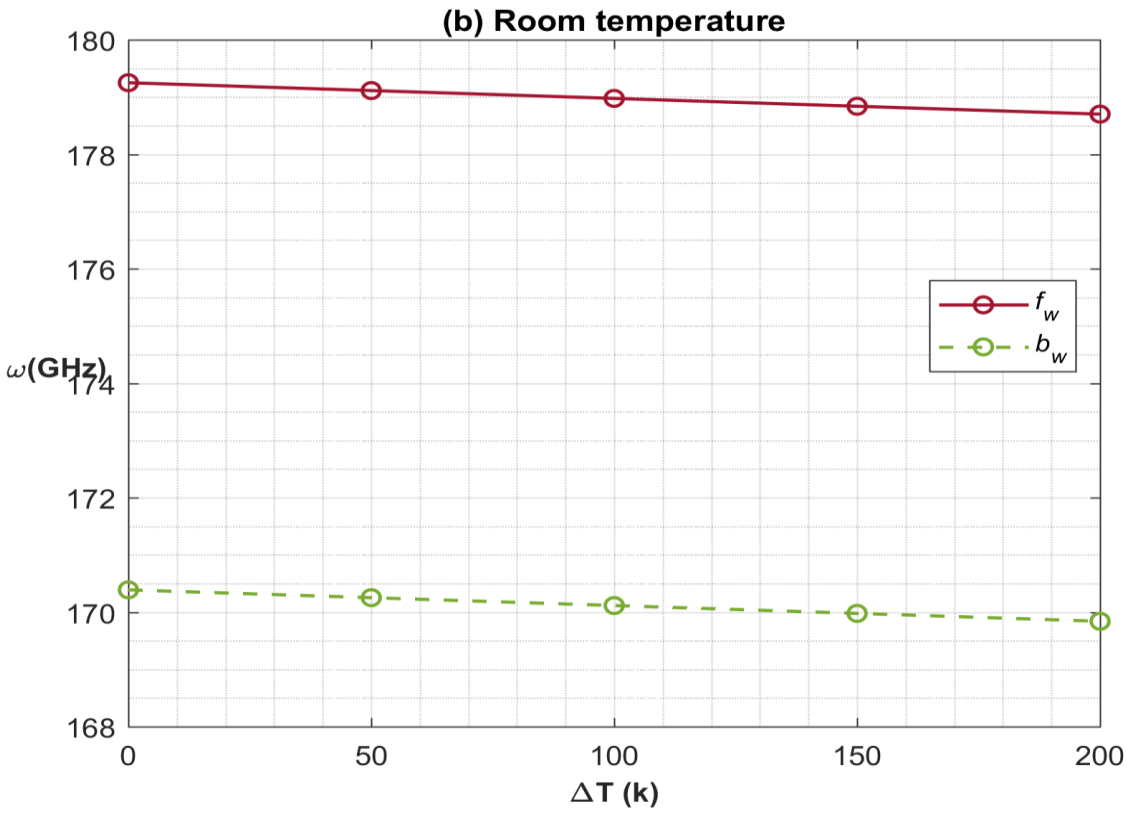

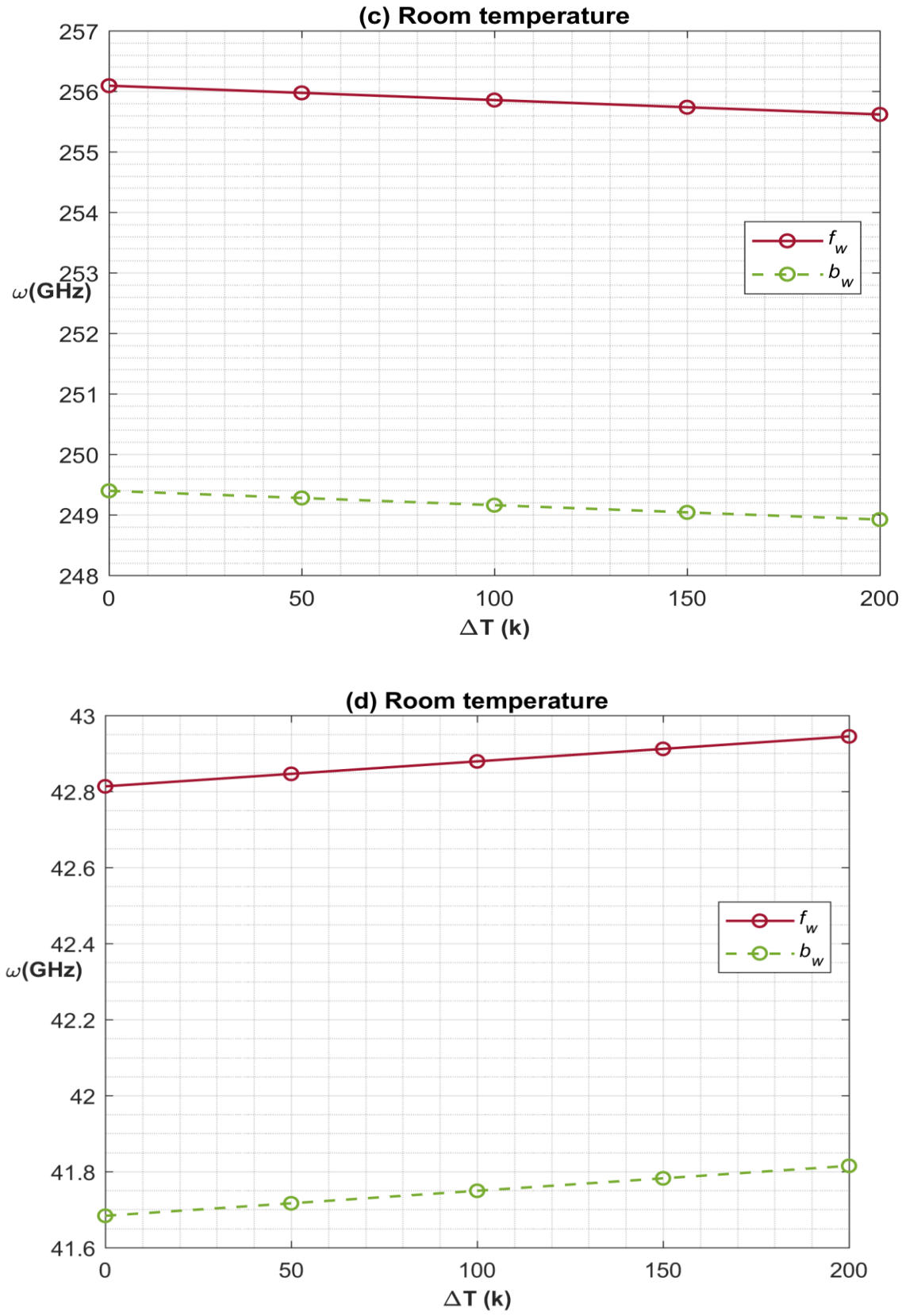

Figure 4.5: Variations of the forward and backward whirls (GHr) of spinning smart nanoshaft for different temperature under room temperature : (a) S-S, (b) C-S, (c) C-C, (b) C-F ($\frac{L}{D} = 15$, $\eta = 1.3nm, l = 0.4nm,\ V_0 = 0$)

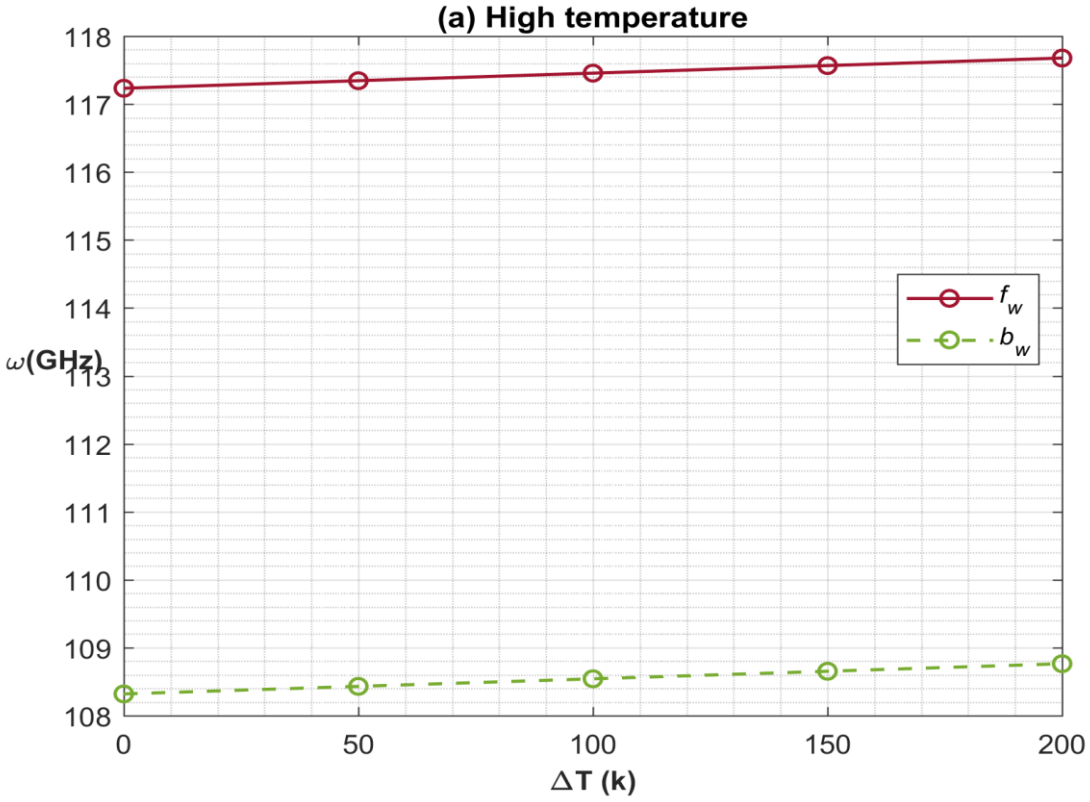
(a) High temperature
118
117
116
115
114
113
112
111
110
109
108
ω(GHz)
0
50
100
150
200
ΔT (k)
f_w
b_w

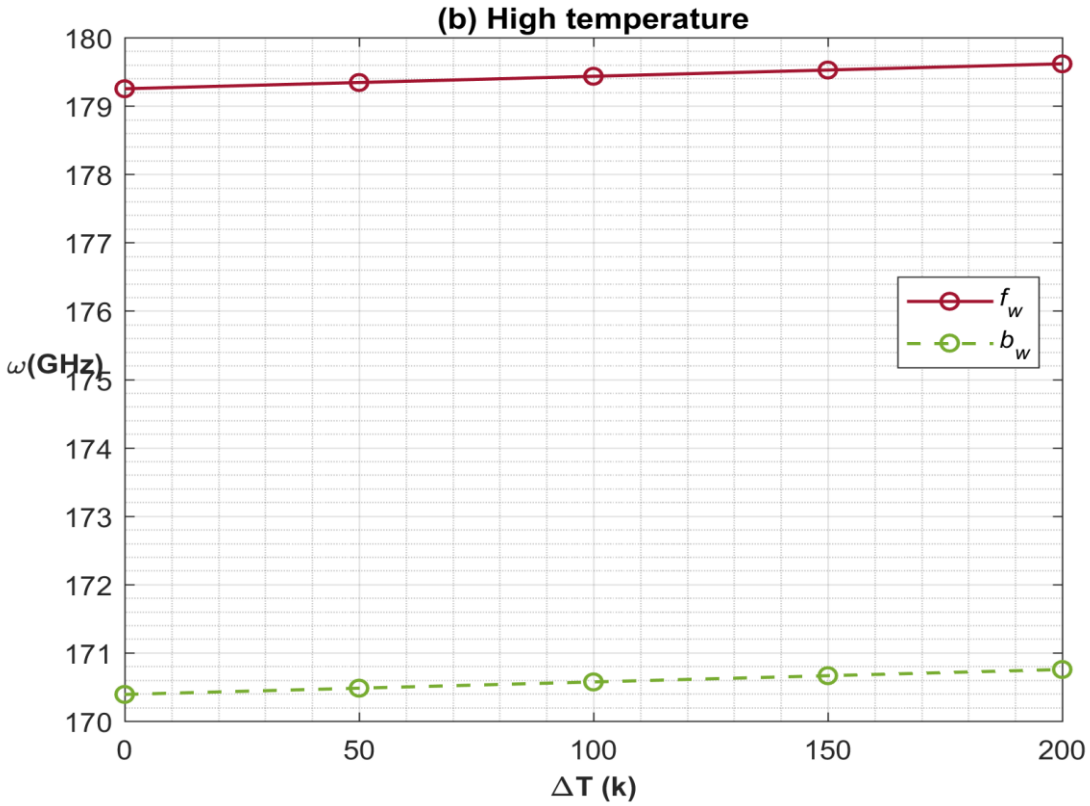
(b) High temperature
180
179
178
177
176
175
174
173
172
171
170
ω(GHz)
0
50
100
150
200
ΔT (k)
f_w
b_w

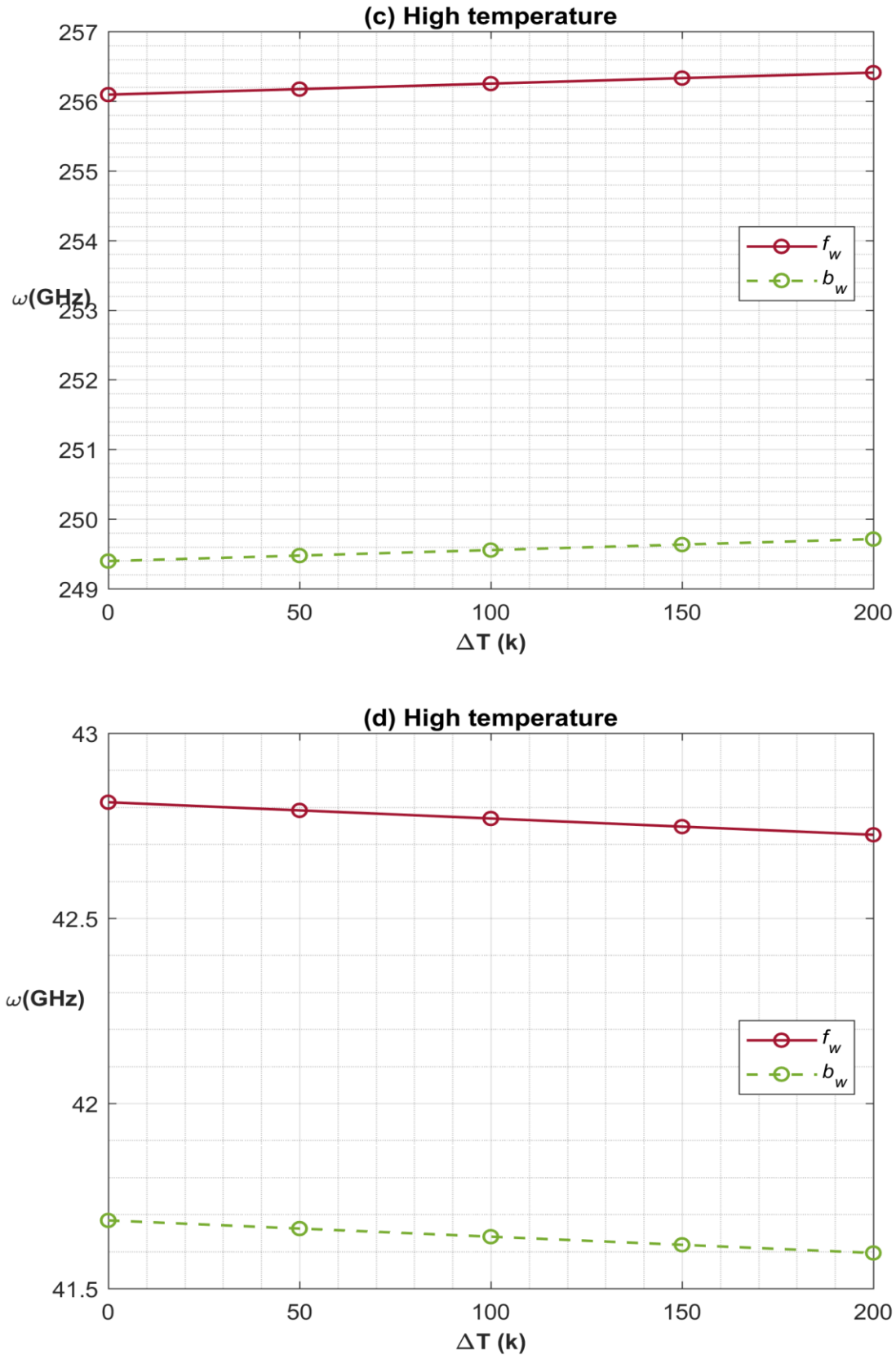

Figure 4.6: Variations of the forward and backward whirls (GHr) of spinning smart nanoshaft for different temperature under high temperature : (a) S-S, (b) C-S, (c) C-C, (b) C-F ($\frac{L}{D} = 15$, $\eta = 1.3nm, l = 0.4nm,\ V_0 = 0$)

4.2.5 The Slenderness ration effect

In our study of rotating smart nanoshafts, we utilize an armchair (6,6) SWBNNT as the base material. The nanotube's diameter is determined by its chirality, while its thickness is based on optimal values derived from previous (MD) simulations, crucial for accurate vibrational response modeling.

We investigate the impact of varying Slenderness Ratio on forward and backward whirls across different boundary conditions, adhering to the Euler-Bernoulli beam theory's recommended Allowable Slenderness Ratio of $L/D \geq 10$. Our findings, illustrated in **Figure** 4.7, show that increasing the slenderness ratio decreases whirling frequency uniformly across all boundary conditions, reducing nanotube stiffness and causing convergence of forward and backward whirls, thus diminishing the spinning speed effect.

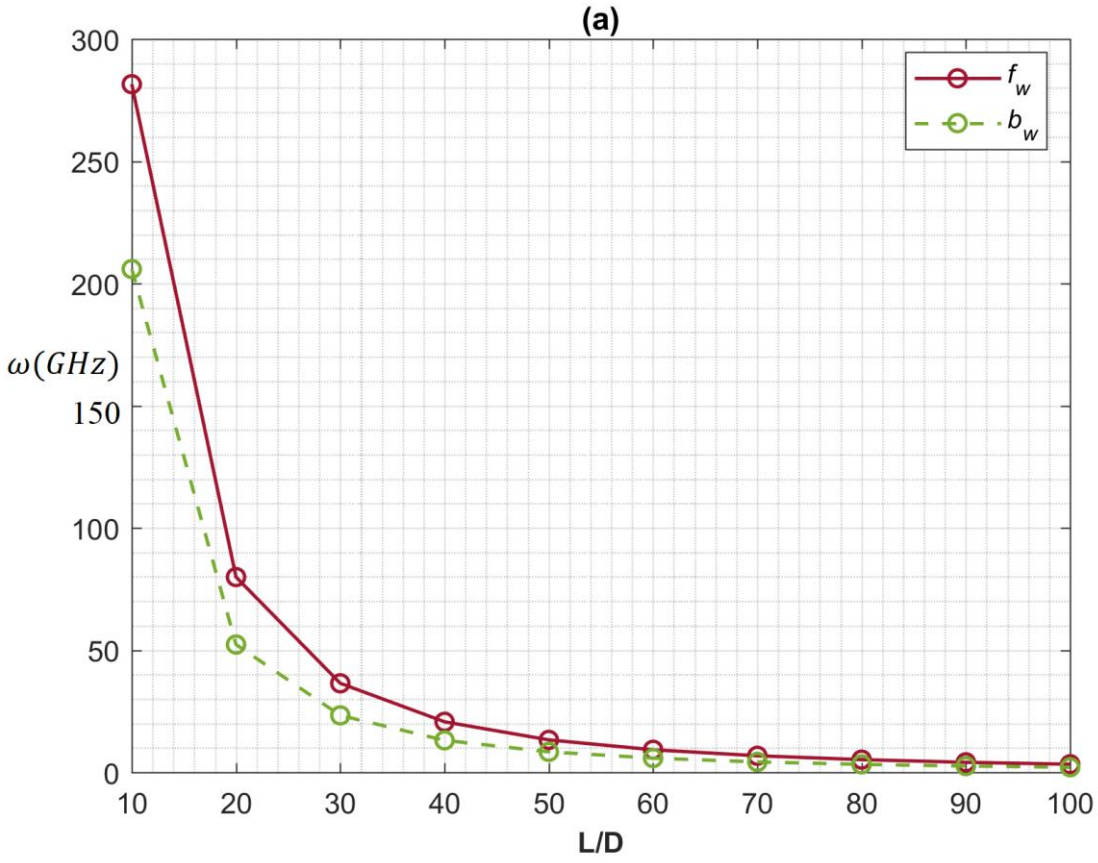

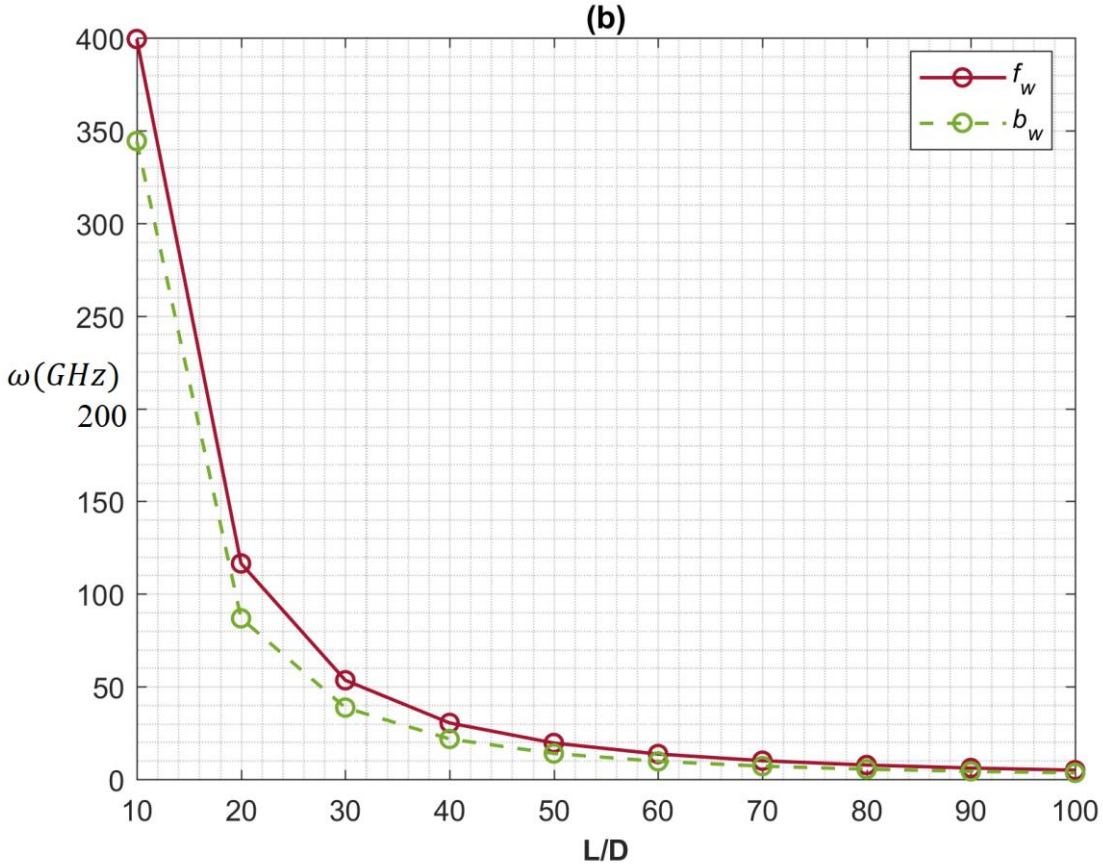
(b)
f_w
b_w
$\omega(GHz)$
L/D
0
50
100
150
200
250
300
350
400
10
20
30
40
50
60
70
80
90
100

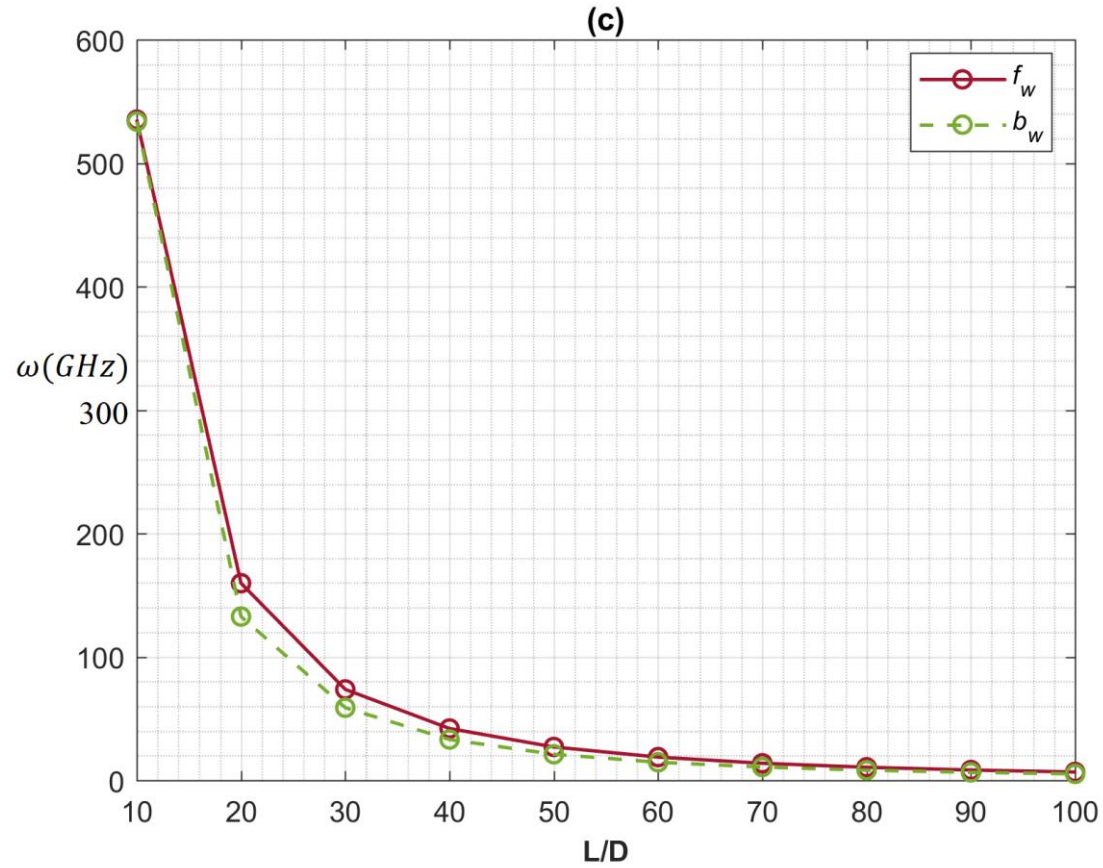
(c)
f_w
b_w
$\omega(GHz)$
L/D
0
100
200
300
400
500
600
10
20
30
40
50
60
70
80
90
100

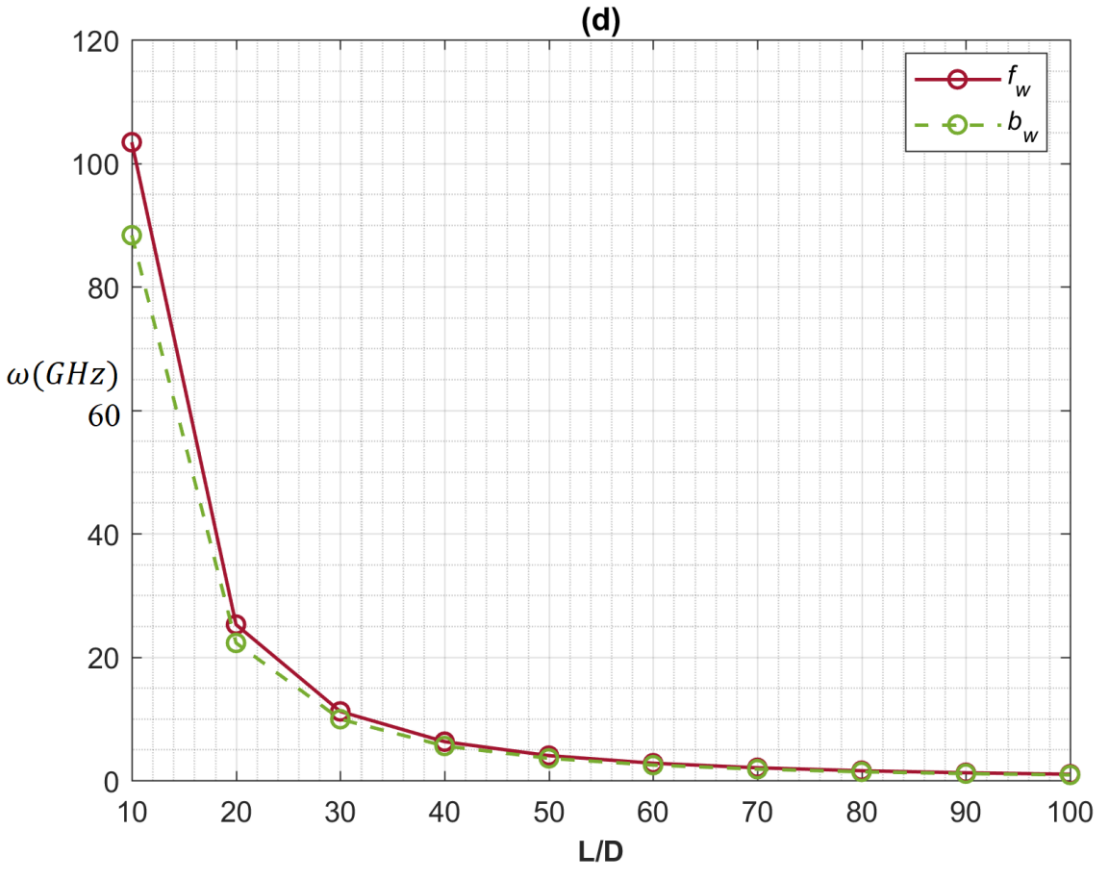

Figure 4.7: Variations of the forward and backward whirls (GHr) of spinning smart nanoshaft for different length-to-diameter ratio: (a) S-S, (b) C-S, (c) C-C, (b) C-F ($\frac{L}{D} = 15,\ \eta = 1.3nm, l = 0.4nm,\ V_0 = 0,\ \Delta\mathrm{T} = 0$)

Notably, at a length-to-diameter ratio (L/D) of 10, the disparity between forward and backward whirls is more pronounced. This difference narrows when transitioning from simply supported (S-S) to clamped-clamped (C-C) boundary conditions. We conclude that boundary conditions imposing greater end constraints, such as C-C, mitigate the rotating speed effect, offering insights into optimal design parameters for smart nanotubes in various applications.

The effect of the initial hoop tension

This section investigates the effect of initial hoop tension due to centrifugal force under high rotational speeds. **Table** 4.8 illustrates the variation of the first and second forward and backward whirls as a function of rotational speed, both with and without considering initial hoop tension, for all boundary conditions. The data reveals that initial hoop tension reduces forward and backward whirls in simply supported (S-S), clamped-simply supported (C-S), and clamped-clamped (C-C) boundary conditions. Consequently, accounting for initial hoop tension at high rotational speeds decreases the stiffness of the smart nanoshaft, while neglecting it at high speeds leads to counterintuitive results. Conversely, in the clamped-free (C-F) boundary condition, initial hoop tension enhances the stiffness of the smart nanoshaft, resulting in an increase in whirling frequency.

Table 4.8: Variations of the first-second forward and backward whirl of spinning smart nanoshaft with and without considering hoop tension

BCs	$\Omega(THz)$	Whirls Type	Without centrifugal force		With centrifugal force	
			1 mode	2 mode	1 mode	2 mode
S-S	1	f_w	117.17	411.23	104.64	400.45
		b_w	105.68	394.05	93.160	383.27
	1.5	f_w	120.22	415.64	89.408	390.90
		b_w	103.00	389.87	72.187	365.18
	2	f_w	123.35	420.10	55.912	375.04
		b_w	100.39	385.74	32.951	340.8
C-S	1	f_w	179.25	509.04	171.25	498.58
		b_w	170.39	497.39	162.39	486.93
	1.5	f_w	181.53	512.00	162.97	488.15
		b_w	168.24	494.52	149.68	470.67
	2	f_w	183.84	514.97	149.18	471.72
		b_w	166.12	491.66	131.46	448.42
C-C	1	f_w	256.09	616.32	249.23	605.89
		b_w	249.39	613.36	242.53	602.93
	1.5	f_w	257.79	617.06	242.08	593.33
		b_w	247.74	612.62	232.03	588.89
	2	f_w	259.50	617.80	230.82	574.94
		b_w	246.11	611.88	217.42	569.02
C-F	1	f_w	43.889	251.74	44.648	244.48
		b_w	41.679	243.97	43.518	236.71
	1.5	f_w	43.096	253.72	47.132	237.07
		b_w	41.401	242.06	45.436	225.12
	2	f_w	43.385	255.71	50.330	225.25
		b_w	41.125	240.18	48.071	209.71

4.3 Summary

This chapter explored the thermo-electro-mechanical behavior of rotating smart nanoshafts, with particular attention to the hoop tension induced by centrifugal forces at high rotational speeds. Our analytical framework integrated the Euler-Bernoulli beam model with nonlocal strain gradient piezoelectric elasticity theory to comprehensively address both small-scale and piezoelectric effects. Through a semi-analytical approach using Galerkin-based closed-form solutions, we uncovered several significant findings, which were subsequently validated through rigorous comparisons with existing literature.

Our analysis revealed that increasing rotational speed elevates forward frequencies while diminishing backward frequencies. The influence of vibration modes on the gyroscopic effect varies according to boundary conditions. Several parameters—including the nonlocal parameter, positive external voltage, room temperature condition, and initial hoop tension—demonstrate stiffness-softening characteristics, resulting in decreased natural frequencies. Conversely, the material length scale, negative external voltage, and high-temperature

conditions exhibit stiffness-hardening properties, leading to increased frequencies. Notably, these effects are reversed under C-F boundary conditions.

The study also highlighted the significant impact of slenderness ratios, where increases lead to simultaneous reductions in both forward and backward natural frequencies. This influence proved more substantial than that of the nonlocal parameter. The subsequent chapter will investigate stability dynamics under thermo-electrical conditions using nonlocal strain gradient piezoelectric theory, specifically examining variations in the resonance critical speed of smart nanoshafts

Chapter 5

Stability analysis of rotating smart nanoshaft under thermo-electrical loading

Objective:

This chapter comprises two primary sections. The first presents a thorough comparative analysis of our findings against existing literature, validating the precision and dependability of our approach. The second section details an extensive parametric investigation exploring the impact of crucial factors on the critical speed and stability of the smart nanoshaft. These factors include size-dependent parameters, external voltage, temperature fluctuations, centrifugal force, and geometric variations. This comprehensive examination offers valuable insights into the smart nanoshaft's dynamic properties and performance across diverse operational conditions.

5.1 Comparative study.

5.2 Parametric study.

5.1 Comparative study

Critical speed is a fundamental concept in the dynamic behavior of rotordynamic systems. It is defined as the rotational speed at which the natural frequency of a rotating shaft or shaft-disc assembly coincides with the system's rotational frequency, inducing resonance. For nanoscale rotors, critical speed remains a crucial parameter in predicting the stability of these nanodevice rotors.

Our comprehensive literature review reveals a significant gap in experimental results and theoretical studies investigating the stability characteristics of smart nanoshafts. Notably, the backward whirl (b_w) wave typically exhibits a smaller amplitude than the forward whirl (f_w) wave, underscoring the importance of accurately predicting the b_w critical speed.

To validate our approach, we conducted a comparative analysis of the first four critical speeds of a rotating macro-shaft under simply supported (S-S) boundary conditions (see **Table** 5.1). Our calculations, based on local Euler-beam theory and the Galerkin technique, were benchmarked against the results of Mirtalaie et al.,[120] who employed Timoshenko beam theory and an exact multiple scales method. For this comparison, we disregarded size-dependent, piezoelectric, and thermal effects to ensure a focused analysis.

Table 5.1 presents this comparative study, utilizing the following mechanical and geometrical parameters: Young's modulus($E = 200\,GPa, \rho = 7860\frac{kg}{m^2}, L = 1\,m, and\, r = 0.015\,m$). The close alignment of our results with the cited literature strongly suggests that our mathematical formulation accurately captures the stability dynamics of spinning smart nanotubes, thereby validating the robustness of our methodology.

Table 5.1: Comparison of the backward critical speeds of a simply supported shaft ($E = 200$ GPa$, \nu = 0.3, \rho = 7860\frac{Kg}{m^2}, r = 0.015, L = 1nm$)

Mode number	$\Omega_{cr}(\frac{rad}{s})$		
	Mirtalaie et al.[120]	Present	Err %
1	373.1917	373.1846	$1.9e^{-3}$
2	1490.379	1490.261	$7.91e^{-5}$
3	3344.502	3343.859	$1.92e^{-4}$
4	5924.133	5921.897	$3.77e^{-4}$

Our results align well with the cited literature, suggesting that our mathematical formulation accurately captures the stability dynamics of spinning smart nanotubes.

5.2 Parametric Study

5.2.1 Effect of non local parameter

This section examines the impact of nonlocal parameters on critical speed and the system's dynamic stability for for with and without centrifugal force. **Figure** 5.1 illustrates the fundamental relationship between critical speed and the nonlocal parameter under various

boundary conditions. For simply supported (S-S), clamped-simply supported (C-S), and clamped-clamped (C-C) boundary conditions, an increase in nonlocal parameters results in a decrease in critical speed. This leads to reduced stability of the smart nanoshaft, indicating that the nonlocal parameter has a stiffness-softening effect on the dynamic stability of the smart nanoshaft. Conversely, under clamped-free (C-F) boundary conditions, the nonlocal parameter reverses its effect, playing a stiffness-hardening role and causing an increase in critical speed. Notably, this opposite effect of nonlocal parameters enhances the dynamic stability of the nanotube.

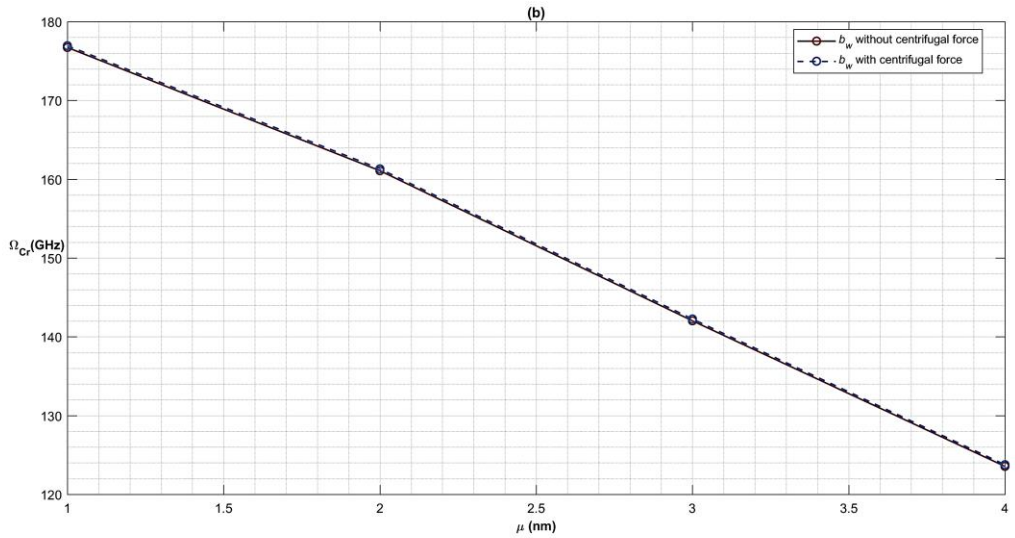

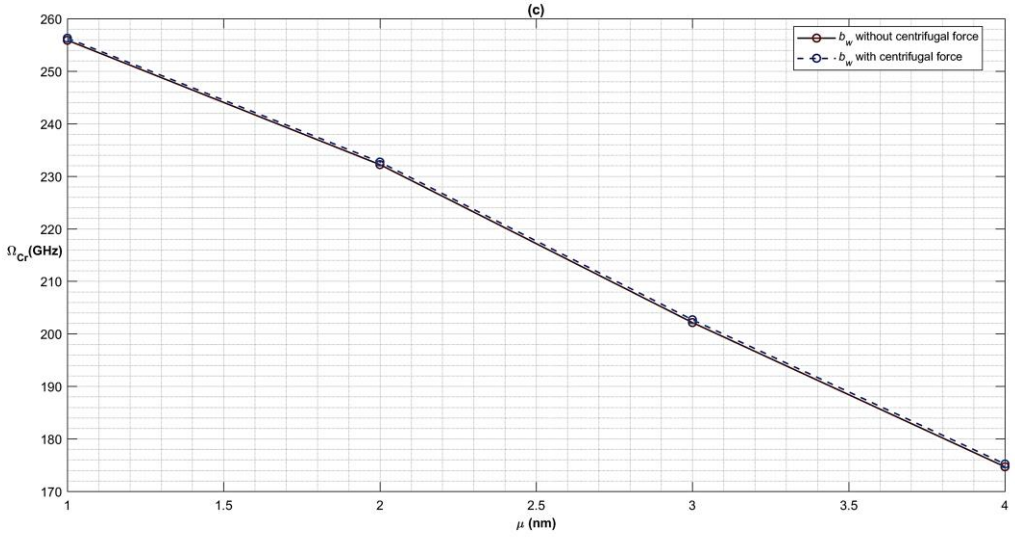

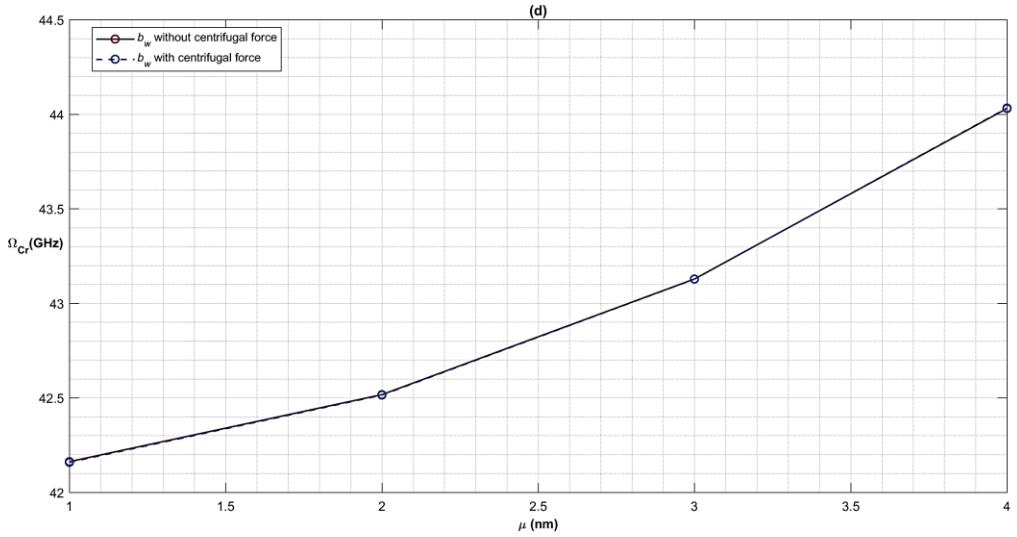

Figure 5.1: Effect of the nonlocal parameter on backward critical speed across different boundary conditions, both with and without consideration of hoop tension effects: (a) S-S, (b) C-S, (c) C-C, (b) C-F ($\frac{L}{D} = 15, l = 0.4nm,\ V_0 = 0, \Delta T = 0$)

As illustrated in **Figure** 5.1, centrifugal force has minimal impact on the critical resonance speed, given that this speed more closely aligns with the nanotube's frequency in its stationary state. In this scenario, the nanotube is not spinning at high velocities.

5.3 Effect of strain gradient parameter

This section investigates how the strain gradient term affects critical speed and dynamic stability of the system, considering scenarios both with and without centrifugal force. **Figure** 5.2 depicts the fundamental relationship between critical speed and the strain gradient term across various boundary conditions. For simply supported (S-S), clamped-simply supported (C-S), and clamped-clamped (C-C) configurations, increasing the strain gradient parameters leads to higher critical speeds. This enhancement in critical speed improves the smart nanoshaft's stability, suggesting that the strain gradient parameter has a stiffening effect on the system's dynamic stability. However, under clamped-free (C-F) boundary conditions, the strain gradient parameter exhibits an opposite effect. In this case, it acts as a softening factor, resulting in decreased critical speed. This contrasting behavior of strain gradient parameters in the C-F configuration diminishes the smart nanoshaft's dynamic stability.

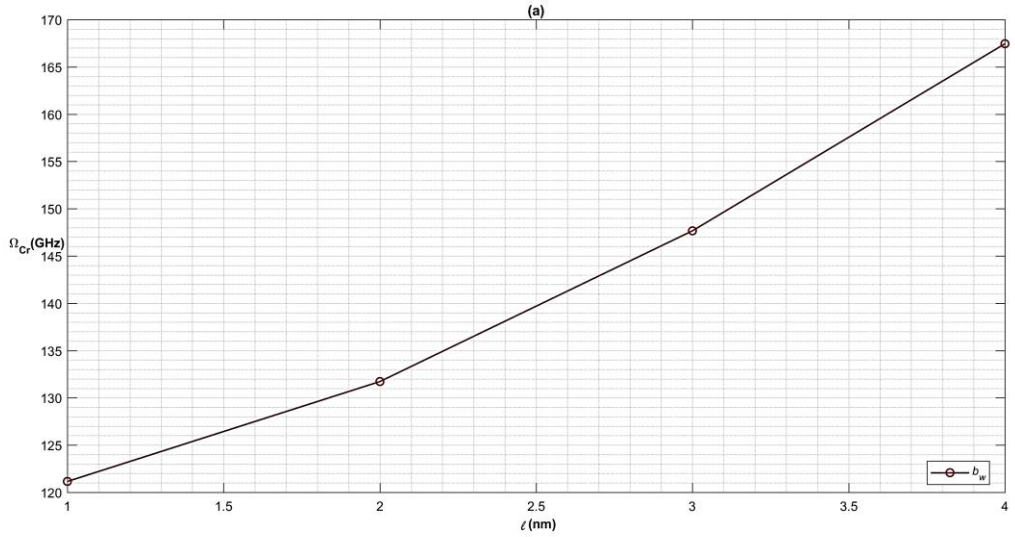
(a)
Ω_{Cr}(GHz)
ℓ (nm)
b_w

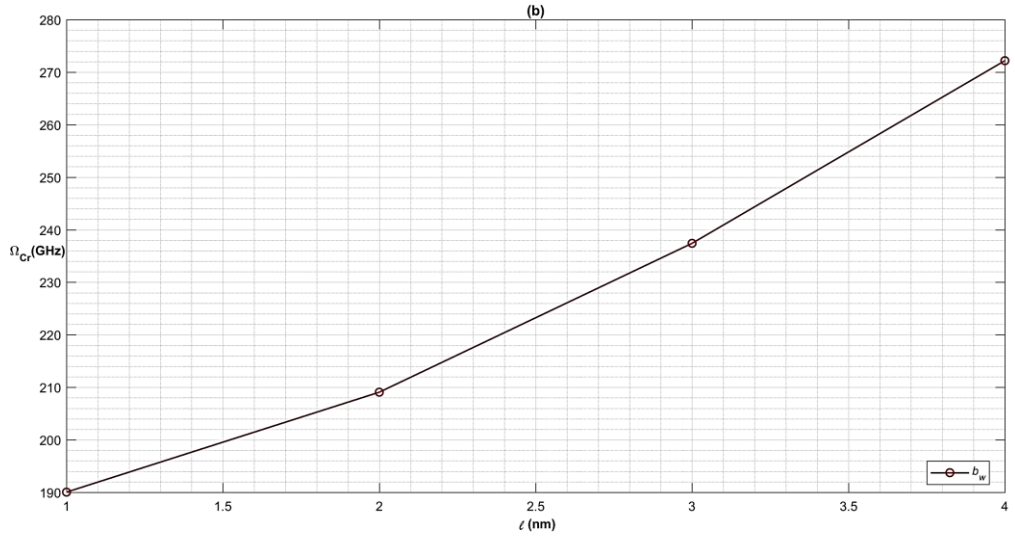
(b)
Ω_{Cr}(GHz)
ℓ (nm)
b_w

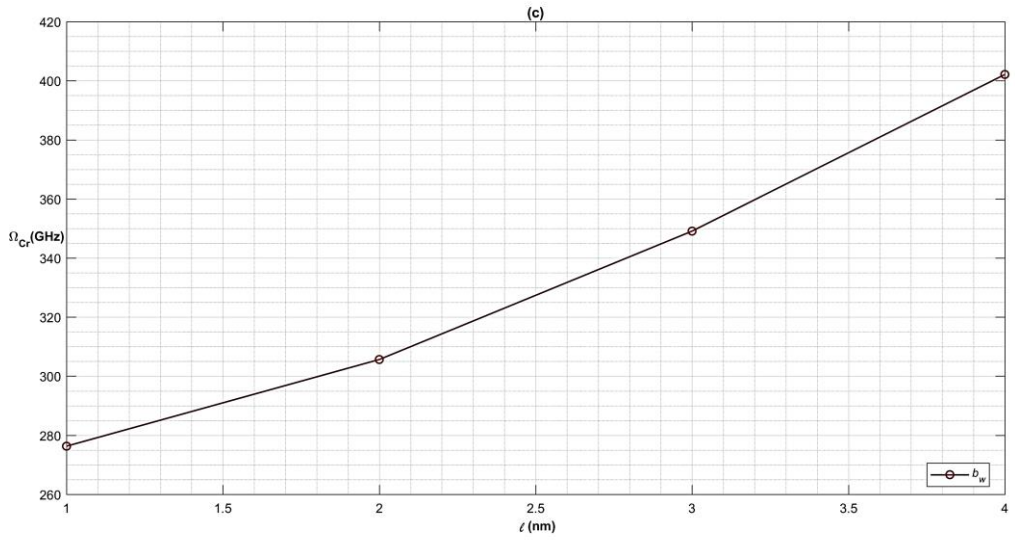
(c)
Ω_{Cr}(GHz)
ℓ (nm)
b_w

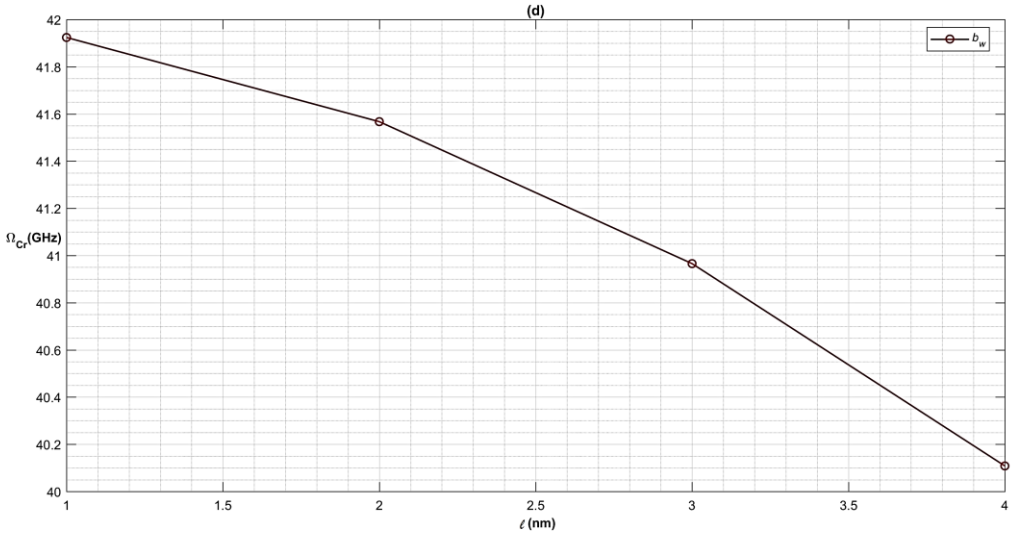

Figure 5.2: Effect of the material length scale parameter on backward critical speed across different boundary conditions, both with and without consideration of hoop tension effects: $(\frac{L}{D} = 15,\ \eta = 1.3nm,\ V_0 = 0, \Delta\mathrm{T} = 0\ )$

Figure 5.2 also demonstrates that centrifugal force has minimal impact on the critical resonance speed. Notably, size-dependent parameters do not alter the effect of centrifugal force. This is because the critical speed closely approximates the natural frequency in the stationary case. Consequently, the centrifugal force term will be disregarded in subsequent analyses throughout this chapter.

5.3.1 Effect of applied external voltage

In this section, we examine the piezoelectric effect on the system's stability dynamics, particularly focusing on the impact of applied external voltage on critical speed. **Figure** 5.3 illustrates the relationship between applied external voltage and critical spinning speed across various boundary conditions and mode numbers.

Figures 5.3 (a-c), which depict S-S, C-S, and C-C boundary conditions, demonstrate that applying a negative voltage increases the critical speed, thereby enhancing the system's stability dynamics. Conversely, applying a positive voltage decreases the critical speed, resulting in reduced stability dynamics of the smart nanoshaft. This trend is consistent across all mode numbers.

The analysis then shifts to the C-F boundary condition, where the applied external voltage shows no effect on the first frequency mode. However, for the second and higher mode numbers, the impact of applied external voltage aligns with the patterns observed in other boundary conditions.

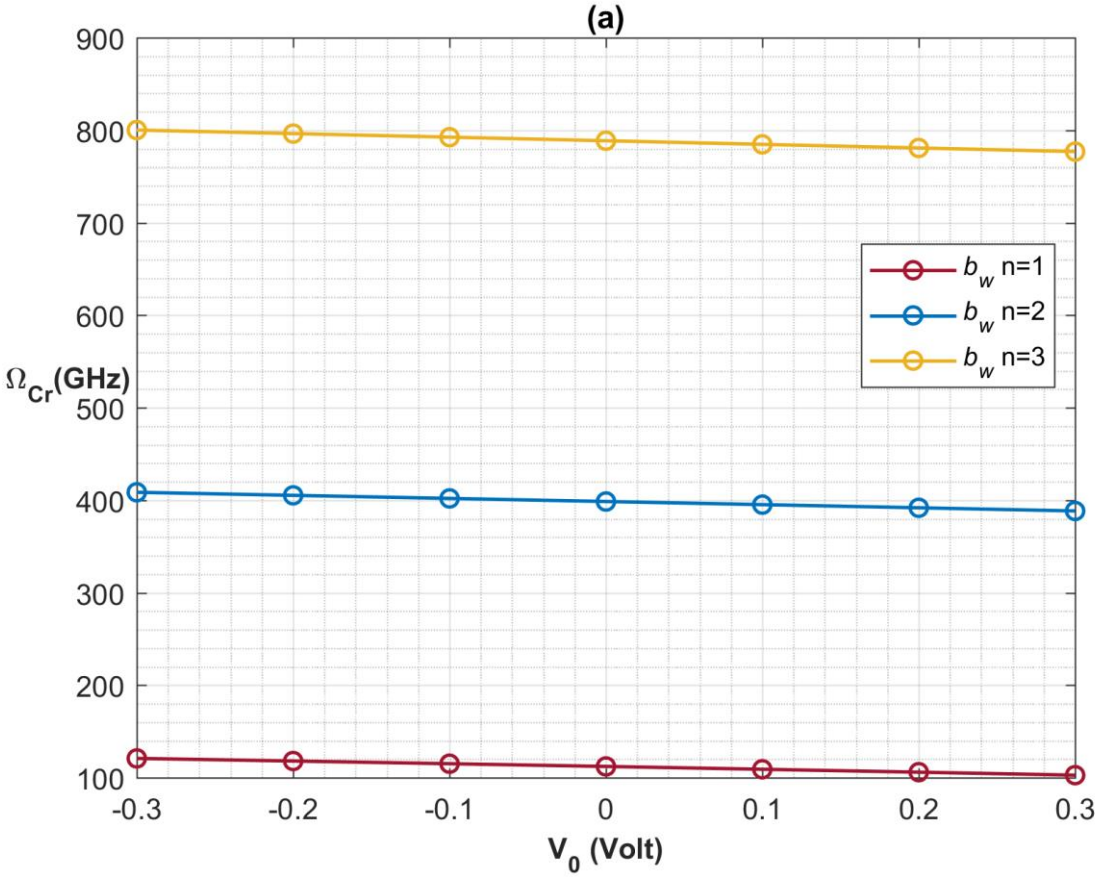
(a)
900
800
700
600
500
400
300
200
100
Ω_{Cr}(GHz)
-0.3
-0.2
-0.1
0
0.1
0.2
0.3
V_0 (Volt)
b_w n=1
b_w n=2
b_w n=3

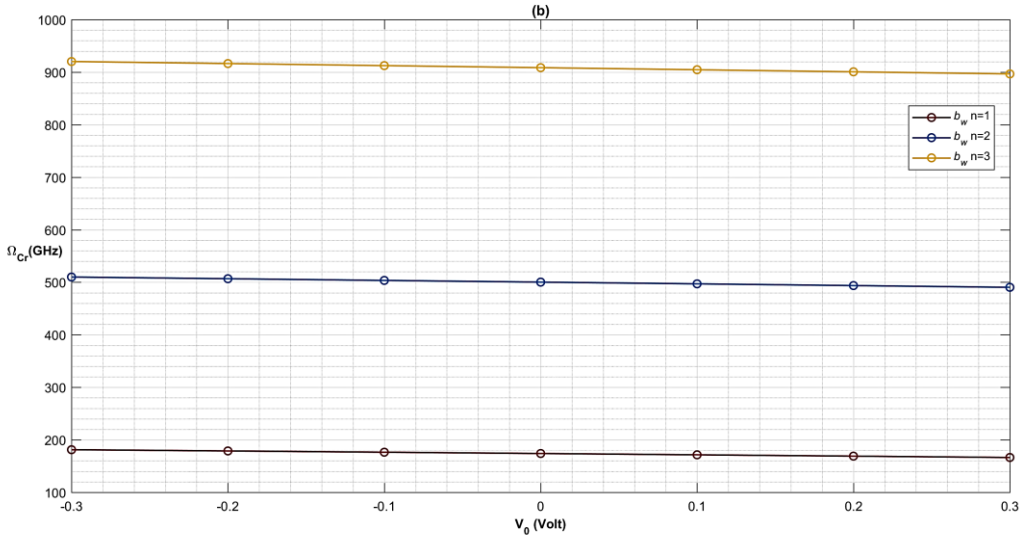
(b)
1000
900
800
700
600
500
400
300
200
100
Ω_{Cr}(GHz)
-0.3
-0.2
-0.1
0
0.1
0.2
0.3
V_0 (Volt)
b_w n=1
b_w n=2
b_w n=3

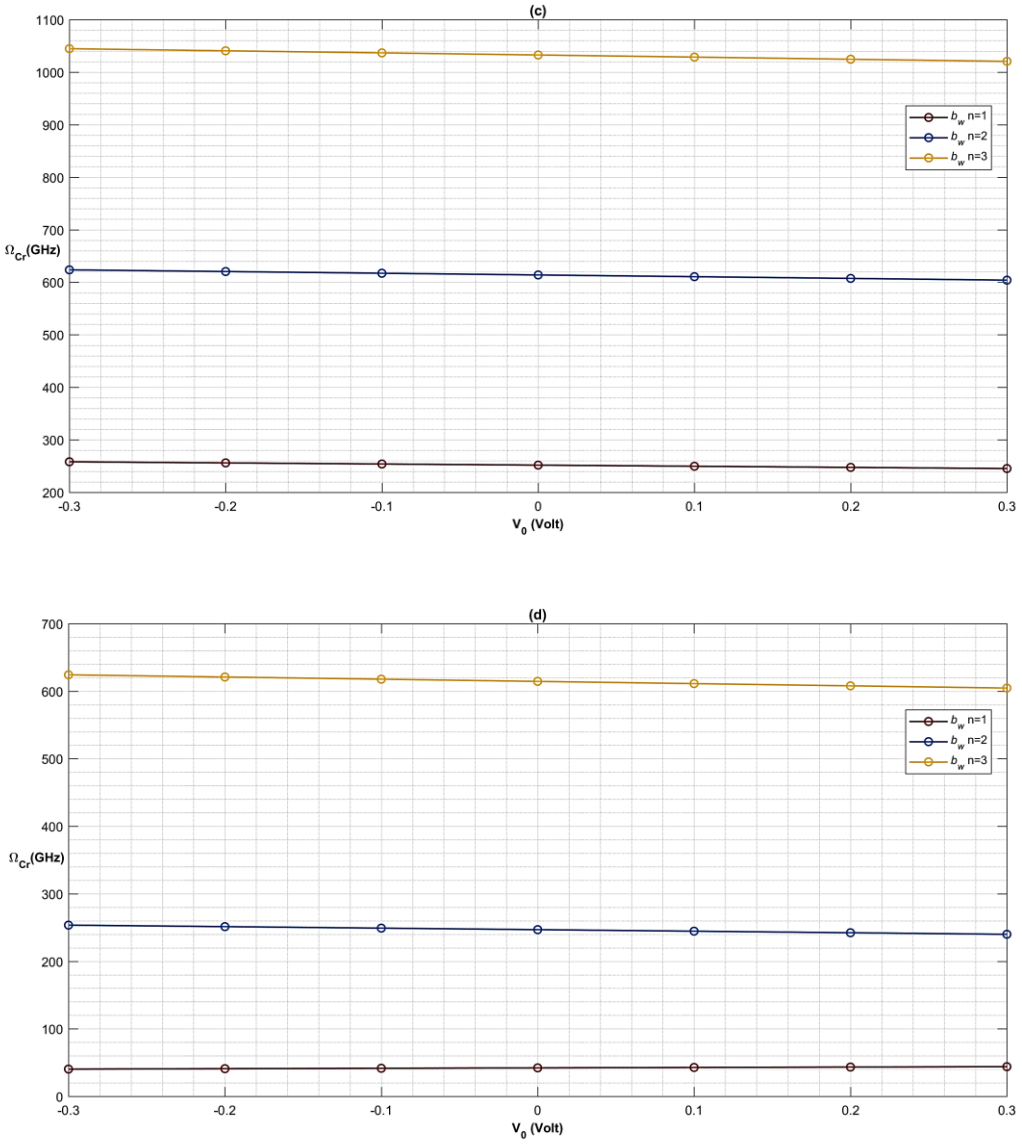

Figure 5.3: Effect of the applied external voltage on first-third backward critical speed across different boundary conditions: (a) S-S, (b) C-S, (c) C-C, (b) C-F ($\frac{L}{D} = 15,\ \eta = 1.3nm, l = 0.4nm, \Delta \mathrm{T} = 0$)

5.3.2 The effect of temperature change

This section examines the impact of temperature variations on the system's critical speed and stability dynamics, considering both room and high temperatures across all boundary conditions. Analysis of **Figure** 5.4 and **Figure** 5.5 reveals a notable finding: temperature changes do not significantly influence the system's critical speed, and stability is maintained regardless of thermal changes. This phenomenon is consistently observed across all boundary conditions tested.

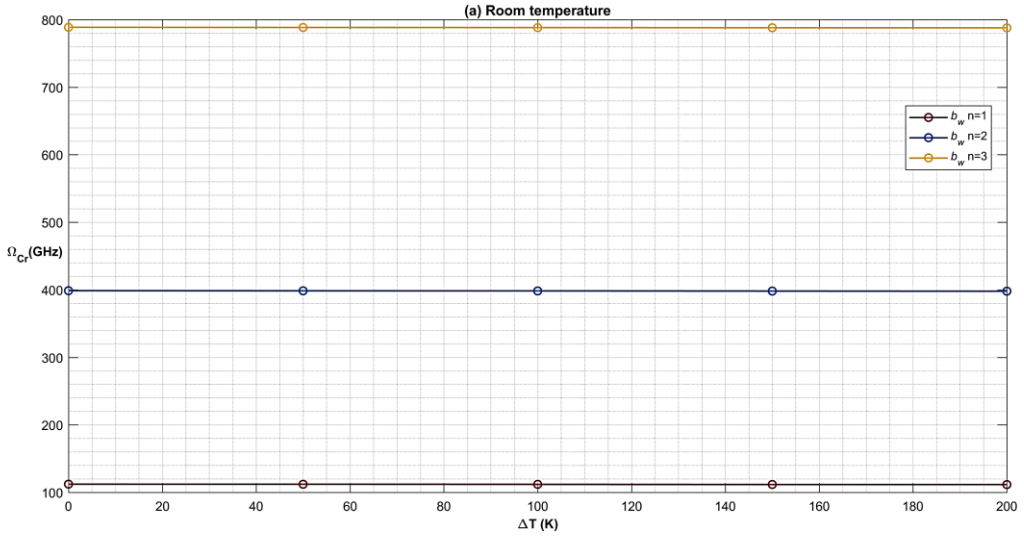
(a) Room temperature
Ω_{Cr}(GHz)
ΔT (K)
b_w n=1
b_w n=2
b_w n=3

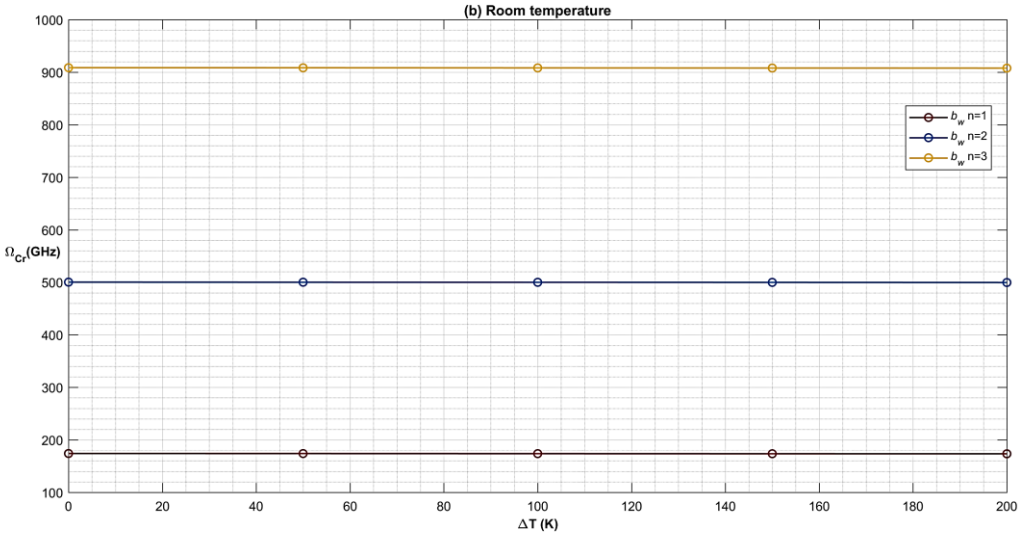
(b) Room temperature
Ω_{Cr}(GHz)
ΔT (K)
b_w n=1
b_w n=2
b_w n=3

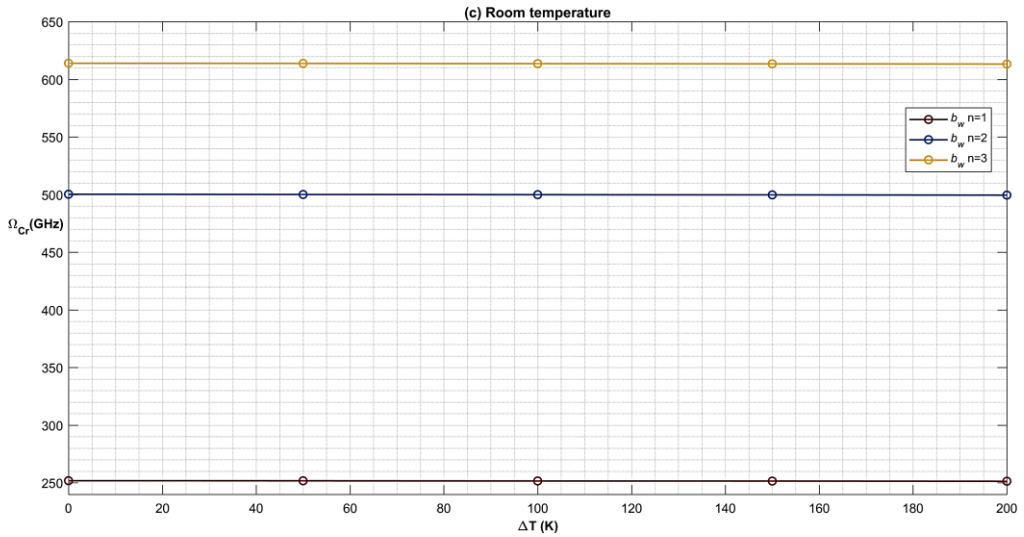
(c) Room temperature
Ω_{Cr}(GHz)
ΔT (K)
b_w n=1
b_w n=2
b_w n=3

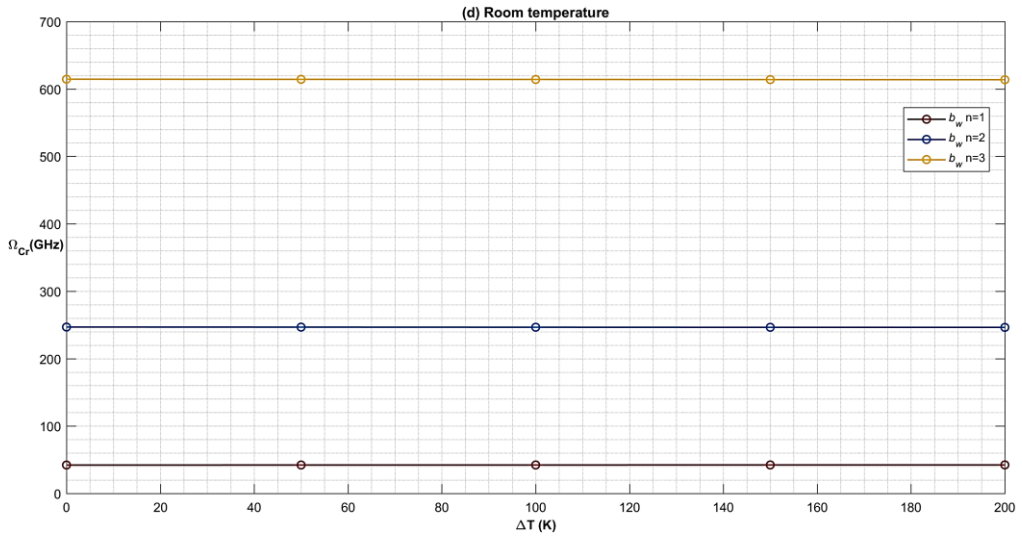

Figure 5.4: Effect of the temperature change on first-third backward critical speed across different boundary conditions and under a room temperature condition: (a) S-S, (b) C-S, (c) C-C, (b) C-F ($\frac{L}{D} = 15,\ \eta = 1.3nm, l = 0.4nm,\ V_0 = 0$)

These results indicate that Single-Walled Boron Nitride Nanotubes (SWBNNTs) possess remarkable thermal resistance. Consequently, their potential application in high-temperature environments, particularly as components in motors or rotors, is highly promising. The consistent performance of SWBNNTs under varying thermal conditions suggests they could be invaluable in engineering applications where thermal stability is crucial.

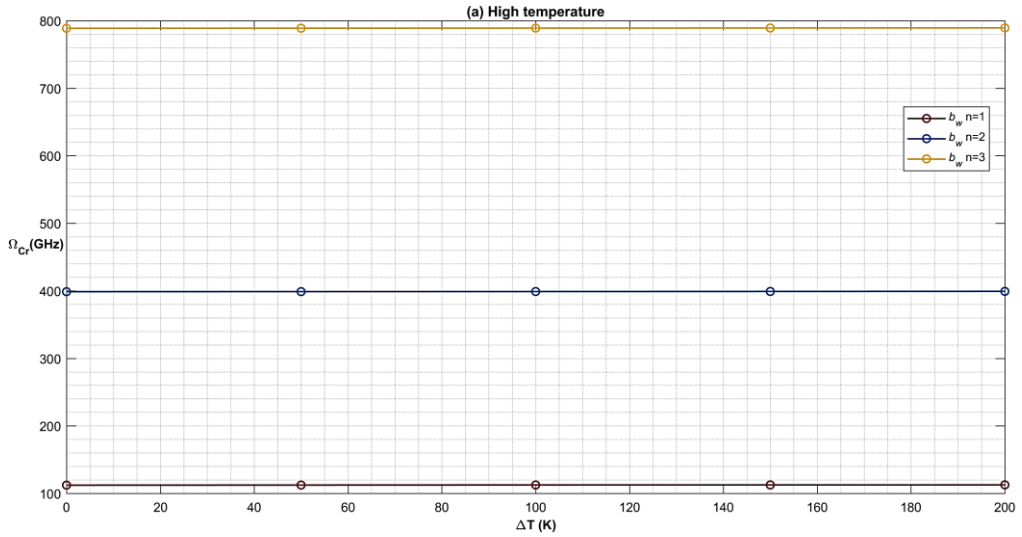

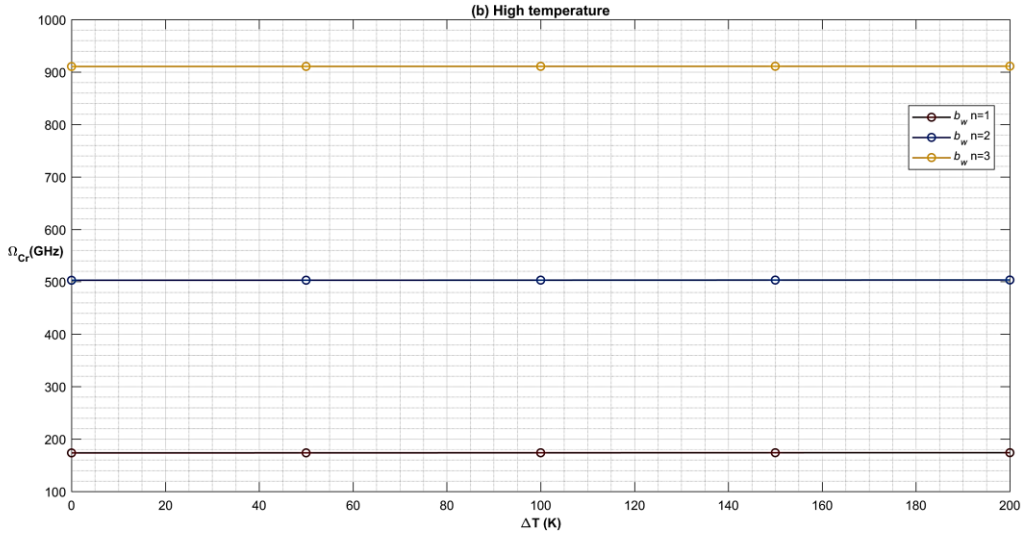
(b) High temperature
Ω_{Cr}(GHz)
ΔT (K)
b_w n=1
b_w n=2
b_w n=3

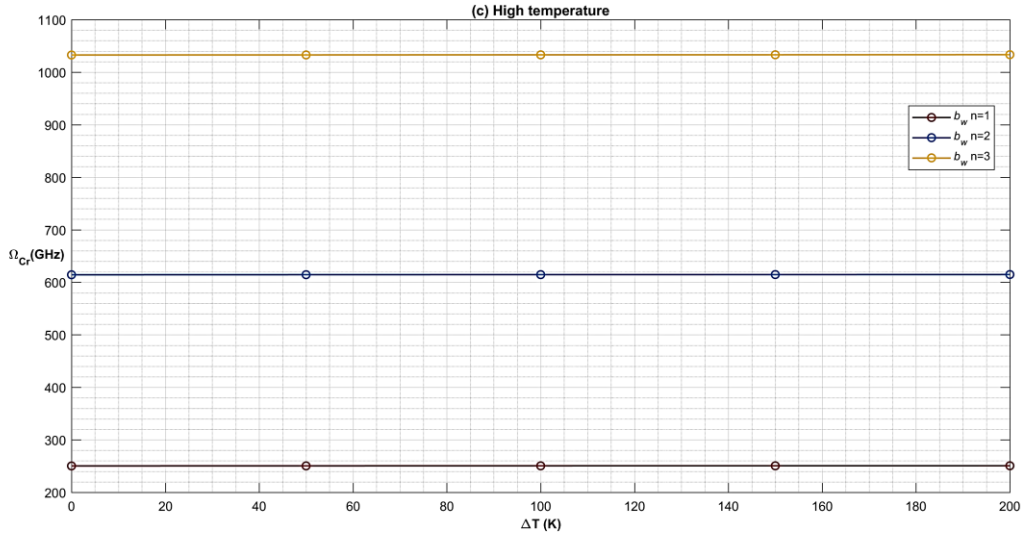
(c) High temperature
Ω_{Cr}(GHz)
ΔT (K)
b_w n=1
b_w n=2
b_w n=3

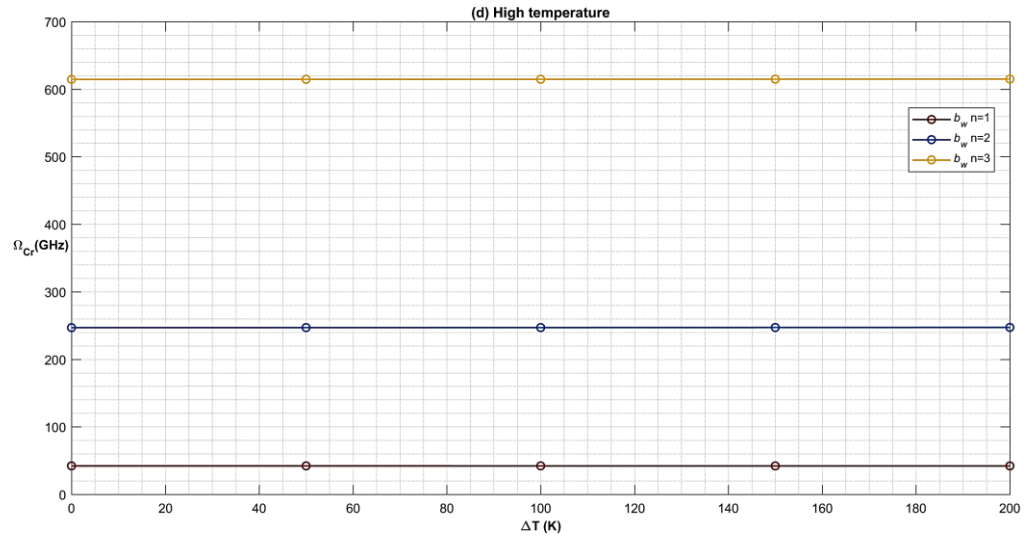
(d) High temperature
Ω_{Cr}(GHz)
ΔT (K)
b_w n=1
b_w n=2
b_w n=3

Figure 5.5: Effect of the temperature change on first-third backward critical speed across different boundary conditions and under a room temperature condition: The effect of the temperature change on first-third backward critical speed across different boundary conditions and under a room temperature condition: (a) S-S, (b) C-S, (c) C-C, (b) C-F ($\frac{L}{D} = 15,\ \eta = 1.3nm, l = 0.4nm,\ V_0 = 0$)

5.3.3 The effect of thickness changes

The thickness value of SWNTs varies depending on the theoretical approach used. Some researchers consider the thickness of SWNTs to be equivalent to the spacing between hexagonal boron nitride (h-BN) layers, which is approximately 0.33 nm. This section analyzes the effect of thickness changes on the critical speed and stability dynamics of the smart nanoshaft.

Table 5.1 illustrates the system's critical speed variation for two thickness values (0.0906 nm and 0.33 nm) and various small-scale parameters under different boundary conditions. The data indicates that reducing the thickness from 0.33 nm to 0.0906 nm decreases the system's critical speed, consequently diminishing its stability dynamics. Notably, this change in thickness does not alter the influence of size-dependent parameters. Moreover, for the clamped-free (C-F) boundary condition, small-scale parameters have a lesser effect on critical speed compared to other boundary conditions.

Figure 5.2: The effects of the thickness change and two small-scale parameters on the backward critical speed (GHz), encompassing all boundary condition combinations

BCs	$\mu(nm)$	$h = 0.33\ nm$				$h = 0.0906\ nm$			
		$l(nm)$							
		0.5	1	1.5	2	0.5	1	1.5	2
S-S	0.5	125.65	128.61	133.40	139.83	117.44	120.21	124.68	130.69
	1	122.83	125.72	130.40	136.69	114.79	117.50	121.87	127.74
	1.5	118.52	121.31	125.83	131.89	110.75	113.36	117.58	123.25
	2	113.18	115.85	120.16	125.95	105.75	108.24	112.27	117.68
C-S	0.5	196.12	201.49	210.13	221.66	183.32	188.34	196.42	207.19
	1	191.10	196.33	204.75	215.98	178.61	183.49	191.36	201.86
	1.5	183.52	188.55	196.63	207.42	171.49	176.18	183.74	193.82
	2	174.29	179.06	186.74	196.98	162.82	167.28	174.45	184.03
C-C	0.5	282.82	269.63	251.23	230.84	264.57	252.15	234.85	215.69
	1	297.43	283.56	264.21	242.76	278.24	265.17	246.98	226.83
	1.5	320.29	305.36	284.52	261.42	299.63	285.56	265.96	244.26
	2	349.81	333.49	310.74	285.51	285.51	311.87	290.47	266.71
C-F	0.5	45.013	44.918	44.759	44.536	42.041	41.953	41.804	41.596
	1	45.106	45.011	44.852	44.628	42.129	42.040	41.891	41.682
	1.5	45.263	45.168	44.008	44.783	42.276	42.187	42.037	41.827
	2	45.486	45.390	45.229	45.074	42.484	42.394	42.244	42.034

Table 5.2 examines the impact of thickness change on the piezoelectric effect. It presents the variation in critical speed for the two thickness values (0.0906 nm and 0.33 nm) at various applied external voltages and mode numbers under all boundary conditions. The results show that reducing the thickness from 0.33 nm to 0.0906 nm amplifies the effect of external voltage on critical speed, indicating that the piezoelectric effect is influenced by thickness

reduction. This underscores the importance of selecting an optimal thickness value for SWNTs with piezoelectric properties.

Interestingly, for the C-F boundary condition, an increase in applied external voltage leads to an increase in the first critical voltage. However, this effect is reversed for the second and third modes.

Figure 5.3: The effect of applied external voltage, thickness change, and mode numbers on backward critical (GHz) speed for all combinations of boundary conditions.

BCs		$h = 0.33nm$			$h = 0.0906$		
		$V_0(Volt)$					
	n	-0.5	0	0.5	-0.5	0	0.5
S-S	1	123.84	120.05	116.13	126.34	112.18	95.961
	2	430.58	426.30	421.98	415.08	398.63	381.46
	3	849.38	844.42	839.42	807.85	788.66	769.00
C-S	1	189.32	186.18	183.00	185.91	173.99	161.19
	2	539.39	535.22	531.03	516.32	500.28	483.69
	3	976.86	971.84	966.79	928.02	908.56	888.68
C-C	1	272.29	269.57	266.81	262.34	251.87	240.95
	2	661.41	657.23	653.02	630.08	613.93	597.34
	3	1108.3	1146.7	1098.0	1052.7	1032.7	1012.4
C-F	1	44.435	45.204	45.960	39.134	42.220	45.097
	2	267.06	264.18	261.28	257.90	246.86	235.31
	3	662.01	657.83	653.63	630.62	614.49	597.92

5.3.4 The Slenderness ration effect

This section investigates the effect of the length-to-diameter ratio on the first through third critical speeds and the system's stability dynamics. **Figure** 5.5 demonstrates that an increase in the length-to-diameter ratio decreases the critical speed, reducing the stability dynamics of the smart nanoshaft. This trend is observed across all boundary conditions and for different mode numbers. From these results, it can be concluded that shorter nanoshafts exhibit greater stability compared to longer nanoshafts.

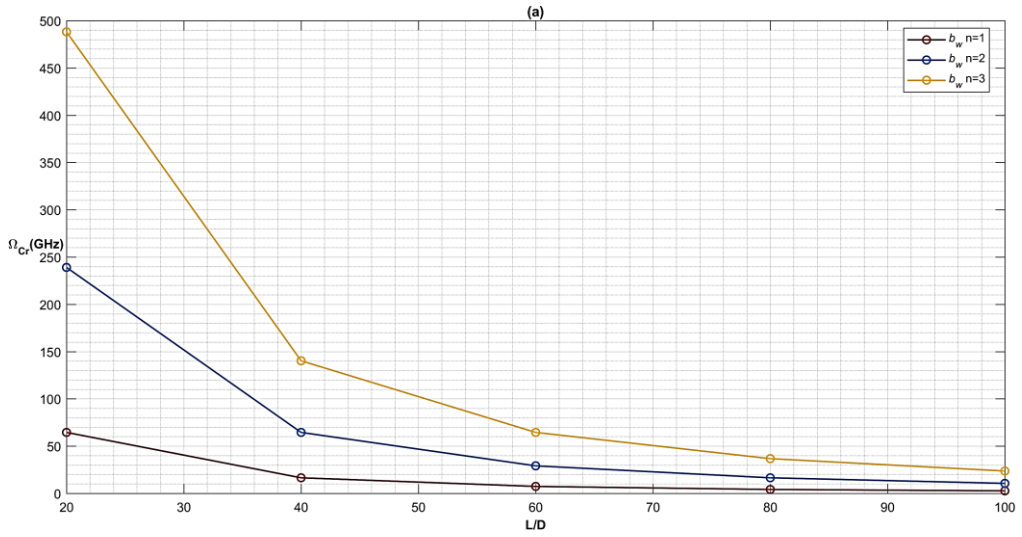

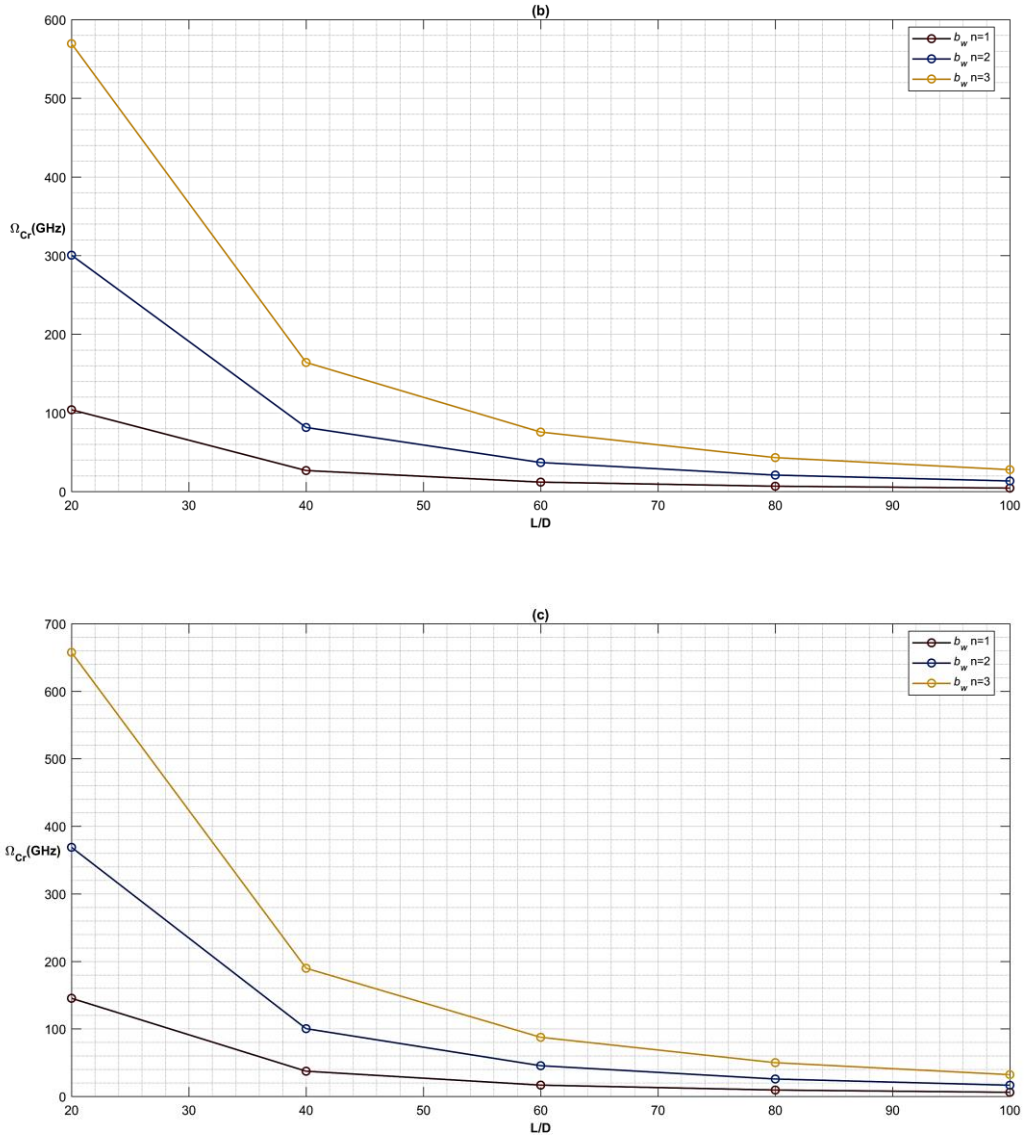

Figure 5.6: The effect of the length-to-diameter ratio on backward critical speed for all combinations of boundary conditions: (a) S-S, (b) C-S, (c) C-C, (b) C-F ($\eta = 1.3nm, l = 0.4nm,\ V_0 = 0, \Delta T = 0$).

5.3.5 The small-scale piezoelectric effect

SWBNNTs are piezoelectric nanotubes, necessitating an investigation into the small-scale piezoelectric effect in smart nanoshafts composed of this material. This section presents the findings of this investigation.

Figure 5.7 illustrates the coupling effect between applied external voltage (both positive and negative) and small-scale parameters under various boundary conditions. Specifically, positive voltage is coupled with the nonlocal parameter, while negative voltage is coupled with the strain gradient parameter.

Under simply supported (S-S) boundary conditions, as shown in **Figure** 5.7(a), increasing positive electrical voltage amplifies the influence of nonlocal parameters on the critical speed of backward whirling (b_w), and vice versa.

For clamped-simply supported (C-S) and clamped-clamped (C-C) boundary conditions (**Figures** 5.7(b-c)), the nonlocal parameter does not affect the critical speed when no external voltage is applied. However, upon application of external voltage, increasing nonlocal parameters decreases the critical speed. Additionally, increasing the positive external voltage reduces the critical speed, with nonlocal parameters enhancing this effect.

In the clamped-free (C-F) boundary condition, increasing the nonlocal parameter decreases the critical speed. When the nonlocal parameter is zero, increasing positive external voltage initially raises the critical speed. However, as the nonlocal parameter increases, this trend reverses, leading to a decrease in critical speed.

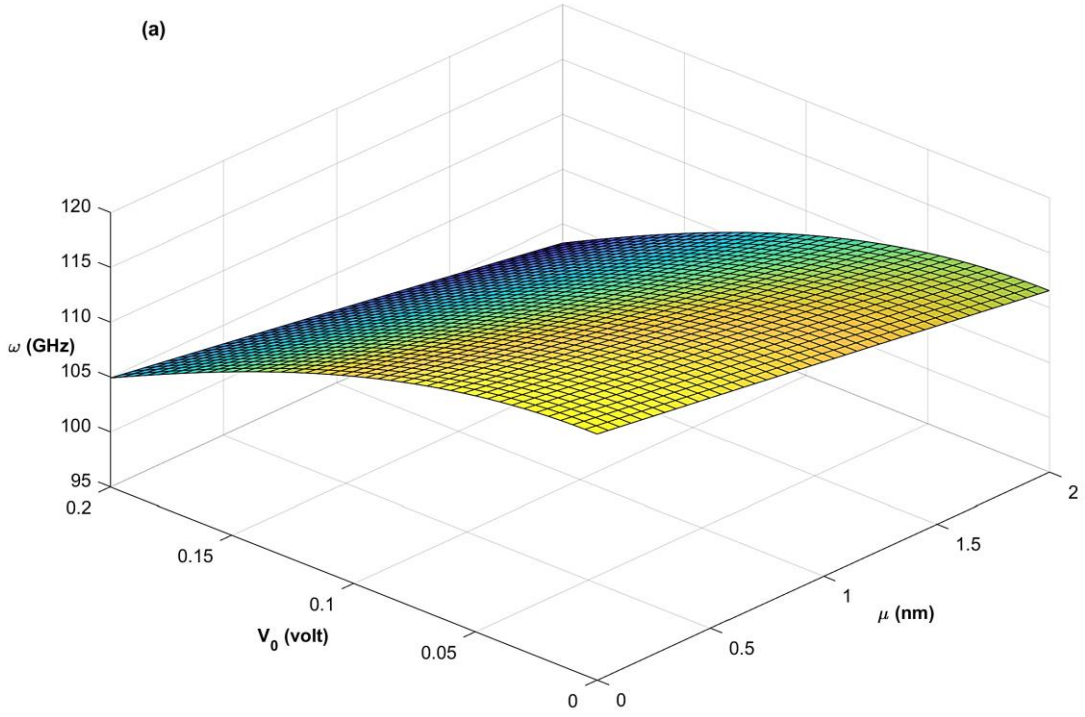

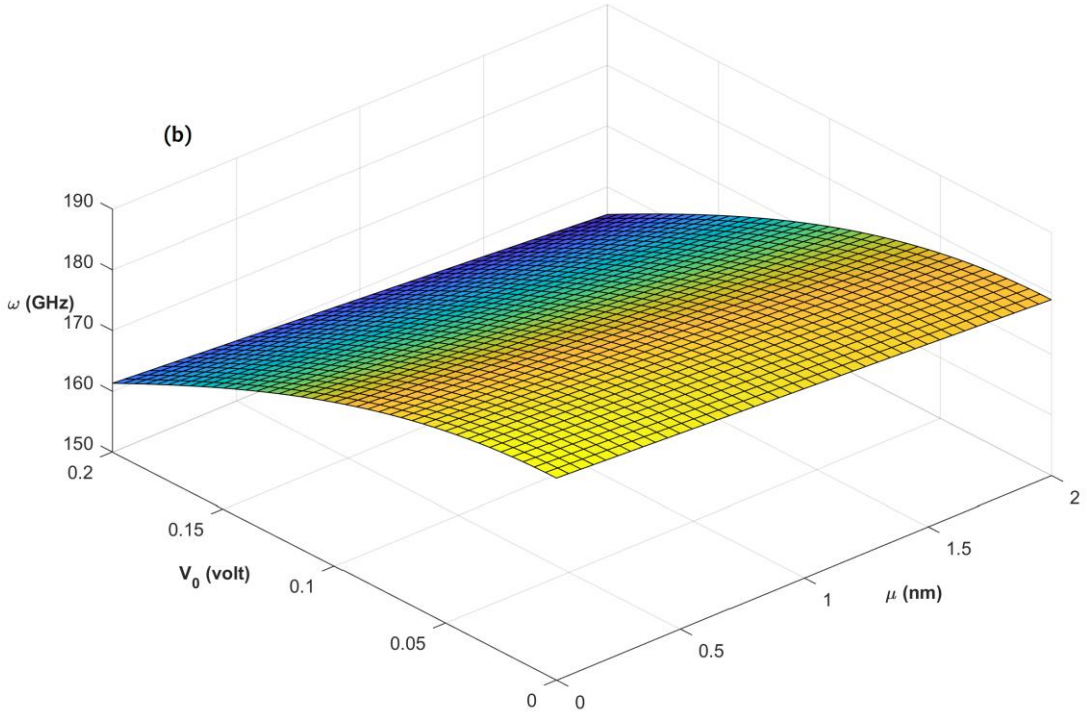
(b)
190
180
ω (GHz)
170
160
150
0.2
0.15
V0 (volt)
0.1
0.05
0
0
0.5
1
μ (nm)
1.5
2

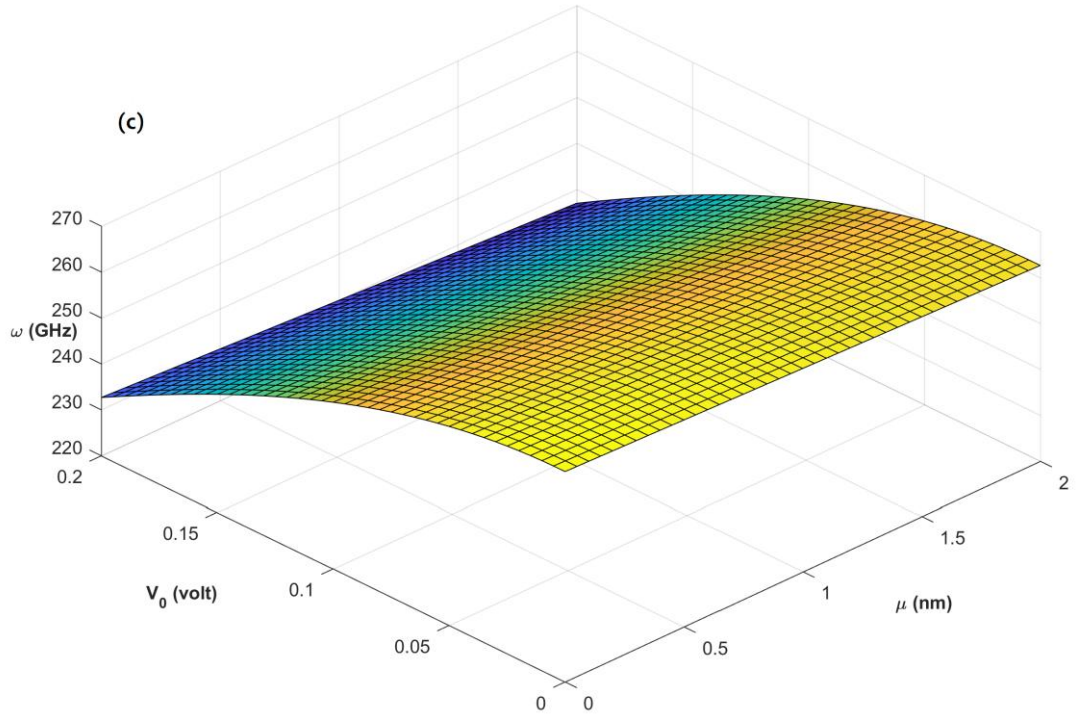
(c)
270
260
250
ω (GHz)
240
230
220
0.2
0.15
V0 (volt)
0.1
0.05
0
0
0.5
1
μ (nm)
1.5
2

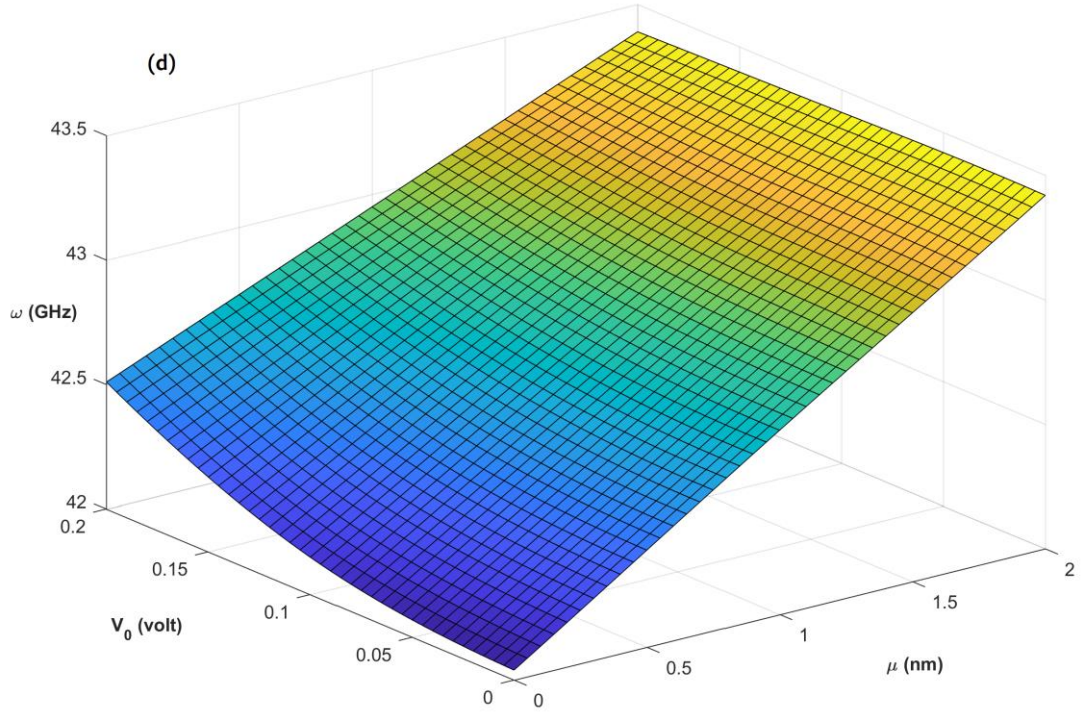

Figure 5.7: Effects of external electrical voltage and nonlocal parameters on backward critical speed for all combinations of the boundary conditions: : (a) S − S, (b) C − S, (c) C − C, (b) C − F $(\frac{L}{D} = 15,\ l = 1.3nm, \Delta \mathrm{T} = 0\ )$

Figure 5.8 illustrates the combined effect of applied negative external voltage and strain gradient parameters on the critical speed across various boundary conditions. For simply supported-simply supported (S-S) and clamped-simply supported (C-S) boundary conditions (see **Figures** 5.8(a-b)), increasing both the negative voltage and strain gradient parameter leads to higher critical speeds.

In the clamped-clamped (C-C) condition, the strain gradient term increases the critical speed, but at a lower rate compared to S-S and C-S conditions. The negative applied voltage also increases the critical speed in this case.

For the clamped-free (C-F) boundary condition, an increase in the strain gradient term decreases the critical speed. When the strain gradient term is zero, the applied negative voltage does not affect the critical speed. However, as the strain gradient term increases, higher negative applied external voltage results in increased critical speed.

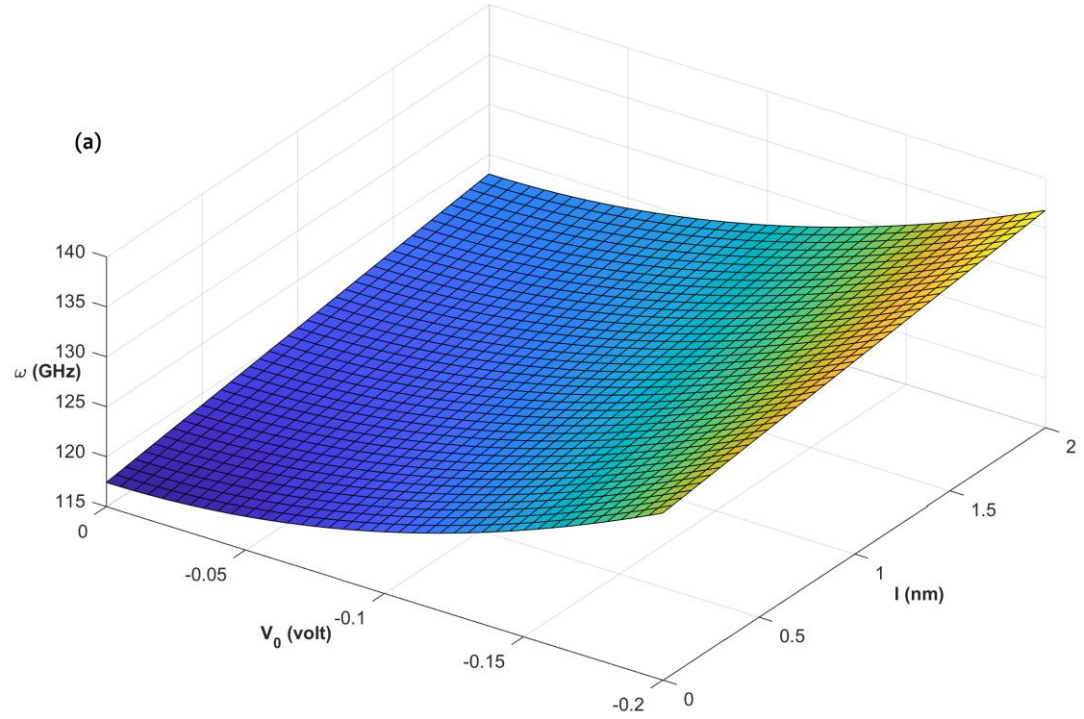
(a)
140
135
130
125
120
115
ω (GHz)
0
-0.05
-0.1
-0.15
-0.2
V0 (volt)
0
0.5
1
1.5
2
l (nm)

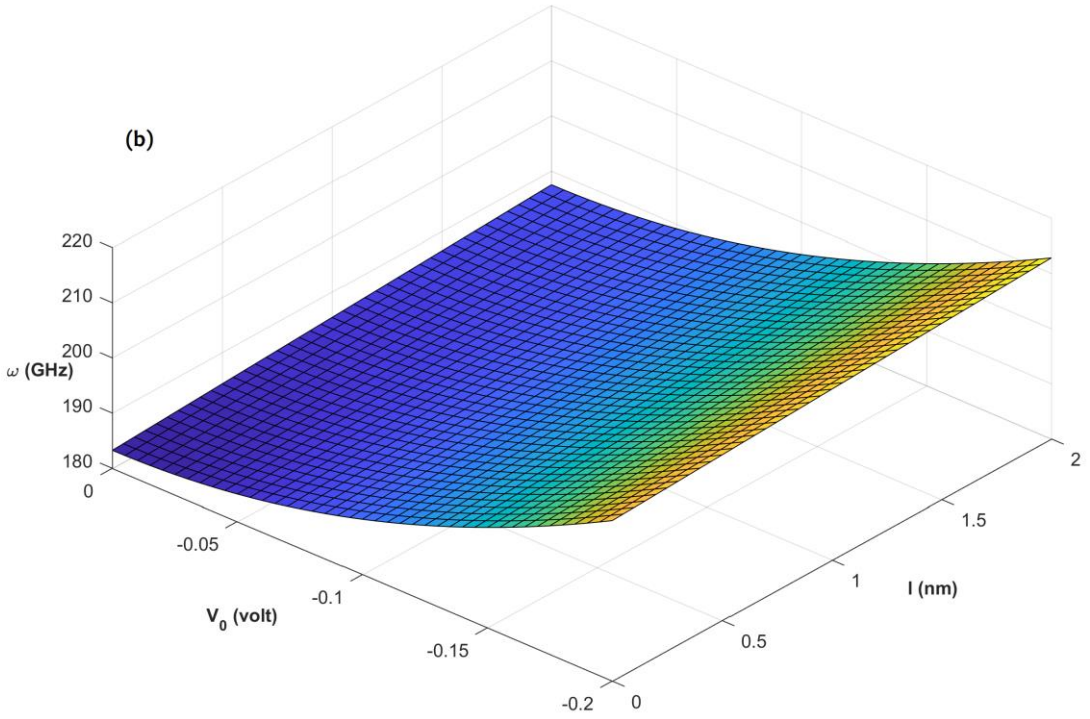
(b)
220
210
200
190
180
ω (GHz)
0
-0.05
-0.1
-0.15
-0.2
V0 (volt)
0
0.5
1
1.5
2
l (nm)

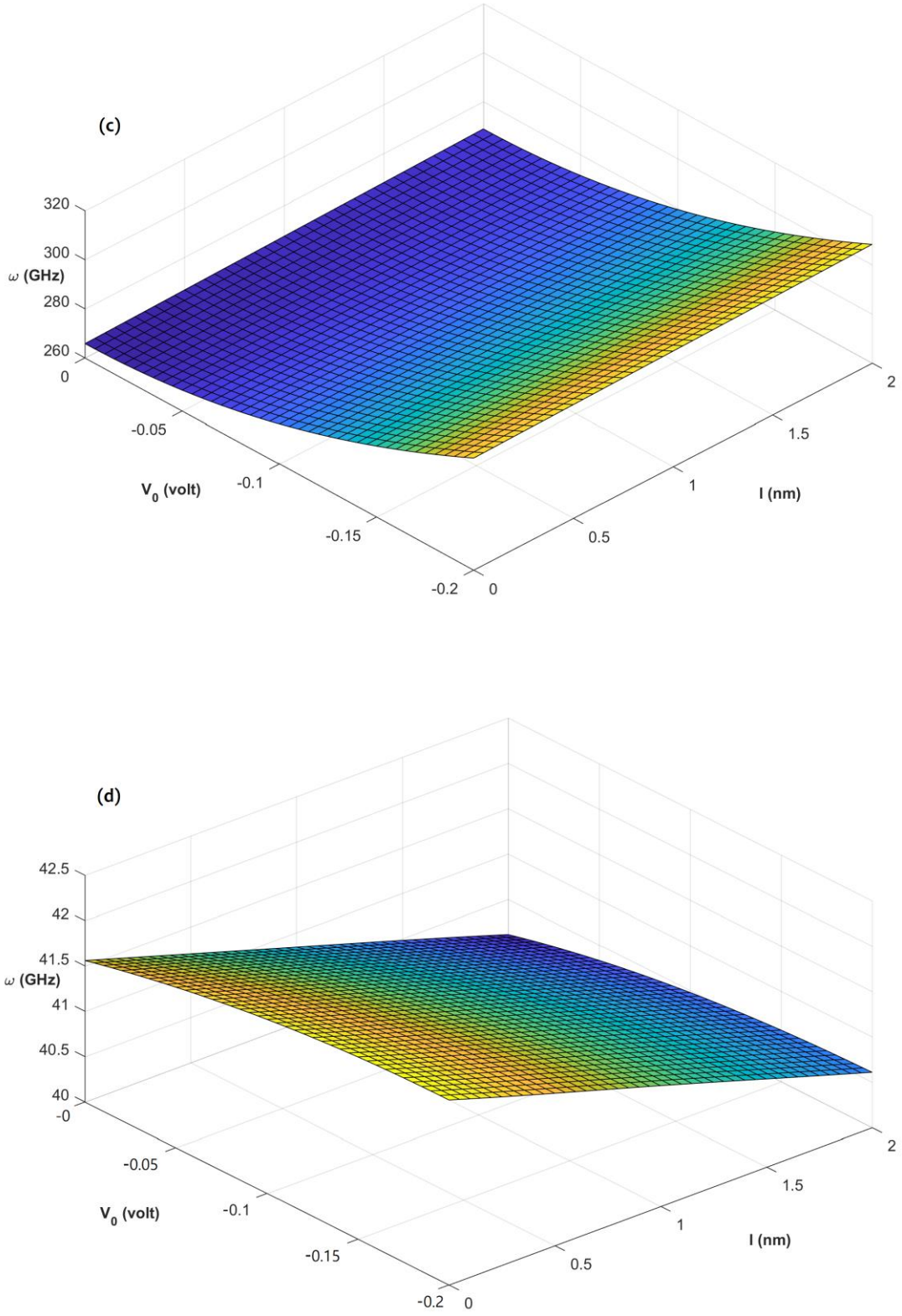

Figure 5.8: The effects of external electrical voltage and material length scale term on backward critical speed for all combinations of the boundary conditions: : (a) S − S, (b) C − S, (c) C − C, (b) C − F ($\frac{L}{D} = 15,\ l = 1.3nm, \Delta \mathrm{T} = 0$)

In conclusion, coupling the nanolocal parameter with positive external voltage demonstrates a stiffness-softening effect on the critical speed, leading to lower stability dynamics. Conversely, coupling the strain gradient parameter with negative external voltage exhibits a stiffness-hardening effect, resulting in higher stability dynamics. In the C-F boundary condition, small-scale parameters show the opposite effect and the applied external voltage loses its impact.

5.4 Summary

In this chapter, we analyzed the stability dynamics of smart nanoshafts under thermo-electrical loading. The resonance critical speed was determined by substituting the natural frequency for the rotating speed in the final equation of motion. Our findings were thoroughly validated through comparison with existing literature.

Significantly, we found that initial hoop tension does not influence the system's critical speed, as this speed occurs at low frequency and approximates the natural frequency in static conditions. Additionally, temperature variations, whether at room or elevated temperatures, showed no impact on the system's critical speed, demonstrating the high temperature resistance of SWBNNT-based smart nanoshafts.

Our analysis revealed that increasing nonlocal parameters and positive external voltage reduces critical speed, thereby decreasing the system's stability dynamics. Conversely, increasing the material length scale and negative external voltage enhances critical speed, improving stability dynamics. These findings suggest that the coupled effect of external voltage and small scale parameters can be used to modulate critical speed and optimize system stability.

Furthermore, reducing the thickness of the smart nanoshaft amplifies the effect of external voltage on critical speed, identifying thickness as a crucial parameter in piezoelectric nanotubes. Finally, we observed that longer smart nanoshafts exhibit lower stability compared to shorter ones.

Chapter 6

Conclusions and Future Research Perspectives

In this study, the thermo-electro-mechanical vibration response and stability analysis of a smart rotating nanoshaft are investigated based on piezoelectric nonlocal strain gradient theory. Euler-Bernoulli beam theory and Maxwell's electrostatic equations are used to model the system. Hamilton's principle is employed to formulate the equations of motion and boundary conditions, which are then solved semi-analytically using the Galerkin technique. Appropriate functions for electric potential distribution in transverse and lateral directions are chosen to satisfy Maxwell's equations. Through parametric studies concerning thermo-electro-mechanical and stability analysis of smart nanoshafts, our study has obtained well-defined results in each chapter. This approach has enabled us to draw important conclusions regarding our modeling techniques, their implementation, and the results of parametric studies. These conclusions, shaped by the applied method and application problems explored in previous chapters, form the foundation of our research.

6.1 Conclusions

1. **Validation of Theoretical Frameworks:** Our study has successfully validated the combined use of Euler-Bernoulli beam theory and piezoelectric nonlocal strain gradient theory in the rotation model. When applied to a rotating system, these theories demonstrated their accuracy and reliability in capturing the system's electromechanical behavior.

2. **Effects of Rotation Speed and Precession Frequencies:** The rotation speed creates two distinct precession frequencies, each exerting different effects. The softening effect was observed in backward whirl, while the stiffening effect was observed in forward whirl.

3. **Effect of Small Scale Parameters:** The strain gradient term shows a stiffness-hardening effect, resulting in higher frequencies and critical speeds, while the nonlocal parameter demonstrates a stiffness-softening effect, causing lower frequencies and critical speeds.

4. **Effect of External Voltage Application:** Negative voltage increases the critical speed, thus improving stability, while positive external voltage decreases it.

5. **Effect of Temperature Change:** Temperature variation does not affect the critical speed or stability dynamics of the smart nanoshaft, whether at room or high temperature. This demonstrates that the smart nanoshaft manufactured from single-walled boron nitride nanotube (SWBNNT) possesses excellent thermal resistance.
6. **Effect of Thickness Change:** Reducing the nanotube thickness does not affect the impact of size-dependent parameters; instead, it amplifies the influence of external electric voltage on the system's critical speed.
7. **Specific Observations for the Cantilever Case:** In the cantilever case, external voltage has opposing effects. The nonlocal parameter initially increases the critical speed without external voltage but decreases it when voltage is applied. Additionally, the strain gradient term remains unaffected.

This research represents a significant advancement in mechanical engineering, particularly in the field of rotating nanoelectromechanical systems (NEMS). While previous studies have investigated the vibration characteristics of smart piezoelectric nanobeams with single-direction polarization, our work introduces a novel approach by incorporating dual perpendicular polarizations in piezoelectric nanotubes under rotation. We have developed an innovative mathematical framework that accounts for this dual polarization phenomenon, including a modified electrical potential distribution function to accurately model these interactions.

Our study presents several groundbreaking contributions to the literature. First, we introduce a comprehensive mathematical formulation for rotating smart nanotubes that accounts for complex electromechanical interactions. Second, our investigation reveals unique behavioral patterns under cantilever boundary conditions, offering valuable insights for future research directions. Most notably, this work represents the first application of nonlocal strain gradient piezoelectric theory to rotating nanoshafts, establishing a foundational framework for designing and analyzing rotating nanostructures.

These findings significantly advance our understanding of nanomechanics and provide essential reference data for future developments in nanoengineering applications. The theoretical framework developed in this study serves as a valuable tool for predicting and optimizing the performance of rotating nanostructures in various technological applications.

6.2 Research Limitations and Future Perspectives

This research encountered inherent limitations in analyzing rotational vibration behavior of smart nanoshafts through nonlocal strain gradient theory. The most significant limitation stems from insufficient experimental validation, making direct real-world applications challenging. Although our theoretical framework provides substantial insights, experimental validation remains crucial for confirming our theoretical predictions.

Our modeling approach necessitated certain simplifications, particularly in adopting cosine functions for electrical potential and assuming linear displacement fields in smart nanoshafts. While these assumptions facilitated computational analysis, they may not capture

all physical complexities present in actual systems. Future studies should address these limitations by:

- Incorporating nonlinear behavior
- Implementing more sophisticated electrical potential distribution models
- Considering advanced multiphysics coupling effects

Another significant challenge involves the uncertainty in material properties of smart nanostructures, including piezomagnetic, ferromagnetic, and ferroelectric materials. This uncertainty necessitates careful interpretation of numerical results. To enhance future research reliability, we recommend:

- Establishing interdisciplinary collaborations with materials scientists
- Developing comprehensive material property databases
- Implementing advanced material characterization techniques

Overcoming these limitations will require substantial experimental and theoretical advancements. Future research efforts should focus on bridging the gap between theoretical predictions and experimental observations, ultimately enhancing the practical applicability of our theoretical framework for designing and optimizing smart nanostructures.

Based on our findings, we propose the following key directions for future research

- ✓ **Piezomagnetic Analysis:** Given the substantial impact of piezomagnetic properties on smart nanostructures, future investigations should incorporate these effects into comprehensive dynamic analyses to enhance model accuracy and predictive capabilities.
- ✓ **Size-Dependent Timoshenko Beam Analysis:** Research indicates that coupling size-dependent parameters with the Timoshenko beam theory yields results that align more closely with molecular dynamics simulations than alternative beam models, including Euler-Bernoulli and Reddy formulations. Therefore, future investigations should prioritize the adoption of size-dependent Timoshenko beam theory to achieve more accurate predictions of nanoscale mechanical behavior.
- ✓ **Advanced Electrical Potential Function Modeling:** Future research should explore nonlinear and exponential electrical potential functions to enhance the accuracy of electromechanical coupling analysis in smart materials. Moving beyond current linear approximations to more sophisticated mathematical representations would enable more precise characterization of the complex interactions between electrical and mechanical properties in smart nanostructures.
- ✓ **Exploring shell theories:** Employing shell theories, such as Donnell's, Love's, and shear deformation models, in place of beam models, allows for more accurate nanotube

modeling, leading to more precise results and better capturing the circumferential vibration mode in these nanostructures.

- ✓ **utilization of the molecular dynamics simulation:** Employing molecular dynamics simulation to capture the piezoelectric response of smart nanostructures is crucial. This investigation aids in calibrating the size-dependent parameters of the material and enhances the mathematical formulation for electro-mechanical interactions within it.

Our investigation into the piezoelectric vibrational dynamics of rotating smart nanoshafts, grounded in the robust framework of nonlocal strain gradient theory, represents a dedicated effort to unravel their complexities. While our contribution is a modest addition to the broader body of scientific knowledge, it holds the potential to spark future advancements, igniting the curiosity of fellow researchers and opening doors to deeper exploration within mechanical engineering. We conclude with deep appreciation for the unwavering support of our mentors, colleagues, and the scientific community. Though this study reaches its end, it serves as a foundation for future scholarship—a guiding light for generations of researchers, and a reminder of the limitless nature of scientific inquiry

Referrences

[1] N. A. Sakharova, A. F. G. Pereira, J. M. Antunes, B. M. Chaparro, and T. G. Parreira, "On the determination of elastic properties of single-walled nitride nanotubes using numerical simulation On the Determination of Elastic Properties of Single- Walled Nitride Nanotubes Using Numerical Simulation," 2024, doi: 10.20944/preprints202404.0629.v1.

[2] E. Ta, "Molecular Mechanics and Molecular Dynamics Simulations of Carbon Based Nanogears," vol. 6, no. 4, pp. 921–925, 2009, doi: 10.1166/jctn.2009.1126.

[3] S. Negi, M. Warrier, S. Chaturvedi, and K. Nordlund, "Molecular Dynamic simulations of a double-walled carbon nanotube motor subjected to a sinusoidally varying electric field," *Comput. Mater. Sci.*, vol. 44, no. 3, pp. 979–987, 2009, doi: https://doi.org/10.1016/j.commatsci.2008.07.003.

[4] P. Zheng, W. G. Jiang, Y. W. Lin, Y. J. Chen, Q. H. Qin, and D. S. Li, "A novel rotation transmission nano-system based on Carbon@Boron-Nitride@Carbon heterogeneous nanotubes: A molecular dynamics study," *Comput. Mater. Sci.*, vol. 196, no. January, p. 110517, 2021, doi: 10.1016/j.commatsci.2021.110517.

[5] P. Zheng, W. Jiang, Q. Qin, and D. Li, "Dynamic behavior of rotation transmission nano-system in helium environment: A molecular dynamics study," *Molecules*, vol. 26, no. 17, 2021, doi: 10.3390/molecules26175199.

[6] A. Arnau and D. Soares, *1 Fundamentals of Piezoelectricity*. 2008. doi: 10.1007/978-3-540-77508-9.

[7] S. Materials, M. Santhya, A. R. Upadhya, N. K. P, and S. M. Kulkarni, "Recent trends in piezoelectric actuators for precision motion and their applications : a review Recent trends in piezoelectric actuators for precision motion and their applications : a review," no. June 2022, 2020, doi: 10.1088/1361-665X/abc6b9.

[8] A. Jafari, A. A. Khatibi, and M. M. Mashhadi, "Evaluation of Mechanical and Piezoelectric Properties of Boron Nitride Nanotube : A Novel Electrostructural Analogy Approach Delivered by Ingenta to :," vol. 9, no. 3, pp. 461–468, 2012, doi: 10.1166/jctn.2012.2047.

[9] M. C. S. Mohammed, "Vibration Analysis of Rotating Functionally Graded Nanoshafts".

[10] R. Bogue, "Smart materials : a review of capabilities and applications," vol. 1, pp. 16–22, 2014, doi: 10.1108/AA-10-2013-094.

[11] L. Cheng and J. Li, "A review on one dimensional perovskite nanocrystals for piezoelectric applications," *J. Mater.*, 2016, doi: 10.1016/j.jmat.2016.02.003.

[12] X. Cheng, P. K. Singh, A. Mishra, A. Tiwari, and W. Ren, "Wurtzite nanostructured piezoelectric devices," *Mater. Today Sustain.*, vol. 23, p. 100474, 2023, https://doi.org/10.1016/j.mtsust.2023.100474

[13] G. Gautschi and G. Gautschi, *Piezoelectric sensors*. Springer, 2002, https://doi.org/10.1007/978-3-662-04732-3_5

[14] H. Jin *et al.*, "Review on piezoelectric actuators based on high-performance piezoelectric materials," *IEEE Trans. Ultrason. Ferroelectr. Freq. Control*, vol. 69, no. 11, pp. 3057–3069, 2022, DOI: 10.1109/TUFFC.2022.3175853.

[15] T. R. Shrout, “Innovations in Piezoelectric Materials for Ultrasound Transducers,” pp. 3–6, DOI: 10.1109/ISAF.2008.4693822.

[16] M. Safaei and H. A. Sodano, “A review of energy harvesting using piezoelectric materials : state-of-the-art a decade later (2008 – 2018),” 2018, DOI 10.1088/1361-665X/ab36e4

[17] B. C. Sekhar *et al.*, “Piezoelectricity and its applications,” *Multifunct. Ferroelectr. Mater.*, vol. 11, p. 13, 2021, DOI: 10.5772/intechopen.96154

[18] P. Kohli and C. R. Martin, “Smart nanotubes for biotechnology,” *Curr. Pharm. Biotechnol.*, vol. 6, no. 1, pp. 35–47, 2005, https://doi.org/10.2174/1389201053167211.

[19] D. Tan, M. Willatzen, and Z. L. Wang, “Out-of-Plane Polarization in Bent Graphene-Like Zinc Oxide and Nanogenerator Applications,” *Adv. Funct. Mater.*, vol. 30, no. 5, pp. 1–8, 2020, doi: 10.1002/adfm.201907885.

[20] H. Guo, T. Yang, X. Xuan, Z. Zhang, and W. Guo, “Flexoelectricity in hexagonal boron nitride monolayers,” *Extrem. Mech. Lett.*, vol. 52, p. 101669, 2022, https://doi.org/10.1016/j.eml.2022.101669.

[21] H. D. Espinosa, R. A. Bernal, and M. Minary-Jolandan, “A review of mechanical and electromechanical properties of piezoelectric nanowires,” *Adv. Mater.*, vol. 24, no. 34, pp. 4656–4675, 2012, https://doi.org/10.1002/adma.201104810.

[22] W. S. Su, Y. F. Chen, C. L. Hsiao, and L. W. Tu, “Generation of electricity in GaN nanorods induced by piezoelectric effect,” *Appl. Phys. Lett.*, vol. 90, no. 6, 2007, https://doi.org/10.1063/1.2472539.

[23] B. Y. N. W. Thomas, “Crystal Structure-Physical Property Relationships in Perovskites,” pp. 337–344, 1989, doi: 10.1107/S0108768189003721.

[24] N. L. Marana, A. R. Albuquerque, F. A. La Porta, E. Longo, and J. R. Sambrano, “Periodic density functional theory study of structural and electronic properties of single-walled zinc oxide and carbon nanotubes,” *J. Solid State Chem.*, vol. 237, pp. 36–47, 2016, doi: 10.1016/j.jssc.2016.01.017.

[25] Y. Jeng, P. Tsai, and T. Fang, “Molecular dynamics investigation of the mechanical properties of gallium nitride nanotubes under tension and fatigue,” vol. 15, pp. 1737–1744, 2004, doi: 10.1088/0957-4484/15/12/006.

[26] Z. Wang, X. Zu, F. Gao, and W. J. Weber, “Mechanical behavior of gallium nitride nanotubes under combined tension-torsion: An atomistic simulation,” *J. Appl. Phys.*, vol. 103, no. 1, 2008, https://doi.org/10.1063/1.2828169

[27] S.-C. Hung, Y.-K. Su, T.-H. Fang, and T.-C. Liang, “Elastic modulus investigation of gallium nitride nanotubes,” in *2006 1st IEEE International Conference on Nano/Micro Engineered and Molecular Systems*, IEEE, 2006, pp. 1400–1403, DOI: 10.1109/NEMS.2006.334775.

[28] M. Zheng *et al.*, “Radial Mechanical Properties of Single-Walled Boron Nitride Nanotubes,” no. 1, pp. 116–121, 2012, doi: 10.1002/smll.201100946.

[29] X. Chen, C. M. Dmuchowski, C. Park, and C. C. Fay, “Quantitative Characterization of Structural and Mechanical Properties of Boron Nitride Nanotubes in High Temperature Environments,” *Sci. Rep.*, no. July, pp. 1–9, 2017, doi: 10.1038/s41598-017-11795-9.

[30] V. Verma, V. K. Jindal, and K. Dharamvir, “Elastic moduli of a boron nitride nanotube,”

Nanotechnology, vol. 18, no. 43, p. 435711, 2007, doi: 10.1088/0957-4484/18/43/435711.

[31] I. K. Petrushenko and K. B. Petrushenko, "Mechanical properties of carbon , silicon carbide , and boron nitride nanotubes : effect of ionization," 2015, doi: 10.1007/s00706-015-1537-1.

[32] M. Mirnezhad, R. Ansari, and H. Rouhi, "Effects of hydrogen adsorption on mechanical properties of chiral single-walled zinc oxide nanotubes," *J. Appl. Phys.*, vol. 111, no. 1, 2012, https://doi.org/10.1063/1.3673867.

[33] A. K. Prajapati, S. Rai, and P. K. Yadawa, "Pressure Dependent Elastic , Mechanical and Ultrasonic Properties of ZnO Nanotube," vol. 61, no. February, pp. 115–123, 2023, doi: 10.56042/ijpap.v61i2.64116.

[34] Y. H. Wen, Y. Zhang, S. Q. Wu, and Z. Z. Zhu, "Size-dependent elastic properties of single-walled ZnO nanotubes: A first-principles study," *J. Appl. Phys.*, vol. 109, no. 8, 2011, doi: 10.1063/1.3573508.

[35] J. Zhang and S. A. Meguid, "On the piezoelectric potential of gallium nitride nanotubes," *Nano Energy*, vol. 12, pp. 322–330, 2015, https://doi.org/10.1016/j.nanoen.2014.12.036.

[36] S. I. Kundalwal and V. Choyal, "Enhancing the piezoelectric properties of boron nitride nanotubes through defect engineering," *Phys. E Low-dimensional Syst. Nanostructures*, vol. 125, p. 114304, 2021, https://doi.org/10.1016/j.physe.2020.114304.

[37] V. Yamakov, C. Park, J. H. Kang, X. Chen, C. Ke, and C. Fay, "Piezoelectric and elastic properties of multiwall boron-nitride nanotubes and their fibers: A molecular dynamics study," *Comput. Mater. Sci.*, vol. 135, pp. 29–42, 2017, doi: https://doi.org/10.1016/j.commatsci.2017.03.050.

[38] M. Salavati, H. Ghasemi, and T. Rabczuk, "Electromechanical properties of Boron Nitride Nanotube: Atomistic bond potential and equivalent mechanical energy approach," *Comput. Mater. Sci.*, vol. 149, pp. 460–465, 2018, doi: https://doi.org/10.1016/j.commatsci.2018.03.037.

[39] A. Jafari, A. A. Khatibi, and M. M. Mashhadi, "Evaluation of mechanical and piezoelectric properties of boron nitride nanotube: a novel electrostructural analogy approach," *J. Comput. Theor. Nanosci.*, vol. 9, no. 3, pp. 461–468, 2012, https://doi.org/10.1166/jctn.2012.2047.

[40] H. J. Xiang, Z. Y. Chen, and J. Yang, "Electronic and piezoelectric properties of BN nanotubes from hybrid density functional method," pp. 1–11, 2019, https://doi.org/10.1166/jctn.2006.025.

[41] J. Zhang, "Elastocaloric effect on the piezoelectric potential of boron nitride nanotubes," *J. Phys. D. Appl. Phys.*, vol. 50, no. 41, p. 415308, 2017, DOI 10.1088/1361-6463/aa839e.

[42] S. M. Nakhmanson, A. Calzolari, V. Meunier, J. Bernholc, and M. B. Nardelli, "Spontaneous polarization and piezoelectricity in boron nitride nanotubes," no. 1, pp. 1–6, 2018, https://doi.org/10.1103/PhysRevB.67.235406.

[43] J. Zhang and S. A. Meguid, "Effect of number of layers upon piezoelectric behaviour of multi-walled boron nitride nanotubes," *J. Phys. D. Appl. Phys.*, vol. 48, no. 49, p. 495301, 2015, DOI 10.1088/0022-3727/48/49/495301.

[44] Z. C. Tu and X. Hu, "Elasticity and piezoelectricity of zinc oxide crystals, single layers, and possible single-walled nanotubes," *Phys. Rev. B*, vol. 74, no. 3, p. 35434, 2006, doi: 10.1103/PhysRevB.74.035434.

[45] H.-P. Lan, L.-H. Ye, S. Zhang, and L.-M. Peng, "Transverse dielectric properties of boron nitride nanotubes by ab initio electric field calculations," *Appl. Phys. Lett.*, vol. 94, no. 18, 2009, https://doi.org/10.1063/1.3129170

[46] S. Yang, "Piezoelectric and dielectric constants of topologically defected boron nitride nanotubes," *Dalt. Trans.*, vol. 52, no. 18, pp. 5895–5908, 2023, doi: 10.1039/D3DT00678F.

[47] V. Lacivita, A. Erba, Y. Noël, R. Orlando, P. D'Arco, and R. Dovesi, "Zinc oxide nanotubes: An ab initio investigation of their structural, vibrational, elastic, and dielectric properties," *J. Chem. Phys.*, vol. 138, no. 21, 2013, doi: 10.1063/1.4808156.

[48] Y. Mao, J. Zhong, and Y. Chen, "First principles study of the band structure and dielectric function of (6,6) single-walled zinc oxide nanotube," *Phys. E Low-dimensional Syst. Nanostructures*, vol. 40, no. 3, pp. 499–502, 2008, doi: https://doi.org/10.1016/j.physe.2007.07.008.

[49] G. Zhou and L. Li, "Phonon thermal conductivity of GaN nanotubes," *J. Appl. Phys.*, vol. 112, no. 1, 2012, https://doi.org/10.1063/1.4736421.

[50] C. W. Chang *et al.*, "Isotope Effect on the Thermal Conductivity of Boron Nitride Nanotubes," *Phys. Rev. Lett.*, vol. 97, no. 8, p. 85901, Aug. 2006, doi: 10.1103/PhysRevLett.97.085901.

[51] J. Huang, Y. Guo, Y. Fan, and Y. Liang, "Molecular dynamics investigation of the thermal properties in single-walled boron nitride nanotube," *Mater. Res. Express*, vol. 7, no. 2, p. 25025, 2020, doi: 10.1088/2053-1591/ab72d1.

[52] D. A. Stewart, I. Savić, and N. Mingo, "First-Principles Calculation of the Isotope Effect on Boron Nitride Nanotube Thermal Conductivity," *Nano Lett.*, vol. 9, no. 1, pp. 81–84, Jan. 2009, doi: 10.1021/nl802503q.

[53] J.-W. Jiang and J.-S. Wang, "Theoretical study of thermal conductivity in single-walled boron nitride nanotubes," *Phys. Rev. B*, vol. 84, no. 8, p. 85439, Aug. 2011, doi: 10.1103/PhysRevB.84.085439.

[54] C.-W. Chang, W.-Q. Han, and A. Zettl, "Thermal conductivity of BCN and BN nanotubes," *J. Vac. Sci. Technol. B Microelectron. Nanom. Struct. Process. Meas. Phenom.*, vol. 23, no. 5, pp. 1883–1886, 2005, https://doi.org/10.1116/1.2008266.

[55] R. E. Tuzun, D. W. Noid, and B. G. Sumpter, "The dynamics of molecular bearings," vol. 64, DOI 10.1088/0957-4484/6/2/005

[56] S. Zhang, W. K. Liu, and R. S. Ruoff, "Atomistic Simulations of Double-Walled Carbon Nanotubes (DWCNTs) as Rotational Bearings," *Nano Lett.*, vol. 4, no. 2, pp. 293–297, Feb. 2004, doi: 10.1021/nl0350276.

[57] B. E. Zhu, Z. Y. Pan, Y. X. Wang, and Y. Xiao, "Thermal effect on DWCNTs as rotational bearings," *Nanotechnology*, vol. 19, no. 49, p. 495708, 2008, doi: 10.1088/0957-4484/19/49/495708.

[58] Z. Huang, "Coaxial stability of nano-bearings constructed by double-walled carbon nanotubes," *Nanotechnology*, vol. 19, no. 4, p. 45701, 2008, doi: 10.1088/0957-

4484/19/04/045701.

[59] Y. Yao and Z. Huang, "Investigation on coaxial stability of nano-bearing under two axis-deviation perturbations," *Sci. China Physics, Mech. Astron.*, vol. 53, no. 12, pp. 2274–2283, 2010, doi: 10.1007/s11433-010-4175-y.

[60] E. H. Cook, M. J. Buehler, and Z. S. Spakovszky, "Mechanism of friction in rotating carbon nanotube bearings," *J. Mech. Phys. Solids*, vol. 61, no. 2, pp. 652–673, 2013, doi: https://doi.org/10.1016/j.jmps.2012.08.004.

[61] Jie Han, Al Globus, Richard Jaffe, and Glenn Deardorff, "Molecular dynamics simulations of carbon nanotube-based gears," *Nanotechnology*, vol. 8, no. 3, p. 95, 1997, doi: 10.1088/0957-4484/8/3/001.

[62] Z. Fu and Z. Xu, "Molecular Dynamics Simulation of Ultra High Speed Nano Wheel Gears in Aqueous Solutions," pp. 323–326, 2019, DOI: 10.1109/EITCE47263.2019.9095019

[63] J. Shi, Z. Cao, J. Wang, J. Shen, and K. Cai, "Stable rotation transmission of a CNT-based nanogear drive system with intersecting axes at low temperature," *Surf. Sci.*, vol. 693, p. 121548, 2020, doi: https://doi.org/10.1016/j.susc.2019.121548.

[64] I. Santamar, D. Reguera, and J. M. Rubi, "Carbon-Nanotube-Based Motor Driven by a Thermal Gradient," 2013, https://doi.org/10.1021/jp311028e.

[65] K. Cai, J. Yu, J. Shi, and Q. H. Qin, "OPEN A method for measuring rotation of a thermal carbon nanomotor using centrifugal effect," *Nat. Publ. Gr.*, pp. 1–10, 2016, doi: 10.1038/srep27338.

[66] K. Cai, J. Shi, J. Yu, and Q. H. Qin, "Dynamic behavior of a rotary nanomotor in argon environments," *Sci. Rep.*, pp. 1–13, 2018, doi: 10.1038/s41598-018-21694-2.

[67] Z. Fu, D. Liang, S. Jiang, P. Zhao, K. Han, and Z. Xu, "nanomotors with different angles," 2019, doi: 10.1063/1.5121642.

[68] K. Cai, P. Wu, J. Shi, Z. Zhong, and Y. Zhang, "CNT-motor driven by competition between thermal fluctuation and REF," *Int. J. Mech. Sci.*, vol. 225, p. 107372, 2022, doi: https://doi.org/10.1016/j.ijmecsci.2022.107372.

[69] J. Li, X. Wang, L. Zhao, X. Gao, Y. Zhao, and R. Zhou, "Rotation motion of designed nano-turbine," *Sci. Rep.*, vol. 4, pp. 1–8, 2014, doi: 10.1038/srep05846.

[70] H. Niu *et al.*, "The nano-pumping process of C20 molecules from carbon nanotube at the different external electric fields and atomic defects: A molecular dynamics approach," *Diam. Relat. Mater.*, vol. 142, p. 110735, 2024, doi: https://doi.org/10.1016/j.diamond.2023.110735.

[71] A. Lohrasebi and Y. Jamali, "Computational modeling of a rotary nanopump," *J. Mol. Graph. Model.*, vol. 29, no. 8, pp. 1025–1029, 2011, doi: https://doi.org/10.1016/j.jmgm.2011.04.007.

[72] Q. Tu, Q. Yang, H. Wang, and S. Li, "Rotating carbon nanotube membrane filter for water desalination," *Sci. Rep.*, vol. 6, pp. 1–11, 2016, doi: 10.1038/srep26183.

[73] Q. Tu, Q. Yang, H. Wang, and S. Li, "Rotating carbon nanotube membrane filter for water desalination," *Nat. Publ. Gr.*, pp. 1–11, 2016, doi: 10.1038/srep26183.

[74] K. Cai *et al.*, "A stable high-speed rotational transmission system based on nanotubes A

stable high-speed rotational transmission system based on nanotubes," vol. 021909, 2015, doi: 10.1063/1.4905696.

[75] H. Yin, K. Cai, N. Wei, Q. H. Qin, and J. Shi, "Study on the dynamics responses of a transmission system made from carbon nanotubes," *J. Appl. Phys.*, vol. 117, no. 23, 2015, doi: 10.1063/1.4922713.

[76] S. Kong, "A review on the size-dependent models of micro-beam and micro-plate based on the modified couple stress theory," *Arch. Comput. Methods Eng.*, vol. 29, no. 1, pp. 1–31, 2022, https://doi.org/10.1007/s11831-021-09567-w.

[77] C. C. Koutsoumaris, K. G. Eptaimeros, and G. J. Tsamasphyros, "A different approach to Eringen's nonlocal integral stress model with applications for beams," *Int. J. Solids Struct.*, vol. 112, pp. 222–238, 2017, https://doi.org/10.1016/j.ijsolstr.2016.09.007.

[78] O. W. Dillon Jr and J. Kratochvil, "A strain gradient theory of plasticity," *Int. J. Solids Struct.*, vol. 6, no. 12, pp. 1513–1533, 1970, https://doi.org/10.1016/0020-7683(70)90061-2.

[79] M. H. Shojaeefard, H. Saeidi Googarchin, M. Mahinzare, and M. Adibi, "Vibration and buckling analysis of a rotary functionally graded piezomagnetic nanoshell embedded in viscoelastic media," *J. Intell. Mater. Syst. Struct.*, vol. 29, no. 11, pp. 2344–2361, 2018, doi: 10.1177/1045389X18770856.

[80] M. H. Shojaeefard, M. Mahinzare, H. Safarpour, H. Saeidi Googarchin, and M. Ghadiri, "Free vibration of an ultra-fast-rotating-induced cylindrical nano-shell resting on a Winkler foundation under thermo-electro-magneto-elastic condition," *Appl. Math. Model.*, vol. 61, pp. 255–279, 2018, doi: 10.1016/j.apm.2018.04.015.

[81] M. Habibi, D. Hashemabadi, and H. Safarpour, "Vibration analysis of a high-speed rotating GPLRC nanostructure coupled with a piezoelectric actuator," *Eur. Phys. J. Plus*, vol. 134, no. 6, Jun. 2019, doi: 10.1140/epjp/i2019-12742-7.

[82] M. Mahinzare, H. Akhavan, and M. Ghadiri, "A nonlocal strain gradient theory for rotating thermo-mechanical characteristics on magnetically actuated viscoelastic functionally graded nanoshell," *J. Intell. Mater. Syst. Struct.*, vol. 31, no. 12, pp. 1511–1523, 2020, doi: 10.1177/1045389X20924828.

[83] A. I. Journal, S. Sadeghzadeh, and M. Mahinzare, "Nonlocal strain gradient theory for dynamical modeling of a thermo-piezo-magnetically actuated spinning inhomogeneous nanoshell," *Mech. Based Des. Struct. Mach.*, vol. 0, no. 0, pp. 1–22, 2020, doi: 10.1080/15397734.2020.1766495.

[84] S. Sadeghzadeh and M. Mahinzare, "Free Vibration Analysis of a Spinning Smart Piezoelectrically Actuated Heterogeneous Nanoscale Shell with Nonlocal Strain Gradient Theory," *J. Nano Res.*, vol. 64, pp. 1–19, 2020, https://doi.org/10.4028/www.scientific.net/JNanoR.64.1

[85] Y. Zhang, Z. Wang, D. Tazeddinova, F. Ebrahimi, M. Habibi, and H. Safarpour, "Enhancing active vibration control performances in a smart rotary sandwich thick nanostructure conveying viscous fluid flow by a PD controller," *Waves in Random and Complex Media*, 2021, doi: 10.1080/17455030.2021.1948627.

[86] B. Zaarour *et al.*, "A review on piezoelectric fibers and nanowires for energy harvesting," vol. 0, no. 0, pp. 1–44, 2019, doi: 10.1177/1528083719870197.

[87] H. Busignies, W. G. Cady, D. Chambers, and G. Rappaport, "Standards on

PIEZOELECTRIC CRYSTALS , 1949," vol. 37, no. 12, 1972, DOI: 10.1109/JRPROC.1949.229975.

[88] S. V Gopinathan, V. V Varadan, and V. K. Varadan, "A review and critique of theories for piezoelectric laminates," *Smart Mater. Struct.*, vol. 9, no. 1, p. 24, 2000, DOI 10.1088/0964-1726/9/1/304.

[89] Q. Wang, S. T. Quek, C. T. Sun, and X. Liu, "Analysis of piezoelectric coupled circular plate," *Smart Mater. Struct.*, vol. 10, no. 2, p. 229, 2001, DOI 10.1088/0964-1726/10/2/308.

[90] Q. Wang, "On buckling of column structures with a pair of piezoelectric layers," *Eng. Struct.*, vol. 24, no. 2, pp. 199–205, 2002, doi: 10.1016/S0141-0296(01)00088-8.

[91] S. K. Kulkarni and S. K. Kulkarni, "Self Assembly," *Nanotechnol. Princ. Pract.*, pp. 125–133, 2015, https://doi.org/10.1007/978-3-319-09171-6.

[92] S. Mourdikoudis, R. M. Pallares, and N. T. K. Thanh, "Characterization techniques for nanoparticles: comparison and complementarity upon studying nanoparticle properties," *Nanoscale*, vol. 10, no. 27, pp. 12871–12934, 2018, DOI: 10.1039/C8NR02278J.

[93] D. Karlicic, T. Murmu, S. Adhikari, and M. McCarthy, *Non-local structural mechanics*. John Wiley & Sons, 2015, DOI: 10.1002/9781118572030.

[94] D. R. Katti, A. Sharma, and K. S. Katti, "Chapter 10 - Predictive Methodologies for Design of Bone Tissue Engineering Scaffolds," S. Bose and A. B. T.-M. for B. D. Bandyopadhyay, Eds., Academic Press, 2017, pp. 453–492. doi: https://doi.org/10.1016/B978-0-12-802792-9.00010-0.

[95] M. E. Gurtin and A. Ian Murdoch, "A continuum theory of elastic material surfaces," *Arch. Ration. Mech. Anal.*, vol. 57, no. 4, pp. 291–323, 1975, doi: 10.1007/BF00261375.

[96] M. E. Gurtin and A. I. Murdoch, "Addenda to our paper A continuum theory of elastic material surfaces," *Arch. Ration. Mech. Anal.*, vol. 59, pp. 389–390, 1975, https://doi.org/10.1007/BF00261375.

[97] A. C. Eringen and D. Edelen, "On nonlocal elasticity," *Int. J. Eng. Sci.*, vol. 10, no. 3, pp. 233–248, 1972, https://doi.org/10.1016/0020-7225(72)90039-0.

[98] R. D. Mindlin, "Micro-structure in linear elasticity," *Arch. Ration. Mech. Anal.*, vol. 16, pp. 51–78, 1964, https://doi.org/10.1007/BF00248490.

[99] R. D. Mindlin, "Second gradient of strain and surface-tension in linear elasticity," *Int. J. Solids Struct.*, vol. 1, no. 4, pp. 417–438, 1965, https://doi.org/10.1016/0020-7683(65)90006-5.

[100] C. W. Lim, G. Zhang, and J. N. Reddy, "A higher-order nonlocal elasticity and strain gradient theory and its applications in wave propagation," *J. Mech. Phys. Solids*, vol. 78, pp. 298–313, 2015, doi: 10.1016/j.jmps.2015.02.001.

[101] V. M. Harik, "Mechanics of carbon nanotubes: Applicability of the continuum-beam models," *Comput. Mater. Sci.*, vol. 24, no. 3, pp. 328–342, 2002, doi: 10.1016/S0927-0256(01)00255-5.

[102] V. M. Harik, "Ranges of applicability for the continuum beam model in the mechanics of carbon nanotubes and nanorods," *Solid State Commun.*, vol. 120, no. 7–8, pp. 331–335, 2001, doi: 10.1016/S0038-1098(01)00383-0.

[103] B. Merwan, B. Abdelkrim, and A. A. Lamine, "Examining the critical speed and electro-mechanical vibration response of a spinning smart single-walled nanotube via nonlocal strain gradient theory," *Mech. Adv. Mater. Struct.*, vol. 0, no. 0, pp. 1–17, 2024, doi: 10.1080/15376494.2024.2341267.

[104] B. Abdelkrim, "Comportement vibratoire des arbres tournants en matériaux composites Soutenu," 2009.

[105] L. Wang and H. Hu, "Thermal vibration of a simply supported single-walled carbon nanotube with thermal stress," *Acta Mech.*, vol. 227, no. 7, pp. 1957–1967, 2016, doi: 10.1007/s00707-016-1608-3.

[106] M. Behzad and A. R. Bastami, "ARTICLE IN PRESS Effect of centrifugal force on natural frequency of lateral vibration of rotating shafts," vol. 274, pp. 985–995, 2004, doi: 10.1016/S0022-460X(03)00659-X.

[107] B. G. Bazehhour, S. M. Mousavi, and A. Farshidianfar, "Free vibration of high-speed rotating Timoshenko shaft with various boundary conditions: effect of centrifugally induced axial force," *Arch. Appl. Mech.*, vol. 84, no. 12, pp. 1691–1700, Dec. 2014, doi: 10.1007/s00419-013-0762-5.

[108] C. T. Loy and K. Y. Lam, "Vibration of cylindrical shells with ring support," *Int. J. Mech. Sci.*, vol. 39, no. 4, pp. 455–471, 1997, doi: 10.1016/s0020-7403(96)00035-5.

[109] L. L. Ke, Y. S. Wang, and J. N. Reddy, "Thermo-electro-mechanical vibration of size-dependent piezoelectric cylindrical nanoshells under various boundary conditions," *Compos. Struct.*, vol. 116, pp. 626–636, 2014, https://doi.org/10.1016/j.compstruct.2014.05.048.

[110] S. Zeng, K. Wang, B. Wang, and J. Wu, "Vibration analysis of piezoelectric sandwich nanobeam with flexoelectricity based on nonlocal strain gradient theory," *Appl. Math. Mech.*, vol. 41, no. 6, pp. 859–880, 2020, doi: 10.1007/s10483-020-2620-8.

[111] F. Mehralian, Y. Tadi Beni, and M. Karimi Zeverdejani, "Nonlocal strain gradient theory calibration using molecular dynamics simulation based on small scale vibration of nanotubes," *Phys. B Condens. Matter*, vol. 514, pp. 61–69, 2017, doi: 10.1016/j.physb.2017.03.030.

[112] K. Ghorbani, A. Rajabpour, and M. Ghadiri, "Determination of carbon nanotubes size-dependent parameters: molecular dynamics simulation and nonlocal strain gradient continuum shell model," *Mech. Based Des. Struct. Mach.*, vol. 49, no. 1, pp. 103–120, 2021, doi: 10.1080/15397734.2019.1671863.

[113] M. R. Ilkhani, R. Nazemnezhad, and S. Hosseini-Hashemi, "Small scale and spin effects on free transverse vibration of size-dependent nano-scale beams," *J. Brazilian Soc. Mech. Sci. Eng.*, vol. 41, no. 11, 2019, doi: 10.1007/s40430-019-1997-z.

[114] S.-T. Choi, J.-D. Wu, and Y.-T. Chou, "Dynamic analysis of a spinning Timoshenko beam by the differential quadrature method," *AIAA J.*, vol. 38, no. 5, pp. 851–856, 2000, https://doi.org/10.2514/2.1039.

[115] A. L. Aouinat, A. Boukhalfa, and S. A. Belalia, "Analytical Solution Using the State-Space Method for Free Vibration Analysis of Rotating Functionally Graded Nanotubes," *J. Vib. Eng. Technol.*, no. 0123456789, 2022, doi: 10.1007/s42417-022-00747-x.

[116] F. Bernardini, V. Fiorentini, and D. Vanderbilt, "Spontaneous polarization and piezoelectric constants of III-V nitrides," *Phys. Rev. B - Condens. Matter Mater. Phys.*,

vol. 56, no. 16, pp. R10024–R10027, 1997, doi: 10.1103/PhysRevB.56.R10024.

[117] H. M. Sedighi, M. Malikan, A. Valipour, and K. K. Zur, "Nonlocal vibration of carbon/boron-nitride nano-hetero-structure in thermal and magnetic fields by means of nonlinear finite element method," *J. Comput. Des. Eng.*, vol. 7, no. 5, pp. 591–602, 2020, doi: 10.1093/jcde/qwaa041.

[118] A. Laturia, M. L. Van de Put, and W. G. Vandenberghe, "Dielectric properties of hexagonal boron nitride and transition metal dichalcogenides: from monolayer to bulk," *npj 2D Mater. Appl.*, vol. 2, no. 1, 2018, doi: 10.1038/s41699-018-0050-x.

[119] J. W. Yan, J. H. Zhu, C. Li, X. S. Zhao, and C. W. Lim, "Decoupling the effects of material thickness and size scale on the transverse free vibration of BNNTs based on beam models," *Mech. Syst. Signal Process.*, vol. 166, no. August 2021, 2022, doi: 10.1016/j.ymssp.2021.108440.

[120] S. H. Mirtalaie and M. A. Hajabasi, "A New Methodology for Modeling and Free Vibrations Analysis of Rotating Shaft Based on the Timoshenko Beam Theory," *J. Vib. Acoust.*, vol. 138, no. 2, pp. 1–13, 2016, doi: 10.1115/1.4032327.

Appendix: Simplified Flowchart of the Galerkin method